ENRICHING QUANTUM SYSTEMS WITH DYNAMIC MAGNON-MEDIATED INTERACTIONS

by

CODY ALEXANDER TREVILLIAN

A dissertation submitted in partial fulfillment of the
requirements for the degree of

DOCTOR OF PHILOSOPHY IN APPLIED AND COMPUTATIONAL PHYSICS

2025

Oakland University
Rochester, Michigan

Doctoral Advisory Committee:

Vasyl Tyberkevych, Ph.D., Chair
Andrei Slavin, Ph.D.
Ilias Cholis, Ph.D.
Steven Louis, Ph.D.
Yi Li, Ph.D.

To my mother, Susan.

For your immense tolerance, unwavering love, and endless support. You were my foundation throughout this entire venture, and I could not have reached this point without you.

ACKNOWLEDGMENTS

I am profoundly indebted to my advisor, Dr. Vasyl Tyberkevych. His mentorship, deep expertise, and, above all, his insurmountable patience were the bedrock of this research. His own deep curiosity was infectious and fueled my own, and his willingness to engage in our countless, challenging discussions was invaluable in shaping this dissertation. I am truly appreciative of his continued guidance and support.

I am also deeply grateful to Dr. Andrei Slavin for his constant encouragement and profound advice. He encouraged me to think critically about my future and, in doing so, helped set the foundation for this entire endeavor.

I am also very grateful to my dissertation committee members: Dr. Ilias Cholis, Dr. Steven Louis, and Dr. Yi Li. I thank them for their time and for the valuable mentorship they provided throughout this process. Their challenging questions and critical suggestions were essential and significantly strengthened this work.

A special acknowledgment is due to our collaborators at Argonne National Laboratory. I extend my sincere thanks to Dr. Yi Li and Dr. Valentine Novosad for their expertise and foundational experimental work on the candidate platform. I am also grateful to Dr. Moojune Song for his crucial work in continuing this development and bringing the near-term host platform to a level that made the analysis in Chapter 4 possible.

My thanks also go to my fellow graduate students and colleagues. The camaraderie, shared problem-solving, and late-night discussions were essential to navigating the challenges of this degree.

Cody Alexander Trevillian

ABSTRACT

ENRICHING QUANTUM SYSTEMS WITH DYNAMIC MAGNON-MEDIATED INTERACTIONS

by

Cody Alexander Trevillian

Adviser: Vasyl Tyberkevych, Ph.D.

Quantum technology is trending toward larger, increasingly interconnected networks of diverse platforms, where coherent information transfer among disparate hardware is essential yet challenging. Magnons, the quanta of spin waves, couple strongly to both bosonic and fermionic quantum objects, offering a route to bridge platforms. This dissertation develops dynamic magnon-mediated interactions that use short, shaped magnetic-field pulses to tune the magnon resonance on demand, linking modules only when needed. By choosing the temporal profile, these pulses deterministically set when, how strongly, and for how long hybrid systems interact, enabling unitary operations such as coherent state transfer, interference, and entanglement not accessible with static or quasi-static control.

We first establish a geometry-agnostic modeling and simulation framework for closed- and open-system dynamics, combining Hamiltonian formulations with a Lindblad master-equation treatment and time-dependent solvers in Liouville space. A modular superconducting-circuit platform provides an architectural basis for strong, designable coupling and near-term programmability while keeping the theory platform agnostic. On this foundation, we design and analyze pulsed magnetic field protocols that implement linear-ramp transfer, parabolic sweeps realizing SWAP and SPLIT operations, and a constant-detuning (rectangular) protocol that yields an analytically tractable family of

unitary gates for single excitations. The rectangular protocol reveals distinct unitary branches and shows how off-resonant operation suppresses dissipation-induced error even as interaction times lengthen.

Two temporal-interferometric applications further demonstrate dynamic control as a resource: time-domain two-magnon interference via a tunable temporal beam splitter, and a temporal magnon–qubit Mach–Zehnder interferometer whose qubit readout encodes magnon dynamics and allows separate estimation of single-magnon amplitude and phase decoherence. Finally, we construct a universal set of magnon-mediated quantum gates, consisting of arbitrary single-qubit rotations and a tunable two-qubit controlled-phase operation, implemented as sequences of dynamically-tuned magnon-mediated interactions. Collectively, these results outline a reconfigurable, near-term pathway for turning strong, tunable magnon coupling into programmable functionality across heterogeneous quantum systems and demonstrate that dynamic magnon-mediated interactions can enrich quantum systems.

TABLE OF CONTENTS

TABLE OF CONTENTS—Continued

LIST OF TABLES

LIST OF FIGURES

LIST OF ABBREVIATIONS

CNOT	controlled-NOT
CPhase	controlled-phase
CPTP	completely positive trace-preserving
CPW	coplanar waveguide
cQED	circuit quantum electrodynamics
FM	ferromagnetic
FMR	ferromagnetic resonance
fSim	fermionic simulation
GKSL	Gorini–Kosakowski–Sudarshan–Lindblad
H	Hadamard
HOM	Hong–Ou–Mandel
HP	Holstein–Primakoff
iSWAP	imaginary swap
LL	Landau–Lifshitz
LLG	Landau–Lifshitz–Gilbert
MS	Mølmer–Sørensen
MZI	Mach–Zehnder interferometer
NM	nonmagnetic
Py	$Ni_{80}Fe_{20}$, permalloy
QSS	quanta subspace

SC	superconducting
Si	Si, silicon
SMD	single magnon decoherence
TBS	temporal beam splitter
TPN	two-port network
YIG	$Y_3Fe_5O_{12}$, yttrium iron garnet

CHAPTER ONE

INTRODUCTION

1.1 Motivation

Quantum systems—whether designed for computing, sensing, or communication—are advancing at a rapid pace, with demonstrations of quantum bits, or qubits, pushing the limits of coherence [1], [2], [3], control [4], [5], and scale [6]. Platforms now operate with tens [7] to hundreds [8] of qubits, proposals target thousands [9], and roadmap toward million-qubit machines have been announced [10], [11]. As these devices scale and interconnect [6], [10], however, decoherence—the irreversible leakage of information to the environment—becomes a more severe constraint [12], [13], and the difficulty of coherently transducing information across different platforms becomes a bottleneck for progress. To address these challenges, research has increasingly turned toward hybrid architectures that can harness the unique advantages of distinct subsystems [14], [15], [16].

Qubits—two-level quantum systems—form the fundamental units of these architectures, encoding quantum information in coherent superpositions of quantum basis states such as, e.g., spin-up and spin-down or $|0\rangle$ and $|1\rangle$ [17], [18]. These coherent states are inherently fragile, however, leading them to be easily disturbed by environmental interactions, and, thus, prone to decoherence during control and communication [12], [13]. Building functional quantum computers and networks therefore requires not only more robust qubits but also architectures that coherently couple disparate subsystems. Because a single technology is unlikely to satisfy all requirements, scalable systems will depend on heterogeneous networks of complementary components coherently linked at the hardware level. Superconducting qubits within circuit quantum electrodynamics (cQED) schemes have emerged as leading platforms due to their scalability and coherence properties [17],

[18], yet they require a means of integration with other elements such as, e.g., optical systems [18], [19], [20] for long-range communication and spin ensembles [18], [21], [22], [23] for enhanced control.

Hybrid quantum systems [14], [15], [16], [24] provide a pathway to address this need by exploiting the natural dynamics of different physical platforms to share and process quantum information coherently and to engineer new functionality from their interplay [14], [16], thereby enabling interactions between otherwise disparate excitations such as, e.g., photons [18], [20], [25], phonons [26], [27], [28], spins [21], [22], [23], [29], and magnons [30], [31], [32], [33], [34], [35]. Primarily, cQED uses superconducting qubits and coplanar superconducting resonators coupled together to bypass the struggles in coherently transducing quantum information and to engineer low-error operations [14], [16]. Within such cQED architectures, superconducting qubits can be seamlessly integrated with microwave resonators, and strong coupling regimes are readily achievable [30], [31], [32], [33], [34], [35], One promising hybrid approach couples cQED—superconducting qubits and coplanar resonators—with magnetic systems to realize unique artificial two-level systems [17], [18], [30], [31], [32], [33], [34], [35]. However, long-lived superconducting modules alone do not solve the broader interconnect problem. Here, ordered magnetic excitations—magnons—become valuable resources.

Magnons—quanta of spin-wave [36], [37], [38] excitations—interact strongly with both bosonic and fermionic quantum objects [30], [31], [32], [33], [34], [35], [39], [40], [41], making them effective mediators for coherent manipulation and transduction between otherwise noninteracting qubits and resonators [39], [40], [41]. As collective excitations of a macroscopically large number of spins, they are versatile, couple efficiently, and are readily controlled via resonant frequency tuning with magnetic fields [19], [21], [22], [30], [31], [32], [33]. Because magnons are composed of spin-density oscillations larger than individual or dilute spin ensembles, they achieve enhanced coupling efficiencies to desired quantum systems in comparison [21], [22]. Experiments show high cooperativity of magnons with microwave photons [30], [31], [32] and superconducting qubits [19], [33]. To prevent decoherence by thermal magnons, the necessary cooling of magnonic systems to the quantum ground state is possible using widely available cryostats [31]. Further prevention of decoherence by higher frequency mode hybridization can be found with ferromagnetic magnons as they exhibit GHz-scale band energy gaps which helps to isolate the quantum state of the system [31]. With sufficiently strong magnon–photon coupling, remote and coherent state transfer—and even gate operations—become feasible, thus enabling key capabilities for controlling networks of quantum information.

Quantum magnonics is a rapidly emerging field that studies these properties of magnons in order to employ them within various quantum technologies [24], [30], [31], [32], [33], [34], [35], [39], [40], [41]. Demonstrations of coherent magnon-photon coupling [31], [32], coherent magnon-qubit interactions [33], and even single-magnon readout [42], [43] have showcased the promise of magnons as central components of hybrid quantum architectures. Contrary to high-quality-factor superconducting qubits and resonators, their comparatively short lifetimes rule out the use of magnons as long-lived quantum memories or qubits, but precisely this property suits them to temporary state transfer. Indeed, magnons are favored for their strong interaction with both bosonic and fermionic quantum objects [30], [31], [32], [33], [34], [35], [39], [40], [41], yet this is directly responsible for their relatively short lifetimes that make them ill-suited as qubits or memories. Instead, by leveraging these strong interactions, they are particularly useful as mediators of quantum interactions and for coherent manipulation and transduction between disparate subsystems [39], [40], [41].

To date, much of the literature on hybrid magnon-photon systems has focused on stationary (static or quasi-static) operation using magnetic bias conditions that are essentially constant during the signal lifetime [30], [31], [32], [33], [34], [35]. In such regimes, the resonant magnon frequency is tuned slowly relative to the signal lifetime, producing hybridized normal modes and the familiar anti-crossing behavior during frequency shifts, but limiting functionality to characterization and steady-state response [30], [31], [32], [33], [34], [35]. These studies have been essential for establishing large coupling rates (often exceeding 100 MHz) in both cavity [31], [32], [33] and planar [30], [34], [35] geometries, yet they do not capitalize on time-dependent control. These quasi-static methods thus restrict functionality and leave open the question of how to harness magnon dynamics for richer, time-programmed, quantum-coherent operations.

This dissertation targets that gap by developing *dynamic magnon-mediated interactions*. The central idea is to use short, shaped magnetic-field pulses to tune the ferromagnetic resonance (FMR) frequency on timescales comparable to the magnon–photon (or magnon–qubit) exchange time, thereby bringing subsystems on- and off-resonance on demand [40], [44], [45], [46], [47], [48], [49], [50], [51], [52], [53], [54], [55], [56], [57], [58], [59], [60], [61], [62], [63], [64], [65], [66], [67], [68], [69]. By selecting the temporal profile, one controls when, how strongly, and for how long the hybrid system interacts, enabling unitary operations such as coherent state transfer, interference, and entanglement generation—capabilities that static tuning cannot realize [40], [44], [45], [46], [47], [48], [49], [50], [51], [52], [53], [54], [55], [56], [57], [58], [59], [60], [61], [62], [63], [64], [65], [66], [67], [68], [69]. Hybrid magnonic systems naturally support such control because the magnon frequency is widely tunable by field across devices spanning 3D cavities [31], [32], [33] to on-chip superconducting resonators [30], [34], [35]. This versatility extends beyond photons—magnons couple to various excitations of both bosonic and fermionic nature and can be tuned by external magnetic fields, suggesting that such time-varying control may unlock additional functionality and allow studies of diverse quantum dynamics at the single-quanta level [30], [31], [32], [33], [34], [35], [39], [40], [41], [70]. For these reasons, dynamically controlled hybrid quantum magnonic systems are of interest for quantum information manipulation and transduction. Exploration of this method for quantum information manipulation and transduction using a dynamically controlled hybrid quantum magnonic system has not been realized previously. Such a technique is also a powerful tool to study fundamental properties of the individual magnon system.

Within this context, this dissertation presents the systematic development of dynamic magnon-mediated interactions from platform to protocol that are designed to enrich quantum systems. First, we establish a modular and scalable superconducting-circuit platform that coherently couples remote magnonic resonators. This provides the architectural basis for programmable interactions between spatially separated magnetic elements as well as the superconducting resonators that couple them. This platform supports strong, designable coupling [71], [72], [73] and establishes a realistic route to integrate hybrid magnonic networks with cQED modules for quantum information tasks.

This dissertation aims to build on that foundation by developing two temporal-interferometric protocols that showcase dynamic control as a resource, advancing time-domain two-magnon interference and a temporal magnon–qubit Mach–Zehnder interferometer. These, together with a gate-level construction, shows how dynamic pulses can enrich quantum functionality. We develop a tunable magnonic "beam splitter" via temporal resonance control to generate and detect entangled magnonic N00N states, and we use pulsed magnon–qubit coupling as temporal "beam splitters" to study single-magnon decoherence channels. Finally, we present the systematic development of a universal set of magnon-mediated quantum gates, showing how sequences of dynamically tuned interactions can implement arbitrary single-qubit rotations and controlled-phase operations on mutually noninteracting qubits—realizing coherent manipulation and transduction using magnons as the active mediator [30], [31], [32], [33], [34], [35], [39],

[40], [41]. We further discuss extensions toward tunable, arbitrary two-qubit operations that go beyond fixed universal sets, addressing an architectural need for scalable quantum-primacy-capable systems [4], [5], [30], [31], [32], [33], [34], [35], [39], [40], [41], [61], [62], [64], [65], [66].

1.2 Organization of this dissertation

Chapter 2 provides a review of the foundational background needed for this dissertation. It begins with an introduction to magnons as collective excitations of spins in magnetic materials, including their dispersion and ferromagnetic resonance. The chapter then presents a primer on qubits and quantum information, emphasizing their coherence and operational principles. Finally, it discusses how magnons and qubits can be combined in hybrid magnonic systems, highlighting why such interactions are attractive for quantum technologies.

Chapter 3 details the methods developed and applied throughout this dissertation. It begins with the construction of hybrid Hilbert spaces and explains how excitation-number truncation allows for efficient modeling of systems with magnons and qubits. Subsequent sections describe Hamiltonian construction, closed-system evolution, and open-system dynamics via the Lindblad master equation. The chapter concludes with a treatment of time-dependent Hamiltonians and the use of the Magnus expansion for simulating dynamically tuned interactions.

Chapter 4 introduces a candidate experimental platform that serves as a foundation for dynamic magnon-mediated protocols. The platform is based on superconducting resonator circuits that integrate chip-mounted magnetic elements. These structures enable strong and tunable coupling between magnons and photons, providing a modular and scalable system on which dynamic protocols may be implemented.

Chapter 5 develops the basic concepts of dynamic magnon tuning protocols. Here the focus is on how pulsed magnetic fields can bring magnon resonances into and out of alignment with other subsystems, thereby enabling coherent energy and information exchange. The chapter demonstrates that shaping the time profile of magnetic field pulses allows different operations to be realized within the same physical system. This establishes the groundwork for the more advanced protocols described later.

Chapter 6 presents the theory and results for time-domain two-magnon interference. By dynamically tuning two magnonic resonators into resonance on demand, the system can realize an effective temporal beam splitter. This mechanism allows for the controlled generation and detection of entangled magnon states, providing a new way to manipulate quantum correlations using magnons.

Chapter 7 introduces the concept of a temporal magnon-qubit Mach–Zehnder interferometer. In this protocol, pulsed magnetic fields are used to couple and decouple a magnon with a qubit, creating an interferometric sequence. The interference patterns that result provide a direct probe of single-magnon decoherence processes. This approach enables new studies of quasi-particle coherence at the single quantum level, with potential applications in quantum information science.

Chapter 8 presents the theoretical framework for a universal set of magnon-mediated quantum gates. By extending the basic dynamic tuning protocols, this work shows that entangling gates between qubits can be mediated by magnons and generalized to arbitrary two-qubit operations. This chapter connects the dissertation results to the broader goal of building magnon-based quantum computing architectures and serves as the landmark achievement of this dissertation.

Chapter 9 concludes the dissertation by summarizing the main findings and discussing future directions. Particular emphasis is placed on the broader impact of dynamic magnon-mediated interactions for quantum technology. The conclusion also highlights open challenges and opportunities for experimental realizations.

CHAPTER TWO

BACKGROUND

This chapter introduces the physical concepts and underlying mathematical models that will be used throughout this dissertation. The work presented in this dissertation lies within the field of quantum magnonics, an intrinsically interdisciplinary area of study that encompasses magnonics and quantum information science. Quantum magnonics is a contemporary field of research, thus it is important to establish a clear technical foundation that supports the findings of this dissertation. In this chapter, we therefore provide the necessary background information to understand how magnons and qubits can be made to interact with one another to form such hybrid quantum magnonic systems.

To this end, the chapter is organized into three major sections: Section 2.1 introduces magnons, starting from the microscopic spin Hamiltonian and proceeding to macroscopic resonance dynamics and quantization, concluding with a review of decoherence phenomena. Section 2.2 presents qubits and a quantum computing primer, beginning from the two-level system model and Bloch sphere, establishing the criteria for valid quantum operations and gates, and outlining the working assumptions of the transmon qubit model. Section 2.3 synthesizes these concepts into the framework of hybrid quantum magnonics, detailing coupling rates, coherent versus dissipative coupling regimes, cooperativity, and the comparative noise analysis that justifies our modeling assumptions. The overall goal is not only to survey prior work but also to establish the common framework, operating regimes, and quantitative benchmarks that anchor the remainder of this dissertation and inform the geometry-agnostic theory of dynamic magnon-mediated interactions we develop.

2.1 Magnons and Ferromagnetic Resonance

Magnons are the quasiparticle quanta of spin waves—the collective excitations of magnetization in ordered ferromagnets. Their utility in quantum systems stems from their bosonic nature and tunable resonant frequencies. This section establishes their fundamental properties. We begin by bridging the microscopic quantum spin-lattice model (the Heisenberg Hamiltonian) to the macroscopic classical description (the Landau–Lifshitz (LL) equation). We then quantize the collective spin excitations (spin waves) to formally derive the bosonic magnon Hamiltonian. This framework is then connected to the experimentally relevant FMR condition in common geometries. Finally, we review the decoherence mechanisms and material properties that define the operational constraints for magnons in hybrid quantum devices.

Spin waves and magnons trace back to Bloch's low-temperature spin-wave theory [74] and the bosonic operator representation of Holstein–Primakoff (HP) for collective spin excitations [75], with interaction effects developed in Dyson's treatments [76] and exchange formalized in Herring's analyses [77]. Uniform-mode FMR in realistic bodies was established by Kittel's formulations for resonance and excitation [78], [79], while geometry- and boundary-sensitive mode structures were clarified for spheres by Walker [80] and for thin films by Damon–Eshbach [81]. Dispersion relations that include both exchange and dipolar contributions were developed in thin films by Kalinikos and Slavin [37]. Experimentally, Brillouin light scattering matured into a precision probe of spin waves [82] and electrical methods enabled on-chip excitation and detection [83], while long-distance magnon transport established magnons as viable carriers [84]. Within materials, $Y_3Fe_5O_{12}$, yttrium iron garnet (YIG) emerged as the benchmark low-damping medium for coherent spin dynamics [85], [86], whereas metallic ferromagnets such as $Ni_{80}Fe_{20}$, permalloy (Py) provide integration advantages at higher loss [34], [35], [87], complementing broader surveys of magnonics and its applications [38], [70], [88]. These ingredients enabled cavity magnonics with strong coherent magnon–photon coupling [30], [31], [32] and direct magnon–qubit interactions in cQED settings [33], and they underpin modern views of magnons as tunable bosonic mediators in hybrid and quantum magnonics [24], [34], [35], [40], [71]. This perspective motivates the developments that follow, in which we adopt a geometry-agnostic but experimentally grounded treatment aimed at hybrid magnonic interfaces and dynamically controlled interactions.

2.1.1 Spin Dynamics and Ferromagnetism

The Heisenberg Hamiltonian for a saturated ferromagnetic (FM) spin-lattice, describing the dominant exchange and Zeeman interactions, is written using spin operators $\hat{\boldsymbol{S}}_i$:

$$\hat{H} = -J \sum_{\langle i,j \rangle} \hat{\boldsymbol{S}}_i \cdot \hat{\boldsymbol{S}}_j - g\mu_B \sum_i \boldsymbol{B} \cdot \hat{\boldsymbol{S}}_i, \tag{2.1}$$

where $J > 0$ is the FM exchange constant, $\langle i, j \rangle$ denotes nearest-neighbor pairs, g is the Landé g-factor, μ_B is the Bohr magneton, and $\boldsymbol{B}$ is the applied magnetic field. The first term favors parallel alignment of neighboring spins, while the second is the Zeeman interaction.

The quantum dynamics of each spin operator are governed by the Heisenberg equation of motion,

$$\frac{d\hat{\boldsymbol{S}}_i}{dt} = \frac{i}{\hbar}[\hat{H}, \hat{\boldsymbol{S}}_i]. \tag{2.2}$$

Evaluating the commutator using the $\mathfrak{su}(2)$ algebra $[\hat{S}_i^\alpha, \hat{S}_j^\beta] = i\hbar\delta_{ij}\epsilon_{\alpha\beta\gamma}\hat{S}_i^\gamma$, we obtain the torque equation for a single spin operator:

$$\frac{d\hat{\boldsymbol{S}}_i}{dt} = -\frac{g\mu_B}{\hbar}\hat{\boldsymbol{S}}_i \times \boldsymbol{B} - \frac{J}{\hbar}\sum_{j\in\mathrm{nn}(i)} \hat{\boldsymbol{S}}_i \times \hat{\boldsymbol{S}}_j. \tag{2.3}$$

The spin operator precesses around the local effective field from the Zeeman and exchange interactions.

To transition to a classical continuum picture, we take the expectation value $\langle \hat{\boldsymbol{S}}(\boldsymbol{r}) \rangle$ and define the coarse-grained magnetization vector $\boldsymbol{M}(\boldsymbol{r})$ as the averaged spin density:

$$\boldsymbol{M}(\boldsymbol{r}) = -\frac{g\mu_B}{a^3} \langle \hat{\boldsymbol{S}}(\boldsymbol{r}) \rangle, \tag{2.4}$$

where a^3 is the unit cell volume. In this continuum model, we replace the discrete exchange sum with its Laplacian form, defining the exchange field $\boldsymbol{H}_{\text{ex}}$:

$$\boldsymbol{H}_{\text{ex}} = \frac{2A}{\mu_0 M_s^2} \nabla^2 \boldsymbol{M}, \tag{2.5}$$

where A is the exchange stiffness. The total effective field, for this simplified model, is the sum of the external field $\boldsymbol{H}_0$ (where $\boldsymbol{B} = \mu_0 \boldsymbol{H}_0$) and this exchange field:

$$\boldsymbol{H}_{\text{eff}} = \boldsymbol{H}_0 + \boldsymbol{H}_{\text{ex}}. \tag{2.6}$$

Inserting this $\boldsymbol{H}_{\text{eff}}$ into the torque equation (2.3) (now using the classical vector $\boldsymbol{M}$) gives the LL equation:

$$\frac{d\boldsymbol{M}}{dt} = -\gamma\, \boldsymbol{M} \times \boldsymbol{H}_{\text{eff}}, \tag{2.7}$$

where $\gamma = g\mu_B/\hbar$ is the gyromagnetic ratio. This derivation connects the microscopic quantum model to the macroscopic continuum equation. Including a phenomenological damping torque $\frac{\alpha_{\text{G}}}{M_s} \boldsymbol{M} \times \frac{d\boldsymbol{M}}{dt}$ yields the Landau–Lifshitz–Gilbert (LLG) equation, which we introduce in Sec. 2.1.5.

2.1.2 Spin Waves and Dispersion

Spin waves are the collective, propagating excitations of the magnetization. They can be understood macroscopically by linearizing the LL equation (2.7) for small transverse fluctuations $\boldsymbol{m}(\boldsymbol{r}, t)$ about the saturated equilibrium magnetization M_s (assumed along $+\hat{z}$):

$$\boldsymbol{M}(\boldsymbol{r}, t) = M_s \hat{z} + \boldsymbol{m}(\boldsymbol{r}, t), \qquad |\boldsymbol{m}| \ll M_s. \tag{2.8}$$

Substituting this into Eq. (2.7) with the effective field from Eq. (2.6) and keeping only terms linear in $\boldsymbol{m}$ yields the linearized dynamical equations.

Taking a plane-wave ansatz for the dynamic components,

$$\boldsymbol{m}(\boldsymbol{r}, t) = \boldsymbol{m}_k e^{i(\boldsymbol{k}\cdot\boldsymbol{r}-\omega t)}, \tag{2.9}$$

we find coupled algebraic equations for m_x and m_y. Solving the determinant condition for nontrivial solutions gives the spin-wave dispersion relation. In the exchange-only case with $\boldsymbol{H}_0 \parallel \hat{z}$, the result is

$$\omega(k) = \gamma\mu_0 \left(H_0 + \frac{2A}{\mu_0 M_s} k^2\right). \tag{2.10}$$

This is a quadratic dispersion relation, where the k^2 term reflects the exchange-induced stiffness of the spin system.

It is important to emphasize that the $k = 0$ limit of this dispersion, $\omega(0) = \gamma\mu_0 H_0$, corresponds to the uniform precession mode, i.e., FMR (in the simple case of an infinite medium, neglecting demagnetization). Thus, the spin-wave framework connects the uniform FMR mode at $k = 0$ to propagating, dispersive spin-wave modes at $k \neq 0$.

2.1.3 Quantization of Spin Waves

To treat spin waves in the quantum limit, we must quantize the underlying spin degrees of freedom. This connects the classical wave picture to the particle picture of magnons. To do this, we return to the microscopic Heisenberg Hamiltonian, Eq. (2.1). Assuming the field is applied along the $\hat{z}$ direction ($\boldsymbol{B} = H_0\hat{z}$), we apply the HP transformation, which maps spin operators to bosonic creation and annihilation operators.

The HP transformation is defined as:

$$\hat{S}_i^+ = \sqrt{2S}\sqrt{1 - \frac{\hat{a}_i^\dagger \hat{a}_i}{2S}}\,\hat{a}_i, \quad \hat{S}_i^- = \sqrt{2S}\,\hat{a}_i^\dagger\sqrt{1 - \frac{\hat{a}_i^\dagger \hat{a}_i}{2S}}, \quad \hat{S}_i^z = S - \hat{a}_i^\dagger \hat{a}_i, \tag{2.11}$$

where $\hat{a}_i$ and $\hat{a}_i^\dagger$ are bosonic operators obeying $[\hat{a}_i, \hat{a}_j^\dagger] = \delta_{ij}$. In the low-excitation (dilute magnon) limit, $\langle \hat{a}_i^\dagger \hat{a}_i \rangle \ll 2S$, we approximate:

$$\hat{S}_i^+ \approx \sqrt{2S}\,\hat{a}_i, \quad \hat{S}_i^- \approx \sqrt{2S}\,\hat{a}_i^\dagger, \quad \hat{S}_i^z \approx S - \hat{a}_i^\dagger \hat{a}_i. \tag{2.12}$$

Substituting this approximation into the Heisenberg Hamiltonian (2.1) (with $\hat{\boldsymbol{S}}_i \cdot \hat{\boldsymbol{S}}_j = \hat{S}_i^z \hat{S}_j^z + \frac{1}{2}(\hat{S}_i^+ \hat{S}_j^- + \hat{S}_i^- \hat{S}_j^+)$), the Hamiltonian becomes:

$$\hat{H} \approx E_0 + g\mu_B H_0 \sum_i \hat{a}_i^\dagger \hat{a}_i + JS \sum_{\langle i,j \rangle} \left(\hat{a}_i^\dagger \hat{a}_i + \hat{a}_j^\dagger \hat{a}_j - \hat{a}_i^\dagger \hat{a}_j - \hat{a}_j^\dagger \hat{a}_i \right), \tag{2.13}$$

where E_0 is the constant ground-state energy. To diagonalize this, we transform to momentum space with the Fourier transform:

$$\hat{a}_i = \frac{1}{\sqrt{N}} \sum_{\boldsymbol{k}} \hat{a}_{\boldsymbol{k}} e^{i\boldsymbol{k}\cdot\boldsymbol{r}_i}, \quad \hat{a}_i^\dagger = \frac{1}{\sqrt{N}} \sum_{\boldsymbol{k}} \hat{a}_{\boldsymbol{k}}^\dagger e^{-i\boldsymbol{k}\cdot\boldsymbol{r}_i}. \tag{2.14}$$

The Hamiltonian becomes a sum of independent harmonic oscillators:

$$\hat{H} = E_0 + \sum_{\boldsymbol{k}} \hbar\omega(\boldsymbol{k})\, \hat{a}_{\boldsymbol{k}}^\dagger \hat{a}_{\boldsymbol{k}}, \tag{2.15}$$

This is the Hamiltonian for a collection of independent harmonic oscillators, where $\hbar\omega(\boldsymbol{k})$ is the magnon dispersion relation. The quantized excitations, $\hat{a}_{\boldsymbol{k}}^\dagger |0\rangle$, are the magnons. These are bosonic quasiparticles carrying spin angular momentum $\hbar$ antiparallel to the magnetization. Note that in later chapters, we will use $\hat{m}$ for magnon operators and $\hat{q}$ for qubit operators to distinguish them.

For a simple cubic lattice with lattice constant a and coordination number z, the dispersion is

$$\hbar\omega(\boldsymbol{k}) = g\mu_B H_0 + 2JSz \left(1 - \frac{1}{z} \sum_{\delta} e^{i\boldsymbol{k}\cdot\delta} \right), \tag{2.16}$$

where δ runs over nearest-neighbor displacements. In the long-wavelength limit ($ka \ll 1$), expanding the exponential gives

$$\hbar\omega(\boldsymbol{k}) \approx g\mu_B H_0 + Dk^2, \tag{2.17}$$

with $D = 2JSa^2$ the spin-wave stiffness. This result, derived from a fully quantum model, is identical to the classical dispersion relation, Eq. (2.10) (since $\gamma\mu_0 H_0 = g\mu_B H_0/\hbar$). This formally establishes the equivalence between the classical spin-wave model and the quantum magnon picture.

2.1.4 Resonance in Selected Geometries

The simple $k = 0$ FMR frequency, $\omega(0) = \gamma\mu_0 H_0$, is only valid for an infinite medium. In any real sample, the dipolar interactions (which we ignored for simplicity) create a **demagnetization field**, $\boldsymbol{H}_{\text{demag}}$, which shifts the resonance. This effect is shape-dependent and is critical for device engineering.

We account for this by modifying the effective field in the LL equation (2.7) to $\boldsymbol{H}_{\text{eff}} = \boldsymbol{H}_0 + \boldsymbol{H}_{\text{demag}}$. For a general ellipsoid, this demagnetization field is uniform and can be written $\boldsymbol{H}_{\text{demag},i} = -N_i M_i$, where N_i (for $i = x, y, z$) are the demagnetization factors. Linearizing the LL equation with this new $\boldsymbol{H}_{\text{eff}}$ (and assuming $\boldsymbol{H}_0$ is along $\hat{z}$) yields the Kittel formula:

$$\omega_{\text{FMR}} = \gamma\sqrt{\mu_0(H_0 + (N_y - N_z)M_s)\mu_0(H_0 + (N_x - N_z)M_s)}. \tag{2.18}$$

This expression shows that the resonance frequency depends on the sample geometry through $N_{x,y,z}$.

For a **thin film** magnetized in-plane (e.g., the xy-plane), the demagnetization factors are approximately $N_x \approx 0$, $N_y \approx 0$, and $N_z \approx 1$. The FMR condition becomes:

$$\omega_{\text{film}} = \gamma\sqrt{\mu_0 H_0 \mu_0(H_0 + M_s)}. \tag{2.19}$$

(Note: M_s is often given in different units, leading to the common form $\sqrt{H_0(H_0 + 4\pi M_s)}$). This geometry is relevant for on-chip planar resonators.

For a uniformly magnetized **sphere**, the demagnetization factors are identical, $N_x = N_y = N_z = 1/3$. The Kittel formula simplifies significantly:

$$\omega_{\text{sphere}} = \gamma \mu_0 H_0. \tag{2.20}$$

This simple, isotropic resonance condition, combined with their extremely low damping, makes YIG spheres ideal systems for studying fundamental magnon physics and for hybrid quantum applications.

This macroscopic, geometry-dependent framework is consistent with the microscopic model. The simple dispersion in Eq. (2.17) gives $\omega(0) = \gamma\mu_0 H_0$, which exactly matches the Kittel formula for a sphere (which has no shape anisotropy). The more complex geometries (like the film) simply add the (anisotropic) demagnetization field to H_0.

2.1.5 Decoherence and Materials Considerations

For magnons to be useful in quantum protocols, their coherence lifetime must be sufficiently long. This subsection analyzes the damping mechanisms that limit magnon coherence and introduces the key material parameters.

Decoherence is commonly described by the phenomenological Gilbert damping parameter α_{G}, which adds a damping torque to the LL equation (2.7):

$$\frac{d\boldsymbol{M}}{dt} = -\gamma\, \boldsymbol{M} \times \boldsymbol{H}_{\text{eff}} + \frac{\alpha_{\mathrm{G}}}{M_s}\, \boldsymbol{M} \times \frac{d\boldsymbol{M}}{dt}. \tag{2.21}$$

This term describes energy dissipation into the lattice, leading to a broadening of the FMR linewidth $\Delta\omega$. The effective magnon lifetime τ_m is related to this linewidth by

$$\tau_m = \frac{1}{\Delta\omega}, \qquad \Delta\omega \approx \alpha_{\mathrm{G}}\, \omega_m, \tag{2.22}$$

so lower damping α_G directly translates to longer coherence times. Microscopically, this damping arises from channels like magnon-phonon and impurity scattering.

For quantum applications, we define the magnon relaxation rate Γ_m and the quality factor Q_m:

$$\Gamma_m = \frac{\Delta\omega}{2}, \qquad Q_m = \frac{\omega_m}{\Delta\omega}. \tag{2.23}$$

Hybrid quantum systems require Q_m to be high enough to enter the strong-coupling regime, $g > \Gamma_m$ (where g is the coherent coupling rate).

From a materials perspective, YIG is the benchmark low-damping material. Bulk YIG spheres exhibit $\alpha_G \sim 10^{-5}$, leading to microsecond coherence times. Epitaxial YIG films show higher damping (e.g., $\alpha_G \sim 10^{-4}$) but are superior to metallic ferromagnets. Sputtered YIG films allow for nanometer-scale thicknesses compatible with on-chip fabrication, though with higher damping. Py, while common in spintronics, has a very high damping $\alpha_G \sim 10^{-2}$, which severely limits its coherence time.

Table 2.1: Representative parameters for magnons in selected materials and geometries at **cryogenic temperatures**. $\omega_m/2\pi$ is the FMR frequency, α_G is the Gilbert damping parameter, $\Gamma_m/2\pi$ is the relaxation rate, and τ_m is the corresponding lifetime. Values are approximate and representative.

Material / Geometry	$\omega_m/2\pi$ (GHz)	α_G	$\Gamma_m/2\pi$ (MHz)	τ_m (ns)
YIG Sphere	5–10	10^{-5}	0.05–0.1	1000–2000
Epitaxial YIG Film	5–10	10^{-4}	0.5–1	200–400
Py Film	8–30	10^{-2}	50–100	2–4

The table highlights the dramatic differences between materials. YIG spheres provide coherence times orders of magnitude longer than Py films, explaining their dominance in quantum magnonics. This analysis of decoherence sets the fundamental timescales for magnon-based operations and leads directly into Section 2.2, where we will introduce the qubit parameters for a direct comparison.

2.2 Qubits and Quantum Computing

In classical computing, the fundamental unit of information is the **bit**, which exists in one of two definite states: 0 or 1. Quantum computing is built upon a more general concept: the **qubit** (or quantum bit) [89]. A qubit is a two-level quantum system that can exist in the state $|0\rangle$, the state $|1\rangle$, or—critically—in a **coherent superposition** of both states simultaneously. This property allows quantum computers to perform calculations in a way that is fundamentally different from their classical counterparts [90], [91].

This section details the physics of these qubits, describing their geometric representation, the rules for their manipulation and noise, the quantum gates that form a universal set for computation [92], and the specific transmon model that justifies the Hamiltonians used in this dissertation.

The conceptual foundations of quantum computation—viewing computation as controlled evolution of two-level systems—grew from the simulation and algorithmic arguments of Feynman and Deutsch and the formalization of quantum information by Schumacher [89], [90], [91], [93], and the experimental era accelerated with cQED, where superconducting (SC) qubits couple coherently to microwave resonators and admit precise control [17], [18], leading to platforms that now field tens to hundreds of qubits and high-fidelity gates across industrial and academic efforts [4], [7], [94], [95]. In parallel, trapped ions [96], [97], semiconductor spin qubits [98], [99], neutral atoms [100], [101], and photonic qubits [102], [103] diversified the hardware landscape while retaining the same universal description of qubits as controllable, entangleable two-level systems subject to noise. Coherence metrics and noise models matured alongside these platforms, with relaxation and dephasing motivating error-mitigation and error-correction strategies

[104], [105], [106], [107] and with state-of-the-art SC qubit coherence and control figures summarized in recent surveys and demonstrations [1], [2], [4], [5], [7]. Dominant decoherence mechanisms in SC devices—dielectric loss, flux noise, and quasiparticles—remain central design targets [7], [108], even as the community continues to improve materials, layouts, and control. The broader theory and visualization toolbox spans early two-level-system and Bloch-sphere treatments from NMR and quantum mechanics [109], [110], through first coherent control of charge/flux devices and the advent of the transmon that suppresses charge noise while preserving anharmonicity [111], [112], and across mature modalities including ions [96], [113], [114], semiconductors [98], [115], and optics [102], [116], all framed consistently by completely positive trace-preserving (CPTP) maps for open-system dynamics [92]. Industrial ecosystems now expose cloud-accessible devices with universal gate sets—IBM's transmon systems [9], Google's Sycamore using fermionic simulation (fSim)/controlled-phase (CPhase) gates [4], [5], Amazon Braket's multi-technology offerings [117], and photonic efforts from Xanadu and PsiQuantum [118], [119]—which together underscore both the promise and the limits of current approaches. Against this backdrop, our viewpoint for the remainder of the chapter is pragmatic and platform-agnostic: we treat qubits in a working model as truncated bosonic modes with sufficient anharmonicity to support coherent control, a stance that aligns naturally with the magnonic mediators developed later and clarifies how these qubits interface within hybrid magnon–qubit architectures.

2.2.1 Two-Level Systems and the Bloch Sphere

A qubit is a quantum two-level system whose state $|\psi\rangle$ can be described as a vector in a two-dimensional Hilbert space spanned by the computational basis states, $|0\rangle$ and $|1\rangle$. Unlike a classical bit, a qubit can exist in a **coherent superposition** of these two states. An arbitrary pure qubit state is written as

$$|\psi\rangle = \alpha\,|0\rangle + \beta\,|1\rangle\,, \qquad \alpha, \beta \in \mathbb{C}, \qquad |\alpha|^2 + |\beta|^2 = 1. \tag{2.24}$$

The complex coefficients α and β are the probability amplitudes, where $|\alpha|^2$ is the probability of measuring the qubit in state $|0\rangle$ and $|\beta|^2$ is the probability of measuring $|1\rangle$.

A powerful geometric representation for a single qubit state is the **Bloch sphere** [109], [110]. This visualization, depicted in Fig. 2.1, maps the abstract state vector onto a tangible, three-dimensional unit sphere, providing a clear intuition for qubit states and operations. The state of any pure qubit can be mapped to a point on the surface of a unit sphere. The "north pole" ($\theta = 0$) of the sphere corresponds to the state $|0\rangle$, and the "south pole" ($\theta = \pi$) corresponds to $|1\rangle$. Points on the equator ($\theta = \pi/2$) represent equal superpositions of $|0\rangle$ and $|1\rangle$. This visualization allows us to parameterize the qubit state from Eq. (2.24) using two real angles, the polar angle $\theta \in [0, \pi]$ and the azimuthal angle $\phi \in [0, 2\pi)$:

$$|\psi\rangle = \cos\!\left(\tfrac{\theta}{2}\right)|0\rangle + e^{i\phi}\sin\!\left(\tfrac{\theta}{2}\right)|1\rangle = \begin{pmatrix} \cos\!\left(\frac{\theta}{2}\right) \\ e^{i\phi}\sin\!\left(\frac{\theta}{2}\right) \end{pmatrix}, \tag{2.25}$$

where an unobservable global phase $e^{i\gamma}$ has been omitted. This two-component complex vector is known as a **spinor**.

This geometric picture is further formalized using the density matrix $\rho = |\psi\rangle\langle\psi|$. For any single-qubit state (pure or mixed), the density matrix can be written as

$$\rho = \frac{1}{2}\left(I + \vec{r}\cdot\vec{\sigma}\right), \tag{2.26}$$

where $\vec{\sigma} = (\sigma_x, \sigma_y, \sigma_z)$ are the Pauli matrices and $\vec{r}$ is the **Bloch vector**. For a pure state, $\vec{r}$ is a unit vector given by $\vec{r} = (\sin\theta\cos\phi, \sin\theta\sin\phi, \cos\theta)$. For mixed states (resulting from noise or decoherence), the vector's length is less than one ($|\vec{r}| < 1$), and the state is represented by a point *inside* the sphere.

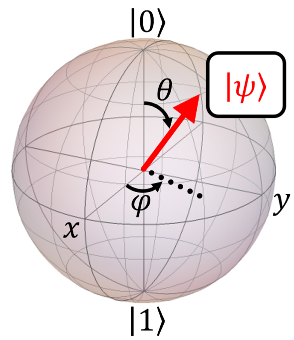

Figure 2.1: A visualization of the Bloch sphere. The state of a qubit $|\psi\rangle$ is mapped to a vector $\vec{r}$ (red) on the surface of a unit sphere. The north pole ($\theta = 0$) represents the $|0\rangle$ state (e.g., spin-up), and the south pole ($\theta = \pi$) represents the $|1\rangle$ state (e.g., spin-down). Points on the equator represent equal superpositions of $|0\rangle$ and $|1\rangle$.

The qubit formalism is mathematically equivalent to the spin-$\frac{1}{2}$ representation of angular momentum. In this framework, $|0\rangle$ and $|1\rangle$ are the eigenstates of the spin-z operator, $\hat{S}_z = \frac{\hbar}{2}\sigma_z$. This equivalence is especially important for this dissertation, as magnons are collective excitations of many spins. The qubit-magnon interactions we will develop thus naturally inherit the mathematical structures of spin dynamics.

2.2.2 Valid Quantum Operations and Noise Channels

Any physical transformation of a qubit state, whether an ideal computation or a noisy interaction with the environment, must be a **CPTP** map. In the density-matrix formalism, a quantum operation is a linear superoperator $\mathcal{E}$ that maps an initial state ρ to a final state $\rho' = \mathcal{E}(\rho)$. For this map to be physically valid, it must be trace-preserving ($\mathrm{Tr}(\rho') = \mathrm{Tr}(\rho) = 1$) and completely positive (ensuring that even when applied to part of an entangled system, the resulting density matrix remains valid). The most general form of such a CPTP map is the **Kraus representation** [92]:

$$\mathcal{E}(\rho) = \sum_{\mu} K_\mu \rho K_\mu^\dagger, \qquad \sum_{\mu} K_\mu^\dagger K_\mu = I, \tag{2.27}$$

where the $\{K_\mu\}$ are the Kraus operators that define the operation, or "channel."

Purely coherent qubit evolutions, such as ideal quantum gates, are a special case where there is only one Kraus operator, $K_0 = U$. The trace-preserving condition $\sum K_\mu^\dagger K_\mu = I$ simplifies to $U^\dagger U = I$, which is the definition of a **unitary matrix**. The evolution is thus $\rho' = U\rho U^\dagger$. On the Bloch sphere, a unitary operation corresponds to a rigid rotation of the state vector.

Realistic qubit dynamics, however, inevitably involve noise and decoherence. These are non-unitary processes described by channels with more than one Kraus operator. Two canonical examples are amplitude damping and dephasing. **Amplitude Damping** models energy relaxation from $|1\rangle$ to $|0\rangle$ with probability λ, corresponding to the T_1 time. The Kraus operators are

$$K_0 = \begin{pmatrix} 1 & 0 \\ 0 & \sqrt{1-\lambda} \end{pmatrix}, \qquad K_1 = \begin{pmatrix} 0 & \sqrt{\lambda} \\ 0 & 0 \end{pmatrix}. \tag{2.28}$$

This operation shrinks the Bloch vector toward the $|0\rangle$ state. **Dephasing** models the loss of phase coherence between $|0\rangle$ and $|1\rangle$ with probability p, corresponding to the T_2 time. The Kraus operators are

$$K_0 = \sqrt{1-p}\, I, \qquad K_1 = \sqrt{p}\, |0\rangle \langle 0|, \qquad K_2 = \sqrt{p}\, |1\rangle \langle 1|. \tag{2.29}$$

This operation damps the x and y components of the Bloch vector, causing it to shrink onto the z-axis.

While the Kraus representation is general, continuous-time dynamics are often described by the Gorini–Kosakowski–Sudarshan–Lindblad (GKSL) master equation. This formalism, which we will define in detail in Chapter 3, describes the evolution via a coherent part ($[H, \rho]$) and a "dissipator" term that describes noise processes using collapse operators.

2.2.3 Quantum Gates and Universal Sets

Unlike a classical computer gate (e.g., AND, NOT), which is a physical circuit of transistors, a **quantum gate** is a physical *operation* that implements a specific unitary evolution on one or more qubits. This operation is typically realized by applying a precisely shaped sequence of control pulses (e.g., microwave or magnetic-field pulses) to the qubit system for a fixed duration.

Any single-qubit operation corresponds to a rotation of the Bloch vector. The most general single-qubit unitary gate U can be parameterized by three angles:

$$U(\theta, \phi, \lambda) = \begin{pmatrix} \cos\left(\frac{\theta}{2}\right) & -e^{i\lambda}\sin\left(\frac{\theta}{2}\right) \\ e^{i\phi}\sin\left(\frac{\theta}{2}\right) & e^{i(\phi+\lambda)}\cos\left(\frac{\theta}{2}\right) \end{pmatrix}. \tag{2.30}$$

This includes common gates like the Pauli gates X, Y, Z (which perform π-rotations around their respective axes) and continuous-parameter rotations $R_x(\theta)$ and $R_z(\phi)$:

$$\begin{aligned} R_x(\theta) &= \exp\Big(-i\frac{\theta}{2}X\Big) = \begin{pmatrix} \cos\frac{\theta}{2} & -i\sin\frac{\theta}{2} \\ -i\sin\frac{\theta}{2} & \cos\frac{\theta}{2} \end{pmatrix}, \\ R_z(\phi) &= \exp\Big(-i\frac{\phi}{2}Z\Big) = \begin{pmatrix} e^{-i\phi/2} & 0 \\ 0 & e^{+i\phi/2} \end{pmatrix}. \end{aligned} \tag{2.31}$$

The **Hadamard (H) gate (*H*)** is particularly important, as it is the operation that creates an equal superposition $|+\rangle$ from the ground state $|0\rangle$:

$$H = \frac{1}{\sqrt{2}}\begin{pmatrix} 1 & 1 \\ 1 & -1 \end{pmatrix}, \qquad H|0\rangle = |+\rangle = \frac{|0\rangle + |1\rangle}{\sqrt{2}}. \tag{2.32}$$

Single-qubit gates are not sufficient for universal quantum computation; they cannot create the crucial resource of **entanglement**. This requires two-qubit gates. The most familiar is the **controlled-NOT (CNOT)** gate, which flips the second (target) qubit if and only if the first (control) qubit is $|1\rangle$:

$$\text{CNOT} = \begin{pmatrix} 1 & 0 & 0 & 0 \\ 0 & 1 & 0 & 0 \\ 0 & 0 & 0 & 1 \\ 0 & 0 & 1 & 0 \end{pmatrix}. \tag{2.33}$$

A closely related gate is the **CPhase** gate, which applies a phase $e^{i\phi}$ if and only if both qubits are in the $|11\rangle$ state:

$$\mathrm{CPhase}(\phi) = \begin{pmatrix} 1 & 0 & 0 & 0 \\ 0 & 1 & 0 & 0 \\ 0 & 0 & 1 & 0 \\ 0 & 0 & 0 & e^{i\phi} \end{pmatrix}. \tag{2.34}$$

These two gates are inter-convertible with the help of single-qubit H gates. For example, a CNOT is a CPhase(π) gate conjugated by H gates on the target qubit:

$$\mathrm{CNOT} = (I \otimes H)\,\mathrm{CPhase}(\pi)\,(I \otimes H). \tag{2.35}$$

A set of quantum gates is **universal** if any possible quantum algorithm (i.e., any n-qubit unitary operation) can be approximated to arbitrary precision by a sequence of gates from that set [92]. A common universal set is any arbitrary single-qubit rotation combined with a single two-qubit entangling gate, such as CNOT or CPhase.

Different hardware platforms have different ”native” gate sets. SC qubits (IBM, Google) often use continuous R_x, R_z rotations and CNOT or ’fSim’ gates. Trapped-ion systems (IonQ) often use collective rotations and the Mølmer–Sørensen (MS) gate. Photonic systems often use phase shifters and CPhase gates. A common two-qubit gate is the **imaginary swap (iSWAP)** gate, which swaps the states $|01\rangle \leftrightarrow |10\rangle$ with an acquired phase:

$$\mathrm{iSWAP} = \begin{pmatrix} 1 & 0 & 0 & 0 \\ 0 & 0 & i & 0 \\ 0 & i & 0 & 0 \\ 0 & 0 & 0 & 1 \end{pmatrix}. \tag{2.36}$$

The **MS** gate is also widely used, particularly in ion traps:

$$\mathrm{MS}(\theta) = \begin{pmatrix} \cos\theta & 0 & 0 & -i\sin\theta \\ 0 & \cos\theta & -i\sin\theta & 0 \\ 0 & -i\sin\theta & \cos\theta & 0 \\ -i\sin\theta & 0 & 0 & \cos\theta \end{pmatrix}. \tag{2.37}$$

Google's 'fSim gate, used in their supremacy experiments [4], generalizes the iSWAP gate:

$$\mathrm{fSim}(\theta, \phi) = \begin{pmatrix} 1 & 0 & 0 & 0 \\ 0 & \cos\theta & -i\sin\theta & 0 \\ 0 & -i\sin\theta & \cos\theta & 0 \\ 0 & 0 & 0 & e^{-i\phi} \end{pmatrix}. \tag{2.38}$$

As we will show in Chapter 8, our magnon-mediated platform naturally realizes tunable CPhase gates, positioning it to form a universal gate set.

Table 2.2: Representative universal gate sets across quantum computing platforms.

Platform	**Single-qubit gates**	**Two-qubit gate**
SC (IBM)	$R_x(\theta), R_y(\theta), R_z(\theta)$	CNOT
SC (Google)	$R_x(\theta), R_z(\theta)$	$\mathrm{fSim}(\theta, \phi)$
Trapped ions	Collective rotations	MS
Photonic systems	Phase shifters, beamsplitters	CPhase
Magnon-mediated (this work)	R_x, R_z-like	CPhase analog

2.2.4 Transmon Qubit Model

A leading physical implementation of a SC qubit is the **transmon** [112]. While its full circuit dynamics are complex, for our purposes it is modeled as a **weakly anharmonic oscillator**. The key feature of the transmon is that its energy levels are not evenly spaced, unlike a simple harmonic oscillator.

The Hamiltonian for this system, also known as the Duffing oscillator, can be written as

$$\frac{H_q}{\hbar} = \left(\omega_q - \frac{\alpha_\mathrm{q}}{2}\right) \hat{q}^\dagger \hat{q} + \frac{\alpha_\mathrm{q}}{2} (\hat{q}^\dagger \hat{q})^2, \tag{2.39}$$

where $\hat{n} = \hat{q}^\dagger \hat{q}$ is the number operator. Here, $\alpha_\mathrm{q} < 0$ is the **anharmonicity**, which is the crucial parameter. This Hamiltonian gives non-equidistant energy levels

$E_n \approx (\omega_q - \frac{\alpha_q}{2})n + \frac{\alpha_q}{2}n^2$. The $|0\rangle \leftrightarrow |1\rangle$ transition frequency is $\omega_{01} = (E_1 - E_0)/\hbar = \omega_q$, but the next transition, $|1\rangle \leftrightarrow |2\rangle$, has a different frequency: $\omega_{12} = (E_2 - E_1)/\hbar = \omega_q + \alpha_q$.

Because α_q is large and negative (typically $\alpha_q/2\pi \sim -100$ to -500 MHz), the ω_{12} transition is hundreds of MHz away from the ω_{01} ”qubit” transition. As long as our control pulses are tuned to ω_q and are weak compared to $|\alpha_q|$, we will never accidentally drive the $|1\rangle \leftrightarrow |2\rangle$ transition. This allows us to **truncate** the model and treat the transmon as a perfect two-level system, ignoring all states $|2\rangle$ and higher.

For our dissertation, we therefore adopt a simplified working model. We treat the qubit as a truncated two-level system but use the bosonic language to maintain an algebraic parallel with the magnon model. Our working Hamiltonian after truncation is the simple harmonic form

$$\frac{H_q}{\hbar} \simeq \omega_q \, \hat{q}^\dagger \hat{q}, \tag{2.40}$$

where $\hat{q}^\dagger$ ($\hat{q}$) creates (annihilates) a qubit excitation only within the truncated $\{|0\rangle, |1\rangle\}$ subspace. This notation effectively sets the ground state energy E_0 to zero, and the first excited state $|1\rangle$ has energy $\hbar\omega_q$.

For simulating hybrid dynamics, we make two further modeling choices. First, we adopt a **rotating frame** at the qubit frequency ω_q, so that the qubit's own Hamiltonian becomes $\tilde{H}_q = H_q - \hbar\omega_q \hat{q}^\dagger \hat{q} = 0$. In this frame, the $|1\rangle$ state is now also at zero energy, and the only relevant frequencies are the detunings of other modes relative to the qubit, i.e., $\Delta_m(t) \equiv \omega_m(t) - \omega_q$. Second, the interactions we consider are number-conserving, so we restrict the evolution to a specific excitation manifold. For example, in a single-excitation-swap protocol, the relevant subspace is

$$\mathcal{H}_1 = \mathrm{span}\left\{ |1;0\rangle, \; |0;1\rangle \right\}. \tag{2.41}$$

The vacuum state $|0;0\rangle$ does not participate in the coherent dynamics.

The coupling terms are also written in this bosonic language. The qubit–magnon exchange interaction used throughout is

$$\frac{H_{\text{int}}}{\hbar} = g\big(\hat{m}\,\hat{q}^{\dagger} + \hat{m}^{\dagger}\hat{q}\big), \tag{2.42}$$

which preserves the total excitation number (e.g., $N = 1$ in $\mathcal{H}_1$). This simplified model enables a clean comparison of energy scales and noise with the magnon parameters when we assemble the full hybrid Hamiltonian in Section 2.3.

2.2.5 Qubit Decoherence and Lifetimes

Like any quantum system, qubits suffer from decoherence, which limits the time available to perform computations. The two primary decoherence mechanisms are **Energy Relaxation (T_1)**, the spontaneous decay from $|1\rangle \to |0\rangle$, and **Dephasing (T_2)**, the loss of phase coherence between $|0\rangle$ and $|1\rangle$.

For modeling purposes, we express these characteristic times as rates. The relaxation rate is simply

$$\Gamma_1^{(q)} = \frac{1}{T_1}. \tag{2.43}$$

The total dephasing rate $1/T_2$ is the sum of relaxation and ”pure dephasing” ($\Gamma_\phi^{(q)} = 1/T_\phi$) contributions:

$$\frac{1}{T_2} = \frac{1}{2T_1} + \frac{1}{T_\phi}. \tag{2.44}$$

The rates we use in the Lindblad formalism (Chapter 3) are thus defined as $\Gamma_1^{(q)}$ and $\Gamma_\phi^{(q)}$.

The anharmonicity α_{q} must also be large enough to prevent leakage to higher states, with typical transmon values [7] being $\alpha_{\text{q}}/2\pi \sim -100$ to -500 MHz. Table 2.3 lists representative coherence times for state-of-the-art SC qubits at dilution refrigerator temperatures.

Table 2.3: Representative SC-qubit coherence figures at cryogenic temperatures. Ranges are indicative of recent reports and roadmap targets [4], [5], [7], [9].

Quantity	Symbol	Typical range
Qubit frequency	$\omega_q/2\pi$	4–8 GHz
Energy relaxation time	T_1	50–300 μs
Dephasing time	T_2	30–200 μs
Pure dephasing time	T_ϕ	50–500 μs
Anharmonicity	$\alpha_\mathrm{q}/2\pi$	-100 to -500 MHz
Single-qubit gate time	t_{1q}	5–40 ns
Two-qubit gate time	t_{2q}	20–300 ns

These values show a crucial hierarchy: coherent gate operations (t_{1q}, t_{2q}) are performed on nanosecond timescales, while decoherence (T_1, T_2) occurs over tens to hundreds of microseconds. This wide separation leaves an ample window for computation.

2.3 Hybrid Magnonic Systems and Quantum Magnonics

The development of **hybrid quantum magnonics** [39], [40] is motivated by the goal of combining the best qualities of magnonic and SC quantum systems. On their own, magnons offer tunability and strong, fast interactions, but suffer from relatively short lifetimes. SC qubits, conversely, have long coherence times and are highly controllable, but are less versatile in their interactions. This section demonstrates how integrating them—using the magnon as a fast, tunable mediator for the long-lived qubit—provides a new pathway for dynamic, high-performance quantum information processing.

Hybrid quantum systems emerged as a design strategy to combine complementary subsystems [14], [15], [16], with cQED setting the chip-scale template by coherently integrating Josephson qubits and microwave resonators [17], [18]. Cavity magnonics then established strong coupling between magnons and microwave photons and later direct magnon–qubit interactions, positioning magnons as tunable mediators [30], [31], [32], [33], [39], [40]. Three platforms now anchor the field: 3D microwave cavities with YIG spheres [31], [32], planar coplanar waveguide (CPW) resonators with YIG films or FM stripes [30], [34], [35], [120], [121], and integrated qubit-on-chip devices with nearby magnetic elements [24], [71]. Compact reductions developed in parallel: dispersive Schrieffer–Wolff treatments for coherent exchange and dressed shifts [71], [122], [123], [124], [125], and Heisenberg–Langevin input–output models that separate coherent exchange from environment-induced couplings and predict level attraction under specific phasing and loading [126], [127], [128], [129], [130], [131], [132]. Remote and multiport layouts add propagation phase control that governs bright/dark superpositions and the crossover between resolvable mode splitting and attraction, with microscopic analyses and experiments linking phase and external coupling to the coherent–dissipative balance [34], [71], [133], [134], [135], [136], [137]. The literature has largely focused on static or quasi-static biasing, while recent proposals and demonstrations highlight dynamic magnon-frequency tuning as a route to programmable state transfer, gates, and entanglement [41], [44], [45], [72], [73], [138]. Framed against SC-qubit coherence and noise scales that set practical timing windows [4], [7], [139], this section adopts a geometry-agnostic yet experimentally grounded view that distills coherent and dissipative magnon-mediated couplings, benchmarks operating regimes, and motivates dynamic control as a means to enrich hybrid quantum systems.

2.3.1 Hybrid vs Quantum Magnonics

The distinction between ”hybrid magnonics” and ”quantum magnonics” is determined by the thermal occupation of the magnon mode [40]. The crossover from the classical (hybrid) to the quantum regime occurs when the mean thermal Bose occupancy, $\bar{n}_{\mathrm{th}}$, is much less than one. The thermal occupancy at angular frequency ω and temperature T is

$$\bar{n}_{\mathrm{th}}(\omega, T) = \frac{1}{\exp\left(\hbar\omega/k_{\mathrm{B}}T\right) - 1}. \tag{2.45}$$

A convenient rule-of-thumb is that the quantum regime ($\bar{n}_{\text{th}} \ll 1$) requires $k_B T \ll \hbar\omega$. For a typical 5 GHz magnon, this means $T \ll 240$ mK. Dilution refrigerators operate well below this threshold (e.g., 10–20 mK), ensuring that for GHz-frequency magnons, the system is deep in the quantum ground state ($\bar{n}_{\text{th}} \simeq 0$). This is the regime that permits single-magnon spectroscopy, vacuum Rabi splittings, and the few-excitation protocols developed in this dissertation [31], [33], [40]. All subsequent analysis assumes operation at these cryogenic temperatures.

2.3.2 Hybrid Coupling Rates

The interaction between a magnon mode and another quantum mode (like a cavity photon or a qubit) is fundamentally an exchange interaction. For a single spin $\hat{\boldsymbol{S}}$ interacting with a quantized magnetic field $\boldsymbol{B}(\boldsymbol{r})$, the interaction Hamiltonian is $\hat{H}_{\text{int}} = g\mu_B \hat{\boldsymbol{S}} \cdot \boldsymbol{B}(\boldsymbol{r})$. For an ensemble of N coherently precessing spins, this interaction is collectively enhanced by $\sqrt{N}$ [21], [22]. Quantizing both the magnon mode (with operators $\hat{m}, \hat{m}^\dagger$) and the other mode (e.g., a photon, $\hat{a}, \hat{a}^\dagger$), the interaction Hamiltonian takes the Jaynes-Cummings form:

$$\hat{H}_{\text{int}} = \hbar g_{\text{eff}} \left(\hat{a}^\dagger \hat{m} + \hat{a}\hat{m}^\dagger\right), \qquad g_{\text{eff}} = \gamma \sqrt{\frac{\mu_0 \hbar\omega}{2V_{\text{mode}}}} \sqrt{N}, \tag{2.46}$$

where g_{eff} is the effective coupling rate. The large spin density in YIG ($n_s \sim 10^{22}\ \text{cm}^{-3}$) and the strong field confinement of SC resonators (small V_{mode}) allow this coupling to be very large. Experimentally, $g_{\text{eff}}/2\pi$ readily reaches 10–100 MHz in both 3D cavity and planar resonator geometries [30], [31], [32], [34].

2.3.3 Coupling Regimes and Cooperativity

When two modes (e.g., a magnon ω_m and a qubit ω_q) are brought into resonance, their interaction g_{eff} can manifest in two distinct ways, depending on the system's dissipation rates and the *nature* of the coupling itself.

The first regime is **Coherent Coupling**. If the coupling rate is much larger than the decay rates of both modes ($g_{\text{eff}} \gg \Gamma_q, \Gamma_m$), the system is in the **strong coupling regime**. Here, energy is coherently exchanged between the modes, leading to Rabi oscillations. In the frequency domain, this is observed as a clear **level repulsion** or ”avoided crossing,” where the hybrid eigenmodes split by a gap of $2g_{\text{eff}}$.

The second regime is **Dissipative Coupling**. If the coupling is mediated by a shared dissipative channel (like a transmission line, as discussed in Chapter 4), the interaction can be dissipative. This can lead to the counter-intuitive phenomenon of **level attraction**, where the two modes merge in frequency and their linewidths bifurcate, with one mode becoming very long-lived (a ”dark” state) and the other very short-lived [126]. This is often associated with exceptional points (EPs) in non-Hermitian systems.

These two distinct coupling regimes are not necessarily dependent on physical dissipation, but rather on the *phase* of the coupling terms. This distinction can be formally modeled by introducing a relative phase φ into the coupling terms, as shown in the classical model in Chapter 3. For a general two-mode system, the coupled equations can be written as:

$$\begin{aligned} \frac{da_1}{dt} + i\omega_1\, a_1 &= -ig_1 e^{i\varphi} a_{\text{m}}, \\ \frac{da_m}{dt} + i\omega_{\text{m}}\, a_{\text{m}} &= -ig_1^* a_1. \end{aligned} \tag{2.47}$$

The phase φ, which in a physical system might be set by the propagation distance along a transmission line (as shown in Section 4.2), dictates the nature of the interaction. When $\varphi = 0$, the coupling is purely coherent (Hermitian) and results in level repulsion. When $\varphi = \pi$, the coupling is purely dissipative (anti-Hermitian) and results in level attraction.

For quantum information processing, the coherent coupling regime ($\varphi = 0$) is essential. The key figure of merit is the **cooperativity** C, which compares the coherent coupling rate to the geometric mean of the dissipation rates:

$$C = \frac{g_{\text{eff}}^2}{\Gamma_q \Gamma_m}. \tag{2.48}$$

The condition $C \gg 1$ signifies that many coherent oscillations can occur before the information is lost to decoherence, and it is the primary requirement for the protocols in this dissertation [39], [40].

2.3.4 Material and Geometry Considerations

The coupling rate $g_{\text{eff}} \propto \sqrt{N_s}\, B_{\text{vac}}\, \eta$ is set by the total number of spins N_s, the vacuum field confinement B_{vac} (related to mode volume), and the geometric overlap η. The platform choice is therefore a trade-off between these parameters and the material's intrinsic damping.

YIG's exceptionally low damping ($\alpha_{\text{G}} \sim 10^{-5}$) enables large cooperativity C [42]. YIG spheres maximize the spin number N_s and can achieve excellent mode matching in 3D cavities, resulting in the highest C. Planar CPW resonators with epitaxial YIG films offer superior on-chip integration and strong field confinement, trading a smaller N_s for a smaller mode volume, and still achieve $C \gg 1$. In contrast, Py has a higher spin density (which boosts g_{eff}), but its extremely large damping ($\alpha_{\text{G}} \sim 10^{-2}$) results in a low $C < 10$, keeping it in the weak-coupling regime unsuitable for quantum operations.

Table 2.4: Representative strong-coupling benchmarks for common platforms at cryogenic temperatures (values compiled from [30], [31], [32], [33], [34], [35]). Here Γ_p is photon/resonator decay and Γ_m is magnon decay.

Platform	$g/2\pi$ (MHz)	$\Gamma_p/2\pi$ (MHz)	$\Gamma_m/2\pi$ (MHz)	C
3D cavity + YIG sphere	50–100	1–2	0.1–1	10^3–10^4
Planar CPW + YIG film	10–30	2–5	1–5	10–10^2
Planar CPW + Py stripe	20–50	5–10	10–20	< 10

2.3.5 Noise Hierarchy and Modeling Assumptions

The primary justification for our theoretical model, which focuses on magnon dynamics, comes from a simple comparison of timescales. The coherent operations we develop in this dissertation, such as a SWAP gate, occur on a timescale $t_g \sim \pi/(2g_{\text{eff}})$. Given $g_{\text{eff}}/2\pi \sim 10 - 30$ MHz (from Table 2.4), a typical gate time is $t_g \sim 10 - 50$ nanoseconds.

We can now compare the noise contributions from the qubit and the magnon over this gate time. For a state-of-the-art qubit (from Table 2.3), coherence times are $T_1, T_2 \sim 100\ \mu$s, giving a corresponding error rate of $\Gamma_q \sim 1/T_1 \sim 10$ kHz. For a high-quality YIG magnon (from Table 2.1), coherence times are $\tau_m \sim 200 - 1000$ ns, giving a much faster error rate of $\Gamma_m \sim 1/\tau_m \sim 1 - 5$ MHz.

This establishes a clear noise hierarchy: $\Gamma_q \ll \Gamma_m$. The error contribution from magnon decoherence ($\varepsilon_m \approx \Gamma_m t_g$) is one to two orders of magnitude greater than the error from qubit decoherence ($\varepsilon_q \approx \Gamma_q t_g$). Therefore, for the fast, magnon-mediated protocols developed in this dissertation, it is a well-justified approximation to neglect qubit noise and include only the dominant magnon collapse operators in the Lindblad master equation.

2.4 Conclusion

This chapter has established the foundational pillars for the dissertation. We began in Section 2.1 by deriving magnons as bosonic quasiparticles, establishing their dispersion, resonance conditions, and decoherence mechanisms. In Section 2.2, we introduced the qubit as a two-level system, defined the rules for quantum operations, and established the transmon model. Finally, in Section 2.3, we synthesized these concepts into a unified hybrid framework, defined the coupling regimes, and—most importantly—established the noise hierarchy $\Gamma_q \ll \Gamma_m$. This hierarchy is the central modeling assumption that justifies our focus on magnon dynamics. With this physical and mathematical foundation in place, we are now prepared to construct the formal simulation methods in Chapter 3.

CHAPTER THREE

METHODS

The purpose of this chapter is to introduce the mathematical and numerical methods that will be utilized in the remainder of this dissertation to analyze hybrid quantum magnonic systems. This chapter lays out a geometry-agnostic modeling and simulation framework for these systems, applicable to static, quasi-static, and dynamically-tuned scenarios. The goal is to define the state spaces for our Q-qubit and M-magnon systems, construct the classical and quantum Hamiltonians, and detail the numerical methods used to solve for both closed-system (unitary) and open-system (dissipative) time evolution. The same formal apparatus supports all protocols developed in later chapters. Ergo, the treatment is geometry-agnostic at the level of theory while remaining parameterized by the physical and material scales summarized in Chapter 2, so platform- and geometry-specific constraints can be introduced later without changing the core methodology.

3.1 State Spaces and Notation

We consider our model hybrid quantum magnonic system to be a composite quantum system of Q qubit modes $|q\rangle$ and M magnon modes $|m\rangle$ with a tensor-product Hilbert space $\mathcal{H}^{QM}$ defined such that:

$$\mathcal{H}^{QM} = \mathcal{H}^{Q} \otimes \mathcal{H}^{M} = \left(\bigotimes_{j=1}^{Q} \mathcal{H}_{q_j} \right) \otimes \left(\bigotimes_{\alpha=1}^{M} \mathcal{H}_{m_\alpha} \right). \tag{3.1}$$

Each of the Q qubit modes $|q\rangle$ is treated as a two-level system (a fermionic quantum object) described by Fock states $|0\rangle$ and $|1\rangle$. The qubit creation ($\hat{q}^\dagger$) and annihilation ($\hat{q}$) operators are defined by their actions:

$$\hat{q}^\dagger |0\rangle = |1\rangle\,, \qquad \hat{q}\,|1\rangle = |0\rangle\,, \tag{3.2}$$

with each qubit subspace defined by:

$$\mathcal{H}_{q_j} = \mathrm{span}\{\left|q_j\right\rangle : q_j = 0, 1\}, \qquad \{\hat{q}_j, \hat{q}_k^\dagger\} = \delta_{jk}. \tag{3.3}$$

Each of the M magnon modes is a bosonic quantum object described by Fock states $|m\rangle$ with a non-negative integer number of magnons m. The magnon creation ($\hat{m}^\dagger$) and annihilation ($\hat{m}$) operators are defined by:

$$\hat{m}^\dagger |m\rangle = \sqrt{m+1}\, |m+1\rangle\,, \qquad \hat{m}\, |m\rangle = \sqrt{m}\, |m-1\rangle\,, \tag{3.4}$$

with each magnon subspace defined by:

$$\mathcal{H}_{m_\alpha} = \mathrm{span}\{|m_\alpha\rangle : m_\alpha = 0, 1, ..., m_\alpha^{\max}\}, \qquad [\hat{m}_\alpha, \hat{m}_\beta^\dagger] = \delta_{\alpha\beta}, \tag{3.5}$$

where $m_\alpha^{\max}$ is set by working assumptions and a maximum number of excitations $N_{\max}$. This leads to the phase space of our model hybrid magnonic system spanned by the tensor-product states $|\mathbf{q}\rangle \otimes |\mathbf{m}\rangle = |\mathbf{q};\mathbf{m}\rangle$ with the basis states of the full system defined by

$$|\mathbf{q};\mathbf{m}\rangle = \left|q_1, ..., q_Q;\, m_1, ..., m_M\right\rangle. \tag{3.6}$$

In this $\left|q_1, ..., q_Q;\, m_1, ..., m_M\right\rangle$ notation, the semicolon explicitly separates the qubit subspace (listed first, on the left) from the magnon subspace (listed second, on the right). For systems where $Q = 0$ (i.e., no qubits are present), the qubit entry is left blank, as in $|;1,1\rangle$ for a two-magnon state.

Our hybrid quantum magnonic system is further described by the total number of quanta N, which is defined by the total number operator $\hat{N}$ given by

$$\hat{N} = \sum_{j\in Q} \hat{q}_j^\dagger \hat{q}_j \;+\; \sum_{\alpha\in M} \hat{m}_\alpha^\dagger \hat{m}_\alpha. \tag{3.7}$$

Functionally, this total number of quanta N is truncated to a maximum number of excitations $N_{\max}$, which is set by the particular application of choice. This means that the basis states, and therefore the phase space of our system, can be set by choice of the number of qubit modes Q, the number of magnon modes M, and the maximum number of excitations N_{max}. In this dissertation, we consider the combinations of (Q, M, N_{max}) listed in Table 3.1, which summarizes the non-trivial excitation subspaces modeled in this dissertation.

Table 3.1: Summary of the non-trivial excitation subspaces modeled in this dissertation, detailing their composition, dimension, basis state ordering, and relevant chapters.

System (Q, M)	**Subspace** (n)	**Dim.** (D_n)	**Basis States** $\lvert q_1, \ldots; m_1, \ldots\rangle$	**Chapters**
(1, 1)	1	2	$\{\lvert 1; 0\rangle, \lvert 0; 1\rangle\}$	7, 8 (and 5)
(0, 2)	1	2	$\{\lvert ; 1, 0\rangle, \lvert ; 0, 1\rangle\}$	6
(0, 2)	2	3	$\{\lvert ; 2, 0\rangle, \lvert ; 1, 1\rangle, \lvert ; 0, 2\rangle\}$	6
(2, 1)	1	3	$\{\lvert 1, 0; 0\rangle, \lvert 0, 1; 0\rangle, \lvert 0, 0; 1\rangle\}$	8 (and 5)
(2, 1)	2	4	$\{\lvert 1, 1; 0\rangle, \lvert 1, 0; 1\rangle, \lvert 0, 1; 1\rangle, \lvert 0, 0; 2\rangle\}$	8

3.2 Quantum Hamiltonian Model

In this dissertation, we study a model hybrid quantum magnonic system comprising Q qubit modes $\lvert q_j\rangle$ with fixed resonant frequencies ω_{q_j} and M magnon modes $\lvert m_\alpha\rangle$ with dynamically tunable resonant frequencies $\omega_{m_\alpha}(t)$. The coupling between each j-th qubit mode and α-th magnon mode is described by a rate $g_{j\alpha}$, and the coupling between each α-th and β-th magnon mode is described by a rate $\tilde{g}_{\alpha\beta}$, while the qubit modes are assumed to be mutually uncoupled by construction and convention to prevent such potential for cross-talk. The Hamiltonian $\hat{\mathcal{H}}(t)$ of this system can then be written as:

$$
\begin{aligned}
\hat{\mathcal{H}}(t)/\hbar = &\sum_{j\in Q} \omega_{q_j} \hat{q}_j^\dagger \hat{q}_j \; + \sum_{\alpha\in M} \omega_{m_\alpha}(t) \hat{m}_\alpha^\dagger \hat{m}_\alpha \\
&+ \sum_{\substack{j\in Q\\ \alpha\in M}} \left(g_{j\alpha} \hat{q}_j^\dagger \hat{m}_\alpha \; + \; g_{j\alpha}^* \hat{m}_\alpha^\dagger \hat{q}_j \right) \\
&+ \sum_{\substack{\alpha,\beta\in M\\ \alpha<\beta}} \left(\tilde{g}_{\alpha\beta} \hat{m}_\alpha^\dagger \hat{m}_\beta \; + \; \tilde{g}_{\alpha\beta}^* \hat{m}_\beta^\dagger \hat{m}_\alpha \right)
\end{aligned}
\quad , \tag{3.8}
$$

where the sums run over all Q qubits and M magnons.

Note that the Hamiltonian $\hat{\mathcal{H}}(t)$ [Eq. (3.8)] commutes with the total number operator $\hat{\mathcal{N}}$ [Eq. (3.7)], such that $[\hat{\mathcal{H}}, \hat{\mathcal{N}}] = 0$, and thus conserves the total number of quanta N. For notational simplicity, from Eq. (3.7) we can define q as the total number of qubit excitations and m as the total number of magnon excitations in a given state, such that the conserved quantity is

$$
N = q + m = \sum_{j\in Q} q_j \; + \sum_{\alpha\in M} m_\alpha . \tag{3.9}
$$

This conservation of N quanta means that, in the absence of noise and any interactions to induce a change in the total number of quanta N, the dynamics of the system can be considered separately in finite-dimensional subspaces corresponding to different quanta N. This leads directly to a block-diagonal decomposition of the Hilbert space. Each excitation manifold therefore corresponds to an invariant subspace with fixed dimension set by the particular combination of $(Q, M, N_{\max})$, where the specific examples we treat in this dissertation can be found in Table 3.1. Accordingly, the full Hamiltonian can be written as a direct sum over these number-conserving subspaces:

$$
\hat{\mathcal{H}}(t) = \bigoplus_{n=0}^{N_{\max}} \hat{\mathcal{H}}_n(t) = \hat{\mathcal{H}}_0(t) \oplus \hat{\mathcal{H}}_1(t) \oplus \cdots \oplus \hat{\mathcal{H}}_{N_{\max}}(t). \tag{3.10}
$$

This decomposition means the state of the system $|\psi(t)\rangle$ can be written as a sum over each N-subspace state $|\psi_n(t)\rangle$:

$$|\psi(t)\rangle = \sum_{n=0}^{N_{\max}} |\psi_n(t)\rangle = |\psi_0(t)\rangle + |\psi_1(t)\rangle + \cdots + \left|\psi_{N_{\max}}(t)\right\rangle, \tag{3.11}$$

where each N-subspace state $|\psi_N(t)\rangle$ is a superposition of all basis states with exactly N excitations:

$$|\psi_N(t)\rangle = \sum_{q+m=N} c_{\mathbf{q};\mathbf{m}}(t)\,|\mathbf{q};\mathbf{m}\rangle\,. \tag{3.12}$$

The overall state of the system then evolves according to the Schrödinger equation, $\partial\,|\psi(t)\rangle\,/\partial t = -(i/\hbar)\,\hat{\mathcal{H}}(t)\,|\psi(t)\rangle$, which therefore separates into a set of smaller, independent linear algebra problems, which can be visualized by the explicit block-diagonal structure of the Hamiltonian matrix:

$$\frac{d}{dt}\begin{pmatrix} \mathbf{c}_0(t) \\ \mathbf{c}_1(t) \\ \vdots \\ \mathbf{c}_{N_{\max}}(t) \end{pmatrix} = -\frac{i}{\hbar}\begin{pmatrix} \hat{\mathcal{H}}_0(t) & 0 & \cdots & 0 \\ 0 & \hat{\mathcal{H}}_1(t) & \cdots & 0 \\ \vdots & \vdots & \ddots & \vdots \\ 0 & 0 & \cdots & \hat{\mathcal{H}}_{N_{\max}}(t) \end{pmatrix}\begin{pmatrix} \mathbf{c}_0(t) \\ \mathbf{c}_1(t) \\ \vdots \\ \mathbf{c}_{N_{\max}}(t) \end{pmatrix}, \tag{3.13}$$

where we have written for brevity the vector of probability amplitudes $\mathbf{c}_n(t)$ for the $\mathcal{H}_n$ subspace. This decomposition greatly reduces the computational complexity.

3.3 Specific Subspace Models

While the operator formalism in Eq. (3.8) is general, all numerical simulations work with the specific matrix representations of the Hamiltonian in each N-excitation subspace. This section provides these explicit matrices for the key quantum protocols analyzed in this dissertation, defining the basis state ordering used in our simulations, which corresponds to Table 3.1. We operate in a rotating frame, so the $N = 0$ subspace $\mathcal{H}_0$, spanned by $|\mathrm{q} = 0; \mathrm{m} = 0\rangle$, is trivial: $\hat{\mathcal{H}}_0 = [0]$.

3.3.1 Case 1: (Q=1, M=1, N=1) – Qubit-Magnon Exchange

This is the fundamental two-level system for single-qubit gates (Chapter 8) and the magnon-qubit Mach–Zehnder interferometer (MZI) (Chapter 7). The $N = 1$ subspace is 2-dimensional, spanned by the basis vector:

$$\mathbf{c}_1 = \begin{pmatrix} c_{q_1=1;m_1=0} \\ c_{q_1=0;m_1=1} \end{pmatrix}, \qquad \text{Basis}: \quad \{|1;0\rangle, |0;1\rangle\}. \tag{3.14}$$

The corresponding Hamiltonian matrix $\hat{\mathcal{H}}_1(t)$ is:

$$\hat{\mathcal{H}}_1(t) = \hbar \begin{pmatrix} \omega_{q1} & g_{11}^* \\ g_{11} & \omega_{m1}(t) \end{pmatrix}. \tag{3.15}$$

3.3.2 Case 2: (Q=0, M=2, N ≤ 2) – Two-Magnon Interference

This system is used for two-magnon interference (Chapter 6). The $N = 1$ subspace is 2-dimensional, spanned by the basis vector:

$$\mathbf{c}_1 = \begin{pmatrix} c_{;m_1=1,m_2=0} \\ c_{;m_1=0,m_2=1} \end{pmatrix}, \qquad \text{Basis}: \quad \{|;1,0\rangle, |;0,1\rangle\}. \tag{3.16}$$

The Hamiltonian $\hat{\mathcal{H}}_1(t)$ is:

$$\hat{\mathcal{H}}_1(t) = \hbar \begin{pmatrix} \omega_{m1}(t) & \tilde{g}_{12}^* \\ \tilde{g}_{12} & \omega_{m2}(t) \end{pmatrix}. \tag{3.17}$$

The $N = 2$ subspace is 3-dimensional, spanned by the basis vector:

$$\mathbf{c}_2 = \begin{pmatrix} c_{;2,0} \\ c_{;1,1} \\ c_{;0,2} \end{pmatrix}, \qquad \text{Basis}: \quad \{|;2,0\rangle, |;1,1\rangle, |;0,2\rangle\}. \tag{3.18}$$

The Hamiltonian $\hat{\mathcal{H}}_2(t)$, derived from Eq. (3.8), is:

$$\hat{\mathcal{H}}_2(t) = \hbar \begin{pmatrix} 2\omega_{m1}(t) & \sqrt{2}\tilde{g}_{12}^* & 0 \\ \sqrt{2}\tilde{g}_{12} & \omega_{m1}(t) + \omega_{m2}(t) & \sqrt{2}\tilde{g}_{12}^* \\ 0 & \sqrt{2}\tilde{g}_{12} & 2\omega_{m2}(t) \end{pmatrix}. \tag{3.19}$$

3.3.3 Case 3: (Q=2, M=1, N ≤ 2) – Two-Qubit Gates

This system is used for realizing universal two-qubit gates (Chapter 8). The $N = 1$ subspace is 3-dimensional, spanned by the basis vector:

$$\mathbf{c}_1 = \begin{pmatrix} c_{1,0;0} \\ c_{0,1;0} \\ c_{0,0;1} \end{pmatrix}, \qquad \text{Basis :} \quad \{|1,0;0\rangle, |0,1;0\rangle, |0,0;1\rangle\}. \tag{3.20}$$

The Hamiltonian $\hat{\mathcal{H}}_1(t)$ is:

$$\hat{\mathcal{H}}_1(t) = \hbar \begin{pmatrix} \omega_{q1} & 0 & g_1^* \\ 0 & \omega_{q2} & g_2^* \\ g_1 & g_2 & \omega_{m1}(t) \end{pmatrix}. \tag{3.21}$$

The $N = 2$ subspace is 4-dimensional, spanned by the basis vector:

$$\mathbf{c}_2 = \begin{pmatrix} c_{1,1;0} \\ c_{1,0;1} \\ c_{0,1;1} \\ c_{0,0;2} \end{pmatrix}, \qquad \text{Basis :} \quad \{|1,1;0\rangle, |1,0;1\rangle, |0,1;1\rangle, |0,0;2\rangle\}. \tag{3.22}$$

The Hamiltonian $\hat{\mathcal{H}}_2(t)$, derived from Eq. (3.8), is:

$$\hat{\mathcal{H}}_2(t) = \hbar \begin{pmatrix} \omega_{q1} + \omega_{q2} & g_2^* & g_1^* & 0 \\ g_2 & \omega_{q1} + \omega_{m1}(t) & 0 & \sqrt{2} g_1^* \\ g_1 & 0 & \omega_{q2} + \omega_{m1}(t) & \sqrt{2} g_2^* \\ 0 & \sqrt{2} g_1 & \sqrt{2} g_2 & 2\omega_{m1}(t) \end{pmatrix}. \tag{3.23}$$

3.4 Classical Model and Quantum Equivalence

For some analyses, particularly in Chapters 4 and 5, it is simpler to use a classical model of coupled harmonic oscillators. This model describes the dynamics of the classical complex amplitudes of the modes, $a_j(t)$ (for qubits/resonators) and $a_\alpha(t)$ (for magnons). The general, damped equations of motion are:

$$\begin{aligned} \dot{a}_j &= -(i\omega_{q_j} + \Gamma_j^{(q)}) a_j - i \sum_{\alpha \in M} g_{j\alpha} a_\alpha \\ \dot{a}_\alpha &= -(i\omega_{m_\alpha}(t) + \Gamma_\alpha^{(m)}) a_\alpha - i \sum_{j \in Q} g_{j\alpha}^* a_j - i \sum_{\beta \neq \alpha} \tilde{g}_{\alpha\beta} a_\beta \end{aligned} \tag{3.24}$$

where $\Gamma_j^{(q)}$ and $\Gamma_\alpha^{(m)}$ are the classical phenomenological decay rates, which are the classical analogues of the quantum relaxation rates (e.g., Γ_q and Γ_m) defined in Chapter 2.

A key feature of this formalism is its direct connection to the quantum model. In the **single-excitation ($N = 1$) subspace** and in the **absence of damping** ($\Gamma = 0$), these classical equations of motion (3.24) are **formally identical** to the quantum Heisenberg equations of motion for the annihilation operators (e.g., $i\hbar\dot{\hat{q}}_j = [\hat{q}_j, \hat{\mathcal{H}}]$). This equivalence provides a powerful mapping: the classical "power" or "population" $|a_j(t)|^2$ is analogous to the quantum probability $|c_j(t)|^2$ of finding the single excitation in mode j. This allows us to use the simpler classical model to characterize and design protocols (as in Chapters 4 and 5), with the knowledge that the results are directly applicable to the single-excitation quantum regime.

3.5 Closed System Time Evolution

In the absence of noise, the evolution of the quantum state $|\psi(t)\rangle$ is governed by the Schrödinger equation. The state at time t is related to the initial state $|\psi(t_0)\rangle$ by a unitary propagator $\hat{\mathcal{U}}(t, t_0)$:

$$|\psi(t)\rangle = \hat{\mathcal{U}}(t, t_0)\, |\psi(t_0)\rangle = \mathcal{T} \exp\left(-\frac{i}{\hbar} \int_{t_0}^{t} \hat{\mathcal{H}}(s)\, ds\right) |\psi(t_0)\rangle\,, \tag{3.25}$$

where $\mathcal{T}$ denotes the time-ordering operation. When $\hat{\mathcal{H}}$ is constant in time, the propagator $\hat{\mathcal{U}}(t, t_0)$ simplifies to a standard matrix exponential:

$$\hat{\mathcal{U}}(t, t_0) = \exp\Big((-i/\hbar)\, \hat{\mathcal{H}}[\Delta\omega]\, (t - t_0)\Big) = \hat{\mathcal{U}}_0(\Delta\omega, \tau), \tag{3.26}$$

and the result of the evolution depends only on the magnon resonance frequency gap $\Delta\omega$ (contained in $\hat{\mathcal{H}}[\Delta\omega]$) and the interaction time $\tau = t - t_0$.

It is important to note that outside of Chapters 4, 5, and 7 in this dissertation, we do not include non-number-conserving noise channels, such as magnon loss, or number-conserving channels, such as phase noise, as these depend on the specific physical implementation and fall outside the scope of our geometry-agnostic model. While such effects are important in experimental systems and may result in partially mixed states, they are not intrinsic to the general quantum magnonic protocols analyzed here. Furthermore, their impact on the outcome of such protocols may be quite dependent on the geometry in-which they occur. Recognizing this, we present a method for recovering the rates of these noise channels in Chapter 7 and detail the methodology for inclusion of these dissipative terms in the following section. By focusing on the idealized, unitary dynamics, prior to this, we isolate the coherent features of dynamic magnon-mediated interactions and investigate to what extent can we manipulate quantum information and enrich quantum systems through dynamic tuning of the interaction time τ and magnon resonance frequency gap $\Delta\omega$.

3.6 Open System Time Evolution

To simulate evolution of our system with noise and effectively model the quantum decoherence processes (e.g., magnon damping, dephasing) as it evolves, we must use the GKSL quantum master equation [92], [140], [141]. This equation governs the evolution of the system's density matrix $\rho(t)$:

$$\dot{\rho}(t) = \mathcal{L}[\rho(t)] = (-i/\hbar)\,[\hat{\mathcal{H}}(t), \rho(t)] + \sum_k \Gamma_k\, \mathcal{D}[\hat{L}_k](\rho(t)). \tag{3.27}$$

The first term is the coherent, unitary evolution of the density matrix $\rho(t)$ by way of the von Neumann equation. The second term is the "dissipator," $\mathcal{D}$ which describes noise processes of the Lindblad jump operators $\hat{L}_k$. The density matrix is $\rho(t) = |\psi(t)\rangle\langle\psi(t)|$. The commutator is $[A, B] = AB - BA$. Each noise channel k is defined by a noise rate Γ_k (such as $\Gamma_1^{(q)}$ or Γ_m) and a Lindblad jump operator $\hat{L}_k$. The dissipator $\mathcal{D}[\hat{L}_k]$ has the form acting on some operator $\hat{O}$ as

$$\mathcal{D}[\hat{L}_k](\hat{O}) = \hat{L}_k \cdot \hat{O} \cdot \hat{L}_k^\dagger - (1/2)\{\hat{L}_k^\dagger \cdot \hat{L}_k, \hat{O}\}, \tag{3.28}$$

where $\{A, B\} = AB + BA$ is the anti-commutator. As justified in Section 2.3.5, our simulations will primarily include the dominant magnon decay channel, where $\hat{L} = \hat{m}_\alpha$ for a given magnon mode α and $\Gamma_k = \Gamma_m$. When dealing with multiple noise channels, such as the case in Chapter 7, it is important to note that the dissipator is linear such that for some set of jump operators $\hat{L} = \hat{L}_1 + \hat{L}_2$, we have

$$\mathcal{D}[\hat{L}](\hat{O}) = \mathcal{D}[\hat{L}_1 + \hat{L}_2](\hat{O}) = \mathcal{D}[\hat{L}_1](\hat{O}) + \mathcal{D}[\hat{L}_2](\hat{O}). \tag{3.29}$$

3.7 Numerical Simulation Methods

The numerical simulation methods we employ in this dissertation must numerically solve for the time evolution in either an open or a closed system. This means that we must use the same method to compute and suitably solve the propagators for both the closed-system state vector $|\psi(t)\rangle$ of the Schrödinger equation (3.25) and the open-system density matrix $\rho(t)$ of the GKSL master equation (3.27).

Vectorization. To do this, both problems are first unified into a standard vector-matrix differential equation $\dot{\mathbf{x}}(t) = \hat{A}(t)\mathbf{x}(t)$, which is then solved using one of three methods detailed below, depending on the time-dependence of $\hat{A}(t)$. In either the open or the closed case, the first step for each problem is to vectorize the system.

The closed-system problem, $\partial |\psi(t)\rangle / \partial t = -(i/\hbar)\hat{\mathcal{H}}(t) |\psi(t)\rangle$, is the simpler case. The state $|\psi(t)\rangle$ is a vector of dimension $D_n \times 1$ (the dimension of the relevant excitation subspace n, see Table 3.1), and the Hamiltonian $\hat{\mathcal{H}}(t)$ is a $D_n \times D_n$ matrix. The equation is therefore already in a "directly vectorized" form, $\dot{\mathbf{c}}(t) = (-i/\hbar)\hat{\mathcal{H}}(t)\mathbf{c}(t)$, where $\mathbf{c}(t)$ is the vector of probability amplitudes $c_{\mathbf{q};\mathbf{m}}(t)$.

The open-system problem, $\dot{\rho}(t) = \mathcal{L}[\rho(t)]$, is more complex as it describes the evolution of a $D_n \times D_n$ *matrix*. To solve this using standard linear algebra, we first **vectorize** the density matrix ρ into a single $D_n^2 \times 1$ column vector, $\boldsymbol{\rho} = \mathrm{vec}(\rho)$. This transforms the GKSL master equation (3.27) into a form analogous to the Schrödinger equation:

$$\dot{\boldsymbol{\rho}}(t) = \hat{\mathcal{L}}(t) \cdot \boldsymbol{\rho}(t), \tag{3.30}$$

where $\hat{\mathcal{L}}(t)$ is a $D_n^2 \times D_n^2$ matrix known as the Liouvillian superoperator. This Liouvillian contains all information about both the coherent ($[\hat{\mathcal{H}}, \,\cdot\,]$) and dissipative ($\mathcal{D}[\hat{L}_k](\,\cdot\,)$) evolution.

Simulation. With both problems in the form of a standard vector-matrix differential equation $\dot{\mathbf{x}}(t) = \hat{A}(t)\mathbf{x}(t)$, we employ three main solution methods depending on the time-dependence of the operator $\hat{A}(t)$ (which is either $(-i/\hbar)\hat{\mathcal{H}}(t)$ or $\hat{\mathcal{L}}(t)$).

First, for **Time-Independent Evolution**, where $\hat{A}$ is constant over a duration τ (as in a rectangular pulse at a constant frequency gap $\Delta\omega$), the solution is a single matrix exponential:

$$\mathbf{x}(t) = \exp\Big(\hat{A}[\Delta\omega]\,\tau\Big)\,\mathbf{x}(0) = \hat{\mathcal{U}}_0(\Delta\omega, \tau)\mathbf{x}(t_0). \tag{3.31}$$

Second, for **Piecewise-Constant Evolution**, where the protocol is a sequence of rectangular pulses (e.g., the "*ABC*" protocol in Chapter 8), the total propagator is simply the product of the individual matrix exponentials for each constant segment:

$$\hat{\mathcal{U}}_{\text{total}} = \hat{\mathcal{U}}_n(\Delta\omega_n,\, \tau_n)\,\cdots\,\hat{\mathcal{U}}_2(\Delta\omega_2,\, \tau_2)\,\hat{\mathcal{U}}_1(\Delta\omega_1,\, \tau_1). \tag{3.32}$$

Third, for **Time-Dependent Evolution**, where $\hat{A}(t)$ is continuously time-dependent (as in a linear or parabolic ramp), the propagator is the time-ordered exponential $\mathcal{T}\exp\left(\int_{t_0}^{t}\hat{A}(s)\,ds\right)$. We solve this numerically using the **Magnus expansion** [142], [143], which approximates the propagator as a single exponential:

$$\mathcal{T}\exp\left(\int_{t_0}^{t}\hat{A}(s)\,ds\right) = \exp\left(\Omega(t, t_0)\right). \tag{3.33}$$

The exponent $\Omega(t, 0) = \Omega(t)$ is an infinite series,

$$\Omega(t) = \sum_{k=1}^{\infty} \Omega_k(t) = \Omega_1(t) + \Omega_2(t) + \ldots, \tag{3.34}$$

where the first three terms [141], [142] are:

$$\Omega_1(t, t_0) = \int_{t_0}^{t} \hat{A}(s_1)\, ds_1, \tag{3.35}$$

$$\Omega_2(t, t_0) = \frac{1}{2} \int_{t_0}^{t} ds_1 \int_{t_0}^{s_1} ds_2\, [\hat{A}(s_1), \hat{A}(s_2)], \tag{3.36}$$

$$\Omega_3(t, t_0) = \frac{1}{6} \int_{t_0}^{t} ds_1 \int_{t_0}^{s_1} ds_2 \int_{t_0}^{s_2} ds_3 \left(\big[\hat{A}_1, [\hat{A}_2, \hat{A}_3]\big] + \big[\hat{A}_3, [\hat{A}_2, \hat{A}_1]\big] \right), \tag{3.37}$$

and we have written $\hat{A}(s_i) \equiv \hat{A}_i$ starting at the $k = 3$ third order Magnus expansion for brevity. In our simulations, we divide the evolution into small steps Δt and compute this series, which is then exponentiated to find the propagator for that step. This method is highly stable as it provides an approximate solution to the *exact function* (the propagator), rather than an exact solution to an *approximated function* (as in a time-slicing method like Runge-Kutta), thus preventing unphysical behavior. We typically truncate this series at the second order ($\Omega \approx \Omega_1 + \Omega_2$) but can employ up to fourth or sixth-order expansions as needed for sufficient accuracy.

3.8 Conclusion

This chapter has established the complete theoretical and numerical framework for this dissertation. We have defined the quantum and classical models, shown their equivalence in the single-excitation limit, and provided the explicit Hamiltonian matrices that are simulated. Finally, we detailed the numerical methods—from simple matrix exponentials to the Magnus expansion—used to solve their time evolution. With these tools in hand, we can now proceed to analyze specific systems and protocols, beginning with the classical, static analysis of the candidate experimental platform in Chapter 4.

CHAPTER FOUR

CANDIDATE EXPERIMENTAL PLATFORM

While the dynamic protocols developed in this dissertation are geometry-agnostic, it is useful to ground them in a concrete, experimentally-realized platform. This chapter describes a scalable, modular SC circuit platform developed by our collaborators at Argonne National Laboratory that is a near-term candidate for implementing these protocols.

This chapter is divided into two main parts. The first section, Section 4.1, provides a descriptive overview of the experimental architecture, which was fabricated and measured by our collaborators. The second section, Section 4.2, presents the theoretical network model that we developed to analyze the platform. This theory derives the transmission-line-mediated coupling between remote resonators, providing the formal basis for understanding the crossover from coherent (level repulsion) to dissipative (level attraction) coupling. The analysis in this chapter is entirely classical, modeling the system as a set of coupled harmonic oscillators. As established in Section 3.4, the results of this classical model are formally equivalent to the single-excitation ($N = 1$) quantum regime, justifying its use for protocol design.

4.1 Architecture and Concept

The candidate platform shown here is modular and scalable, and it has advanced through successive iterations by our collaborators at Argonne. Device fabrication and measurements were performed by our collaborators, while our contribution is the phenomenological modeling and network analysis of the coupled magnon–photon circuits.

4.1.1 Local Sphere–Resonator Module

The basic building block, shown in Fig. 4.1, is a **local sphere-resonator module**. A single-crystal YIG sphere is mounted in a lithographically-defined hole on a Si, silicon (Si) substrate and inductively coupled to a SC loop resonator. This loop antenna strongly couples the localized microwave mode of the resonator to the uniform (Kittel) magnon mode of the YIG sphere. The resonator can then be interfaced with a CPW for microwave readout and control. In this configuration the loop current provides the near-field that couples to the uniform magnon mode; the external line defines a reference port for excitation and readout that we use later in network descriptions.

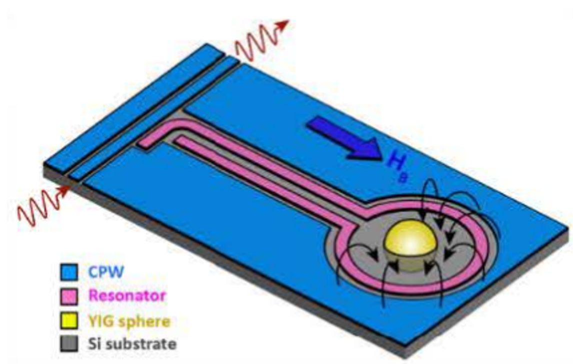

Figure 4.1: Local sphere–resonator module. A single YIG sphere on Si is inductively coupled to a SC loop resonator that can be interfaced to a coplanar transmission line. The diagram highlights the control degrees of freedom used later: (i) the magnon resonance (set by magnetic bias) that tunes the frequency gap to the loop mode, and (ii) the external coupling ports that set loading and readout. This module establishes the baseline geometry, notation, and control handles used throughout the chapter.

4.1.2 Two Spheres Coupled by One Resonator

This modular design can be extended to couple multiple magnonic elements. Figure 4.2 shows a **two-sphere, one-resonator** design. Here, two YIG spheres are coupled to different segments of the *same* SC resonator. The shared current pattern in the loop mediates an effective interaction between the two magnon modes, demonstrating a minimal network. This layout keeps the mediator localized (the loop) while providing a clear path to explore how detuning and placement shape inter-sphere coupling.

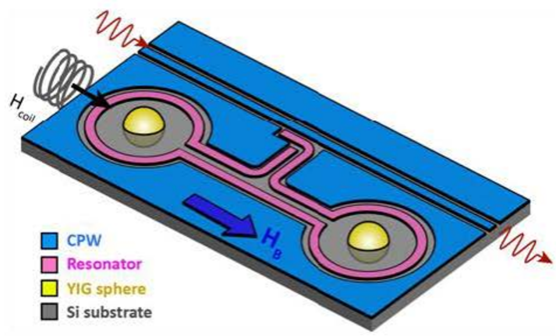

Figure 4.2: Two spheres–one resonator. Two YIG spheres address different segments of a single SC loop; the shared loop current pattern mediates an effective interaction between the magnon modes. Geometric placement and individual loop–sphere coupling rates set the strength and sign of the mediated interaction for a given detuning configuration. This extends the local module to a minimal multi-sphere network while keeping a single SC element as the mediator.

4.1.3 Two Spheres Coupled by a Transmission Line

A more flexible architecture for remote coupling uses a **transmission line** as the mediator, shown in Fig. 4.3. Two YIG spheres, each in their own resonator loop, are coupled to a common CPW. Propagating microwaves in the transmission line carry signals between the two sites. As we will show in Section 4.2, the accumulated propagation phase φ along the line becomes a critical parameter that controls the nature of the remote coupling. A transmission-line layout is especially convenient here because traveling waves supply a phase-referenced path for interaction and an external channel that can add or remove energy.

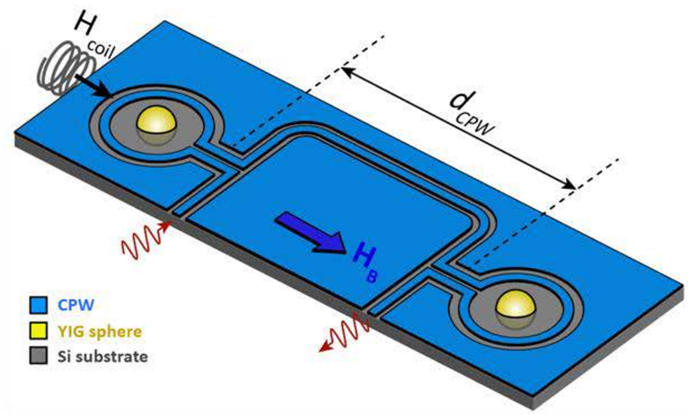

Figure 4.3: Two spheres–one transmission line. Two YIG spheres couple to a common CPW transmission line; traveling waves mediate remote coupling, and the propagation phase between the sites provides a tunable control parameter. The line also furnishes a natural external channel for injection and readout that integrates with the network descriptions used later in the chapter.

4.1.4 Local Dynamic Tuning Coils

Finally, for the dynamic protocols developed in this dissertation, the magnon frequency $\omega_m(t)$ must be tuned in time. Figure 4.4 illustrates how this is achieved experimentally by integrating **local dynamic tuning coils** with the module. A current I_{coil} passed through an on-chip SC coil generates a local magnetic field H_{coil} at one of the YIG spheres, tuning its FMR frequency ω_{m1} without affecting ω_{m2} or the static global bias field H_B. This provides the fast, selective control handle required for all subsequent protocols.

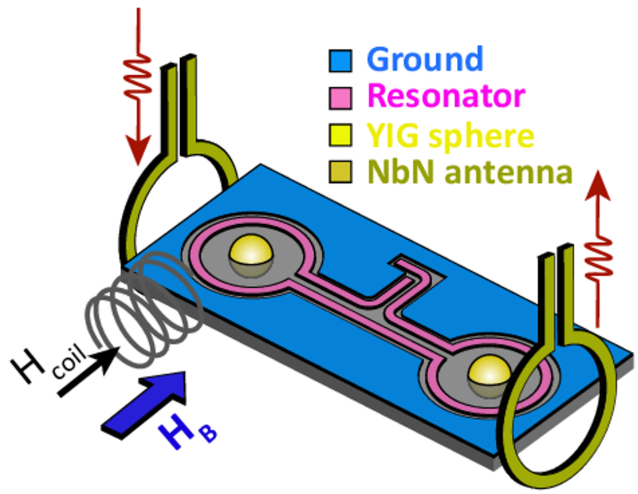

Figure 4.4: The platform module outfitted with local field coils. This enables time-dependent control of a specific magnon resonance $\omega_m(t)$ via I_{coil}, which is the key mechanism for the dynamic protocols in this dissertation.

4.2 Transmission Line-Mediated Coupling Between Two Ferromagnetic Spheres

As a model problem to analyze this platform, we now develop the theory for two remote YIG spheres coupled by a SC transmission line (as in Fig. 4.3). This geometry is particularly rich, as the traveling waves that mediate the coupling can be engineered to be coherent or dissipative. As established in Section 3.4, we use the classical model of coupled amplitudes. We derive a two-port network (TPN) model to describe the system, which yields the collective eigenfrequencies and provides a clear criterion for level repulsion versus level attraction, matching the experimental results from our collaborators.

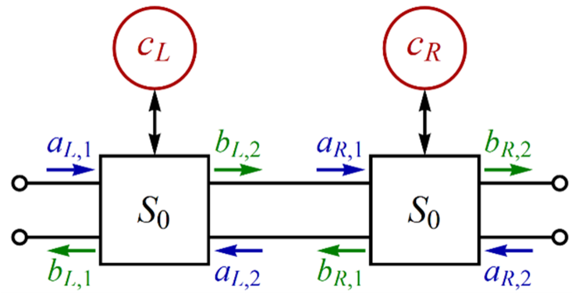

Figure 4.5: Network model of two YIG spheres coupled by a transmission line.

Dynamics of two FM YIG spheres coupled by a microwave transmission line can be analyzed using the network model shown schematically in Fig. 4.5. Namely, we consider each segment of the transmission line coupled to a YIG sphere as a TPN that interacts with the FMR mode of the sphere. The complex amplitude of the FMR mode of a sphere will be denoted as c_α ($\alpha \in \{L, R\}$ denotes the left/right spheres and TPNs); amplitudes of the incoming (outgoing) electromagnetic waves at the α-th TPN will be denoted as $a_{\alpha,j}$ ($b_{\alpha,j}$), where $j = 1$ [$j = 2$] denotes the wave to the left [to the right] of the network, as shown in Fig. 4.5. The normalization of the amplitudes is chosen in the following way: $E_\alpha = |c_\alpha|^2$ is the energy of the magnetic oscillations in the α-th YIG sphere and $P_{\alpha,j} = |a_{\alpha,j}|^2$ and $P'_{\alpha,j} = |b_{\alpha,j}|^2$ are the microwave powers of the corresponding incoming and outgoing waves.

We will assume that both TPNs are identical and are symmetric, reciprocal, and lossless (except for magnetic losses, which will be accounted for in the dynamics of the FMR amplitudes c_α). Then, using the vector notations

$$\boldsymbol{a}_\alpha = \begin{pmatrix} a_{\alpha,1} \\ a_{\alpha,2} \end{pmatrix}, \qquad \boldsymbol{b}_\alpha = \begin{pmatrix} b_{\alpha,1} \\ b_{\alpha,2} \end{pmatrix}, \tag{4.1}$$

one can write the vector equation for outgoing waves at each port:

$$\boldsymbol{b}_\alpha = \boldsymbol{S}_0 \cdot \boldsymbol{a}_\alpha + g_r\, \boldsymbol{e}\, c_\alpha. \tag{4.2}$$

Here $\boldsymbol{S}_0$ is the intrinsic (without account of influence of the magnetic dynamics) scattering matrix, which, without loss of generality, can be written as

$$\boldsymbol{S}_0 = \begin{pmatrix} iR_0 & T_0 \\ T_0 & iR_0 \end{pmatrix}, \tag{4.3}$$

where T_0 and R_0 are real-valued transmission and reflection coefficients, related by

$$T_0^2 + R_0^2 = 1. \tag{4.4}$$

The real parameter g_r in Eq. (4.2) has the dimension of frequency and is equal to the rate of radiation losses of the FM mode into the transmission line. The dimensionless vector $\boldsymbol{e}$ in Eq. (4.2) describes the relative coupling strength of the FMR mode with electromagnetic waves propagating in different directions; for a symmetric network this vector, without loss of generality, can be chosen as

$$\boldsymbol{e} = \begin{pmatrix} 1 \\ 1 \end{pmatrix}. \tag{4.5}$$

The dynamics of the FMR mode c_α, in the frequency domain, is described by the equation

$$\omega c_\alpha = \omega_\alpha c_\alpha - i(\Gamma + g_r) c_\alpha - i g_r\, \boldsymbol{e}^* \cdot \boldsymbol{a}_\alpha. \tag{4.6}$$

Here ω is the driving frequency, ω_α is the FMR frequency of the α-th sphere, and Γ is the intrinsic magnetic damping rate (not related to the radiation losses g_r). The relations between coefficients of Eqs. (4.2) and (4.6) are determined by the energy conservation considerations at the α-th TPN, as described below. The solution of Eq. (4.6) for a given $\boldsymbol{a}_\alpha$ is given by

$$c_\alpha = -i g_r \frac{\boldsymbol{e}^* \cdot \boldsymbol{a}_\alpha}{(\omega - \omega_\alpha) + i(\Gamma + g_r)}. \tag{4.7}$$

Using it in Eq. (4.2), one can easily find the scattering matrix $\boldsymbol{S}_\alpha$ of the TPN loaded with the YIG sphere:

$$\boldsymbol{b}_\alpha = \boldsymbol{S}_\alpha \cdot \boldsymbol{a}_\alpha, \qquad \boldsymbol{S}_\alpha = \boldsymbol{S}_0 \cdot \left[\boldsymbol{I} - i \frac{g_r}{(\omega - \omega_\alpha) + i(\Gamma + g_r)} \boldsymbol{e} \otimes \boldsymbol{e}^* \right]. \tag{4.8}$$

Here $\boldsymbol{I}$ is the identity matrix and $\otimes$ denotes the direct (outer) product of vectors. Using Eq. (4.8), one can easily find the power drop at the TPN:

$$\Delta P_\alpha = |\boldsymbol{a}_\alpha|^2 - |\boldsymbol{b}_\alpha|^2 = \frac{2 g_r \Gamma}{(\omega - \omega_\alpha)^2 + (\Gamma + g_r)^2} |\boldsymbol{e}^* \cdot \boldsymbol{a}_\alpha|^2. \tag{4.9}$$

Note that $\Delta P_\alpha = 0$ when $\Gamma = 0$, i.e., only intrinsic magnetic damping Γ leads to power losses, while the radiation damping g_r does not contribute to the overall energy loss if the electromagnetic waves are taken into account. For $\Gamma \neq 0$, the power drop ΔP_α can be written as $\Delta P_\alpha = 2\Gamma E_\alpha$, which, again, clearly shows that the power drop at the network is associated with the intrinsic magnetic losses. These energy considerations fix the relations between coefficients in Eq. (4.2) and Eq. (4.6).

To analyze the problem of interaction of two YIG spheres, we need to complement Eqs. (4.2) and (4.6) with equations relating amplitudes of waves propagating between the spheres, which can be written as

$$a_{L,1} = e^{i\varphi} b_{R,2}, \tag{4.10a}$$

$$a_{R,2} = e^{i\varphi} b_{L,1}. \tag{4.10b}$$

Here φ is the total phase shift acquired by an electromagnetic wave during propagation between the two TPNs. It depends on the frequency of the electromagnetic wave ω and the distance d_{CPW} between the networks and can be found as $\varphi = (\omega / c_{\text{eff}}) d_{CPW}$, where c_{eff} is the speed of the electromagnetic waves in the transmission line. In Eqs. (4.10a) and (4.10b), we assumed that the transmission line is reciprocal (phases acquired by waves propagating in opposite directions are equal). By using a complex phase φ with $\text{Im}(\varphi) > 0$

in Eqs. (4.10a) and (4.10b), one can also investigate the influence of losses in the transmission line.

Equations (4.2), (4.6), and (4.10a)–(4.10b) form a closed system of equations that allows one to find all characteristics of the circuit given the amplitudes of the incoming waves $a_{R,1}$ and $a_{L,2}$. One may use Eq. (4.8) for the loaded scattering matrix $\boldsymbol{S}_\alpha$ of a single TPN to find the scattering matrix of the overall system using standard methods of microwave network theory.

From the physical point of view, however, it would be more useful to derive effective equations for the amplitudes of the FMR oscillations c_α, which would clearly demonstrate non-Hermitian interaction between them caused by coupling with the transmission line. To do this, we use Eqs. (4.2), (4.6), and (4.10a)–(4.10b) one can find relations between input $\hat{\boldsymbol{a}} \equiv (a_{L,1}, a_{R,2})$ and output $\hat{\boldsymbol{b}} \equiv (b_{L,1}, b_{R,2})$ circuit amplitudes and amplitudes of FMR oscillations $\hat{\boldsymbol{c}} \equiv (c_L, c_R)$. This calculation is straightforward, although cumbersome:

$$\hat{\boldsymbol{b}} = \hat{\boldsymbol{S}}_0 \cdot \left[\hat{\boldsymbol{a}} + \sqrt{g_r}\,\hat{\boldsymbol{G}} \cdot \hat{\boldsymbol{c}}\right], \tag{4.11a}$$

$$\omega\,\hat{\boldsymbol{c}} = \left(\hat{\boldsymbol{H}}_0 - i\,\Gamma\,\hat{\boldsymbol{I}} + g_r\,\hat{\boldsymbol{K}}\right) \cdot \hat{\boldsymbol{c}} - i\sqrt{g_r}\,\hat{\boldsymbol{G}}^+ \cdot \hat{\boldsymbol{a}}. \tag{4.11b}$$

Here $\hat{\boldsymbol{I}}$ is the identity matrix,

$$\hat{\boldsymbol{S}}_0 = \begin{pmatrix} i\hat{R}_0 & \hat{T}_0 \\ \hat{T}_0 & i\hat{R}_0 \end{pmatrix}, \tag{4.12a}$$

$$\hat{\boldsymbol{G}} = \begin{pmatrix} G_d & G_x \\ G_x & G_d \end{pmatrix}, \tag{4.12b}$$

$$\hat{\boldsymbol{H}}_0 = \begin{pmatrix} \omega_L & 0 \\ 0 & \omega_R \end{pmatrix}, \tag{4.12c}$$

$$\hat{\boldsymbol{K}} = \begin{pmatrix} K_d & K_x \\ K_x & K_d \end{pmatrix}, \tag{4.12d}$$

where

$$\hat{R}_0 = \frac{1 + e^{2i\varphi}}{1 + e^{2i\varphi} R_0^2} R_0, \tag{4.13a}$$

$$\hat{T}_0 = \frac{e^{i\varphi}}{1 + e^{2i\varphi} R_0^2} T_0^2, \tag{4.13b}$$

$$G_d = 1 - \frac{i}{e^{2i\varphi} + R_0^2} T_0 R_0, \tag{4.13c}$$

$$G_x = \frac{e^{i\varphi}}{e^{2i\varphi} + R_0^2} T_0, \tag{4.13d}$$

$$K_d = -i + \frac{e^{2i\varphi}(T_0 + iR_0)R_0}{1 + e^{2i\varphi} R_0^2}, \tag{4.13e}$$

$$K_x = -i \, \frac{e^{i\varphi}(T_0 + iR_0)}{1 + e^{2i\varphi} R_0^2}. \tag{4.13f}$$

Note that

$$\hat{\boldsymbol{G}}^{+} \cdot \hat{\boldsymbol{G}} = i \left(\hat{\boldsymbol{K}} - \hat{\boldsymbol{K}}^{+} \right). \tag{4.14}$$

This condition ensures that the energy of the system is conserved in the case $\Gamma = 0$ and, for $\Gamma \neq 0$, the energy drop at the whole circuit is related to the intrinsic losses in the YIG spheres:

$$\Delta P = \hat{\boldsymbol{a}}^{+} \cdot \hat{\boldsymbol{a}} - \hat{\boldsymbol{b}}^{+} \cdot \hat{\boldsymbol{b}} = 2\Gamma \, \hat{\boldsymbol{c}}^{+} \cdot \hat{\boldsymbol{c}}. \tag{4.15}$$

The matrix $\hat{\boldsymbol{K}}$ in Eq. (4.11b) describes the effects of the transmission line on the collective oscillations of two YIG spheres. The diagonal elements of this matrix, K_d, describe the shift of individual FMR frequencies and direct radiation losses in each YIG sphere. The most interesting effect—effective coupling between the spheres—is described by the off-diagonal elements of $\hat{\boldsymbol{K}}$ (K_x, see Eq. (4.13f)). The real part of K_x describes Hermitian (conservative) coupling, while the imaginary part of K_x is responsible for anti-Hermitian (dissipative) coupling. As one can see from Eq. (4.13f), the phase of the coupling term K_x depends on the phase shift φ between the TPNs and can be tuned by changing the operational frequency of the circuit (i.e., changing the bias magnetic field).

As one can see from Eq. (4.13f), one can achieve a strong dissipative coupling between YIG spheres by using TPNs with strong intrinsic reflection ($R_0 \approx 1$, $T_0 \ll 1$) with quarter wavelength separation between them ($\varphi = \pi/2$). In this case, the coupling K_x is imaginary and large,

$$K_x \approx \frac{i}{T_0^2}. \tag{4.16}$$

This situation corresponds to a perfectly matched (in absence of YIG spheres) composite TPN which perfectly transmits electromagnetic waves due to destructive interference of waves reflected at the left and right individual TPNs. Introduction of YIG spheres strongly disrupts fine balance between partial reflected waves, which explains enhanced influence of YIG spheres on traveling electromagnetic waves and enhanced mutual coupling between the spheres.

In the opposite case of weak reflection at an individual TPN ($R_0 \approx 0$, $T_0 \approx 1$), the coefficients of the coupling matrix $\hat{\boldsymbol{K}}$ take a simple form

$$K_d \approx -i, \qquad K_x \approx -ie^{i\varphi}. \tag{4.17}$$

Here, dissipative coupling is achieved when $\varphi = n\pi$ (n is an integer), i.e., when the distance between two YIG spheres is a multiple of half-wavelength of the electromagnetic wave.

In what follows, we analyze the frequencies of collective eigen-oscillations of two YIG spheres in the limit of weak reflection ($R_0 = 0$, $T_0 = 1$). For simplicity, we also neglect intrinsic magnetic damping ($\Gamma = 0$) as compared to the radiation losses g_r. These approximations are satisfied with good accuracy for the experimental conditions.

The equations for collective oscillations of YIG spheres are obtained from Eq. (4.11b) in the absence of incoming waves ($\hat{\boldsymbol{a}} = 0$). Using the simplified expressions from Eq. (4.17), these equations become

$$\Omega c_L = \omega_L c_L - i g_r c_L - i e^{i\varphi} g_r c_R, \tag{4.18a}$$

$$\Omega c_R = \omega_R c_R - i g_r c_R - i g_r e^{i\varphi} c_L. \tag{4.18b}$$

In Eqs. (4.18), Ω is the complex eigenfrequency of the collective oscillations of the spheres. The two possible solutions for Ω are

$$\Omega_\pm = \omega_0 - i g_r \pm \sqrt{\delta\omega^2 - g_r^2 e^{2i\varphi}}. \tag{4.19}$$

Here $\omega_0 = (\omega_L + \omega_R)/2$ is the average FMR frequency of the two spheres, and $\delta\omega = (\omega_L - \omega_R)/2$ is half separation of the FMR frequencies. Separating the real and imaginary parts of Eq. (4.19), $\Omega_\pm = \omega_\pm - i g_\pm$, gives

$$\omega_\pm = \omega_0 \pm \Delta\omega, \qquad g_\pm = g_r \left[1 \pm \frac{g_r}{2\Delta\omega} \sin(2\varphi)\right], \tag{4.20}$$

where $\Delta\omega$ is the half-separation between the frequencies of the collective oscillations:

$$\Delta\omega = \frac{1}{\sqrt{2}} \sqrt{\delta\omega^2 - g_r^2 \cos(2\varphi) + \sqrt{\delta\omega^4 - 2\delta\omega^2 g_r^2 \cos(2\varphi) + g_r^4}}. \tag{4.21}$$

Equations (4.20) and (4.21) are the central result of this analysis. These equations allow one to easily find the frequencies and radiation-induced losses of collective oscillations of two YIG spheres connected by a transmission line for arbitrary phase shift φ. Figure 4.6 shows the dependence of the collective frequencies $\omega_\pm$ on the frequency detuning $(\omega_L - \omega_R)$ for several phase shifts φ (indicated on the graphs). Shaded areas in these graphs show the regions of one radiation linewidth from the collective frequency, $\omega_\pm - g_\pm < \omega < \omega_\pm + g_\pm$.

For $\varphi/\pi = 0.50$ (purely Hermitian, or conservative, coupling between the spheres) one can see the usual picture of mode repulsion (anti-crossing) with a resonant (at $\delta\omega = 0$) gap between the modes $2\Delta\omega_0 = 2g_r$. The radiative losses for each mode are identical,

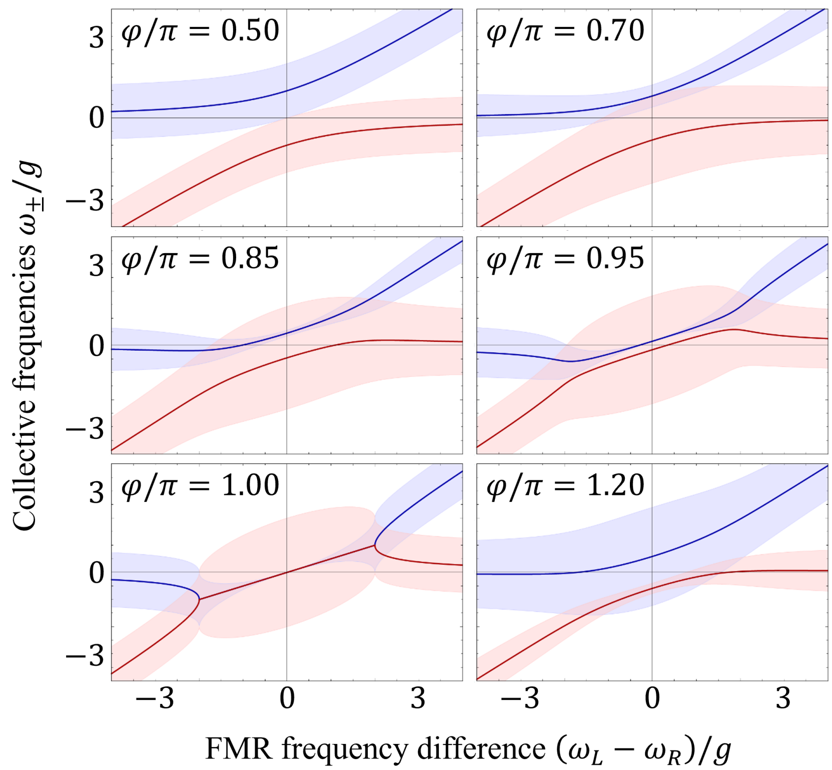

Figure 4.6: Dependence of collective frequencies of YIG spheres on the separation of FMR frequencies $(\omega_L - \omega_R)$ for several phase shifts φ introduced by the transmission line. Solid lines show real parts of the eigenfrequencies $\omega_\pm$; light shaded areas show the regions corresponding to the radiation linewidth of collective modes, $\omega_\pm - g_\pm < \omega < \omega_\pm + g_\pm$.

$g_\pm = g_r$, and are unaffected by the mutual coupling between the spheres. Note that the gap between modes is twice the radiation losses of each mode. One can expect such a relation between $2\Delta\omega_0$ and $g_\pm$, because both effects are caused by the same physical interaction—coupling of a YIG sphere to propagating electromagnetic waves.

With an increase of the phase shift φ, the frequencies of the two collective modes move closer to each other in the interaction region $\delta\omega \approx 0$. This effect is especially well pronounced in the graph for $\varphi/\pi = 0.95$, where the two collective frequencies move parallel to each other and remain at a very close distance over a wide interval of detunings

$\delta\omega$. Note that in this region the radiation losses of one mode (ω_-) increase, while the losses of the other mode (ω_+) decrease. Due to the small frequency separation between the modes, the resonance linewidths of the modes overlap, making experimental distinction between the two modes a difficult task.

When the inter-mode coupling is purely dissipative ($\varphi = \pi$), the frequencies of both modes exactly coincide, $\omega_\pm = \omega_0$, within the detuning interval $|\delta\omega| < g_r$. The radiation losses in this case are

$$g_\pm = g_r \pm \sqrt{g_r^2 - \delta\omega^2}. \tag{4.22}$$

Note that the radiation losses of one mode completely vanish at the exact resonance point $\delta\omega = 0$.

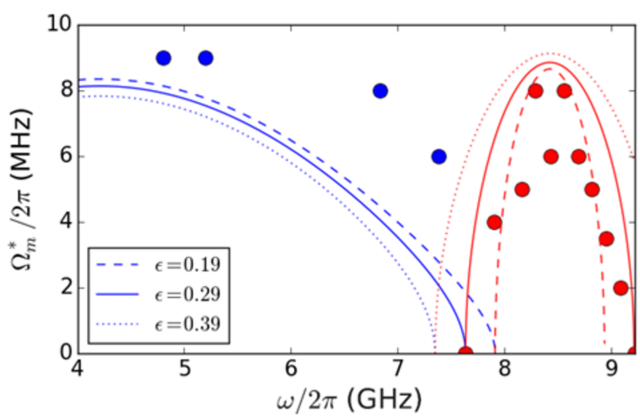

Figure 4.7: Apparent couplings in the level attraction Ω_{att} (red) and level repulsion Ω_{rep} (blue) regimes as a function of frequency f of electromagnetic waves (proportional to the phase shift $\varphi = \pi f/f_0$). Circular points represent experimental data, and curves show calculations using Eqs. (4.24) and (4.25). Parameters used in the calculation of the solid curve: $f_0 = 8.425$ GHz, $g_r/2\pi = 8.5$ MHz, $\epsilon = 0.29$. Comparison predictions with $\epsilon = 0.19$ and $\epsilon = 0.39$ are plotted as dashed and dotted curves, respectively.

With further increase of the phase shift φ, the frequencies of the two collective modes start to separate again, and the whole process repeats cyclically with period $\Delta\varphi = \pi$. Note, however, that for $\varphi > \pi$ the reduction of the radiation losses is seen for the lower-frequency mode ω_-. When the frequency difference $2\Delta\omega = \omega_+ - \omega_-$ becomes significantly smaller than the sum of the modes' linewidths $2g_r = g_+ + g_-$, it is not possible to distinguish the two modes experimentally anymore. As a simple criterion of mode distinguishability, we assume that the modes become indistinguishable when $\Delta\omega < \epsilon g_r$, where ϵ is a certain dimensionless parameter. In the "distinguishable" case $\Delta\omega > \epsilon g_r$, the finite modes' linewidth leads to a reduction of the apparent separation $\Delta\omega_{\text{app}}$ between the modes; to account for this effect, we adopt a simple model $\Delta\omega_{\text{app}}^2 = \Delta\omega^2 - (\epsilon g_r)^2$. Within these assumptions, a region of apparent mode attraction exists when

$$|\sin(\varphi)| < 2\epsilon, \tag{4.23}$$

and, within this region, the frequency half-interval of apparent mode attraction is given by

$$\Omega_{\text{att}} = g_r \frac{\sqrt{(\cos(2\varphi) + 2\epsilon^2)^2 - 1}}{2\epsilon}. \tag{4.24}$$

In the "repulsive" region $|\sin(\varphi)| > 2\epsilon$, the minimum half-gap between the modes (apparent coupling constant) is equal to

$$\Omega_{\text{rep}} = g_r \sqrt{\sin^2(\varphi) - \epsilon^2}. \tag{4.25}$$

Figure 4.7 shows the comparison of Eqs. (4.24) and (4.25) with the experimental data. One can see reasonably good agreement between the theory and experiment, given the simple model used in the calculations. Changing the value of ϵ mainly shifts the transition frequency between level attraction and repulsion, where $\epsilon = 0.29$ best captures the transition frequency.

4.3 Conclusion

This chapter has introduced the modular, SC-circuit-based platform developed by our collaborators. We then presented our theoretical TPN model for analyzing the static coupling between two remote magnonic resonators mediated by a transmission line.

The key result of this analysis is the validation of our classical model, which, as shown in Fig. 4.7, accurately reproduces the experimental results. This includes the full, phase-dependent crossover from coherent, Hermitian coupling (seen as level repulsion) to dissipative, non-Hermitian coupling (seen as level attraction). This agreement gives us high confidence in the underlying model of coupled oscillators.

With this static, classical model validated, we now have the foundation to explore the core topic of this dissertation. Chapter 5 will build directly on this framework by introducing time-dependent control, moving from the static analysis of what the coupling is in a specific system to the more general and geometry-agnostic idea of the dynamic control of when and how that coupling is applied.

CHAPTER FIVE

BASIC DYNAMIC MAGNON TUNING PROTOCOLS

Chapter 4 analyzed a candidate experimental platform in a *static* regime. This chapter transitions to the core topic of this dissertation: the *dynamic* control of magnon-mediated interactions. We introduce three basic protocols—a linear ramp, a parabolic ramp, and a rectangular pulse—that use time-dependent magnetic fields to tune a magnon's resonance.

The analysis in this chapter is performed using the classical model of coupled harmonic oscillators, first introduced in Section 3.4. This approach is intentional. As established in Section 3.4, the dynamics of the classical model are formally equivalent to the single-excitation ($N = 1$) quantum regime in the absence of damping. By using the simpler, more intuitive classical model, we can build a clear understanding of how temporal pulse shaping (linear, parabolic, etc.) directly creates different functionalities (transfer, SWAP, etc.). These classical results provide the fundamental intuition for the fully quantum, multi-excitation protocols that will be developed in Chapters 6, 7, and 8.

5.1 Linear ramp

To better understand this new dynamic approach, let us first consider the case of a statically tuned resonant magnon frequency. It is well understood that hybrid magnonic systems benefit from the wide-ranged tunability of the resonant magnon frequency using changes in bias magnetic field strength. Existing systems that achieve high coupling rates encompass a wide variety of geometries ranging from millimeter-scale microwave cavities [31], [32], [33] to micrometer-scale SC CPW resonators [30], [34], [35]. These systems function via resonant coupling between the electromagnetic and magnonic resonators. This resonant coupling occurs when the resonant magnon frequency is near the resonant frequency of the photonic resonator. Changing the strength of the bias magnetic field and, thus, the magnon resonant frequency allows one to continuously tune the hybrid system on and off the resonance and observe the famous anti-crossing behavior of the coupled oscillator's frequencies, shown schematically in Fig. 5.1.

The behavior of a hybrid magnon-photon system can be mathematically described by the classical model of coupled amplitudes (from Eq. (3.24)) for complex amplitudes of the photonic $a_1(t)$ and magnonic $a_\mathrm{m}(t)$ resonator modes [40], [44], [45]:

$$\begin{aligned} \frac{da_1}{dt} + i\omega_1 a_1 &= -ig_1 a_\mathrm{m}, \\ \frac{da_m}{dt} + i\omega_\mathrm{m}(B)\, a_\mathrm{m} + \Gamma_\mathrm{m} a_\mathrm{m} &= -ig_1^* a_1. \end{aligned} \tag{5.1}$$

Here ω_1 and ω_m are the resonant frequencies of the photonic and magnonic modes, respectively; the magnonic frequency ω_m depends on the applied bias magnetic field B and can be easily tuned in a wide range. Γ_m is the damping rate of the magnonic resonator; the corresponding term was, for simplicity, neglected in the equation for photonic mode a_1 since the photon damping rate Γ_p is usually much lower than Γ_m. The parameter g_1 in Eqs. (5.1) is the coupling rate between the magnon and photon modes and can exceed 100 MHz [30], [31], [32], [33], [34], [35].

As established in Section 3.4, these classical equations (neglecting Γ_m) are formally identical to the quantum model in the $N = 1$ subspace. The classical populations $|a_1(t)|^2$ and $|a_m(t)|^2$ are directly analogous to the quantum probabilities of finding the single excitation in the photonic or magnonic mode, respectively. This equivalence justifies using this intuitive classical model to design these protocols.

Model Eqs. (5.1) describe linear coupling of two resonant modes. One can easily find eigen-frequencies of two coupled oscillations formed as a result of mode interaction:

$$\omega_\pm = \frac{\omega_1 + \omega_\mathrm{m}}{2} \pm \sqrt{\left(\frac{\omega_1 - \omega_\mathrm{m}}{2}\right)^2 + {g_1}^2}. \tag{5.2}$$

The solutions for Eq. (5.2) for varying ω_m (which, physically, corresponds to varying bias magnetic field) are shown in Fig. 5.1 and demonstrates the formation of a mode anti-crossing at the point of the strongest resonant coupling ($\omega_1 = \omega_m$), where the modes become strongly hybridized to prevent degeneracy of their frequencies. The gap between the coupled mode frequencies at the anti-crossing point is proportional to the coupling strength, $\omega_+ - \omega_- = 2|g_1|$.

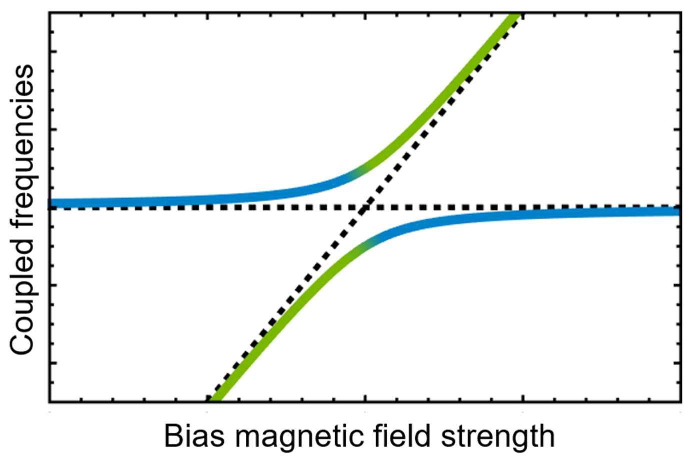

Figure 5.1: Dependence of the coupled-mode frequencies $\omega_\pm$ from Eq. (5.2) on the bias magnetic field (i.e., magnonic mode frequency ω_m). Dashed lines indicate the uncoupled photonic ω_1 and magnonic ω_m frequencies. Color encodes modal content: magnonic (green) and photonic (blue).

Typically, existing studies of hybrid magnon-photonic systems focus on quasi-static tuning of the magnon resonance frequency ω_m, in which the characteristic time τ of magnetic field variation is much longer than the magnon lifetime, $\tau \gg 1/\Gamma_m$. In this case the hybrid system behaves as a usual resonance system with statically tunable resonance parameters described by Eq. (5.2).

The strongly coupled ($|g_1| \gg \Gamma_{\rm m}$) magnon-photon systems, however, may exhibit much richer and much more interesting behavior in case of dynamic tuning of the resonance frequency $\omega_{\rm m}$. If the characteristic time of the magnetic field variation τ satisfies $1/\Gamma_{\rm m} \gg \tau \gtrsim 1/|g_1|$, the parameters of the magnon mode change during lifetime of a single magnon; at the same time, magnon and photon modes interact over a sufficiently long time interval ($\tau|g_1| \gtrsim 1$) to ensure efficient energy and information exchange between the modes.

In the simplest case of a linearly ramped bias magnetic field $B(t) = B_0 + (dB/dt)t$ the behavior of the dynamically-tuned hybrid system can be qualitatively understood from Fig. 5.1, in which the horizontal axis now plays the role of time. As the bias field $B(t)$ comes closer to the resonance value, the two modes hybridize, but the excitation initially localized within the higher (lower) mode, will continue to stay in that mode. The overall result of the "passage" shown in Fig. 5.1 is the transfer of energy and information from the photonic mode to the magnonic one [along the upper branch $\omega_+(t)$], and vice versa [along the lower branch $\omega_-(t)$]. Note, however, that this simple picture of an *adiabatic passage* is, strictly speaking, quantitatively correct for relatively slow ramps $\tau \gg |g_1|$; in a more realistic non-adiabatic setting $\tau \sim 1/|g_1|$ a more elaborate model of hybrid system dynamics, which is described below, must be utilized.

By shaping the profile of the pulsed magnetic field one can control how strongly, when, and for how long the resonant coupling occurs, which, in turn, will determine the overall outcome of the "passage".

Below, we illustrate some of the capabilities of dynamically-tuned hybrid magnon-photon systems using, as an example, a system that consists of two photonic resonators (amplitudes a_1 and a_2, resonant frequencies ω_1 and ω_2) and one magnonic resonator (amplitude $a_{\rm m}$, frequency $\omega_{\rm m}$, damping rate $\Gamma_{\rm m}$). The photonic resonators are not coupled directly, but both interact with the magnonic resonator with coupling rates g_1

and g_2, respectively. The equations describing this system is a direct generalization of Eqs. (5.1):

$$\begin{aligned} \frac{da_1}{dt} + i\omega_1 a_1 &= -ig_1 a_\mathrm{m}, \\ \frac{da_m}{dt} + i\omega_\mathrm{m}(t)a_\mathrm{m} - \Gamma_\mathrm{m} a_\mathrm{m} &= -ig_1^* a_1 - ig_2^* a_2, \\ \frac{da_2}{dt} + i\omega_2 a_2 &= -ig_2 a_\mathrm{m}. \end{aligned} \tag{5.3}$$

In the following simulations we used conservative estimate for the coupling rates, $g_{1,2} = g_\mathrm{c} = 2\pi \cdot 20$ MHz, which is much lower than the experimentally achievable values. We assumed the damping value $\Gamma_\mathrm{m} = 6.28\ \mu\mathrm{s}^{-1}$ typical for magnonic resonators made of YIG, as listed in Table 2.1.

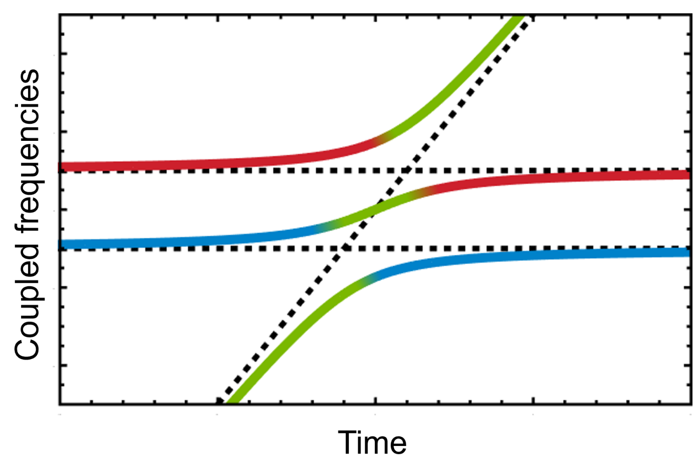

Figure 5.2: Qualitative three-mode spectrum under a linear ramp of $\omega_m(t)$. Dashed lines show uncoupled SC-resonator eigenfrequencies ω_1, ω_2 and the magnon frequency ω_m. Colored branches indicate instantaneous hybrid modes and their energy distribution among magnonic (green) and SC-resonator modes S_1 (blue) and S_2 (red), highlighting two avoided crossings and the $S_1 \to M \to S_2$ relay.

To set intuition for the linear ramp in the three-mode setting, a qualitative diagram of the instantaneous eigen-frequencies is shown in Fig. 5.2. As $\omega_m(t)$ sweeps across ω_1 and ω_2, two hybridization regions appear and the color of the branches indicates the distribution of energy among the magnonic and SC-resonator modes, which aligns with the relay picture of $S_1 \to M \to S_2$ used below.

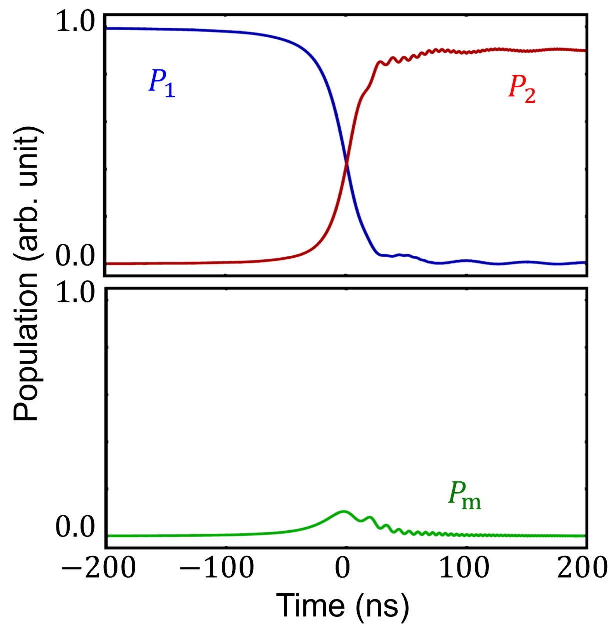

Figure 5.3: Temporal evolution during a linear passage. Top panel: populations $P_{1,2} = |a_{1,2}|^2$ of SC resonators S_1 and S_2. Bottom panel: magnon population $P_m = |a_m|^2$. The magnon frequency is swept with rate $\rho/2\pi = 2.5$ MHz/ns. The passage implements the $S_1 \to M \to S_2$ relay while keeping P_m modest, consistent with mediated transfer.

To illustrate the proposed approach, we performed simulations of magnon-mediated transfer of energy between two SC resonators S_1 and S_2, which are not mutually coupled and have different frequencies ω_1 and ω_2 ($\omega_2 - \omega_1 = 2\pi \times 20$ MHz in the simulations shown below). S_1 and S_2 are coupled to the same magnetic element (M), FMR frequency of which $\omega_m(t)$ is swept from below ω_1 to above ω_2 with the linear ramp rate $\rho = d\omega_m/dt$. On a qualitative level, when $\omega_m(t)$ crosses the frequency ω_1, S_1 and M become effectively coupled, and the energy from S_1 goes to M. Then, when $\omega_m(t)$ crosses ω_2, this energy is transferred to the S_2 resonator. The net result of such "passage" is the transfer of energy or information from S_1 to S_2, with magnons playing the role of a mediator. In this process the energy exists in the form of magnons only for a short time and, respectively, finite magnon lifetime (which is typically much shorter than damping time in SC elements) is not critical for the transfer efficiency.

Figure 5.3 displays the corresponding populations during a representative passage; the temporal structure confirms the intuition developed above and quantifies the relay through M.

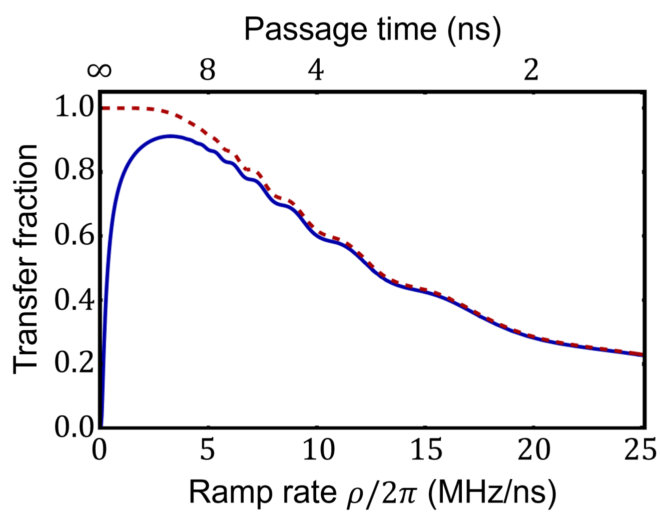

Figure 5.4: Transfer fraction $S_1 \rightarrow S_2$ versus ramp rate ρ. Solid line: dissipative case; dashed line: ideal non-dissipative case ($\Gamma_m = 0$). A broad maximum near $\rho \sim g_c^2$ yields $\sim$90% transfer. Faster ramps limit interaction time; slower ramps increase dissipation losses in the magnetic subsystem.

Figure 5.4 summarizes how the transfer efficiency depends on the ramp rate for the same system parameters. If the ramp is too fast, the modes do not have sufficient time to interact and the transfer fails. If the ramp is too slow (approaching the quasi-static limit), the excitation spends too much time in the lossy magnon mode, and the transfer efficiency drops due to dissipation. An optimal transfer of ~90% is achieved at an intermediate rate ($\rho \sim g_c^2$) that balances interaction time against dissipation.

Thus, our numerical simulations showed the feasibility of efficient and fast magnon-mediated transfer of energy in hybrid magnon–photon systems. We hope that the proposed approach of dynamically-coupled hybrid systems will also be useful for a number of different information-processing operations in quantum computing systems.

5.2 Parabolic Ramp

The dynamics of the hybrid magnon-photon system is determined by the profile of the pulsed bias magnetic field, i.e., by the time dependence of the magnonic resonance frequency $\omega_\mathrm{m}(t)$. Here we consider a parabolically shaped profile,

$$\omega_\mathrm{m}(t) - \omega_1 = -\lambda t^2 + \Delta, \tag{5.4}$$

where the parameters Δ and λ determine the maximum value and the curvature λ of the pulse as shown in Fig. 5.5. The characteristic passage time in this case is $\tau \sim \sqrt{g_\mathrm{c}/\lambda}$.

In the adiabatic limit $\tau \gg |g_\mathrm{c}|$ the parabolic "passage" has no effect on the final populations of the interacting modes, as the magnonic frequency $\omega_\mathrm{m}(t)$ crosses each of the photonic modes twice. The situation, however, is different in the non-adiabatic regime $\tau \sim 1/g_\mathrm{c}$, in which the final populations of each mode depend on the pulse parameters λ and Δ. This means that by simply changing the shape of the pulsed magnetic field profile, different operations can be realized in the same physical system.

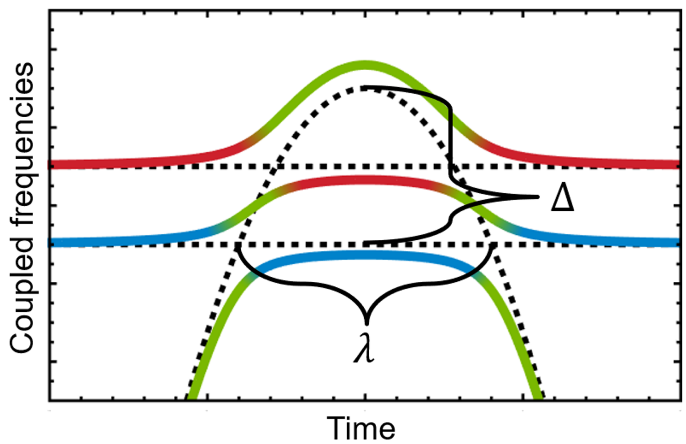

Figure 5.5: Instantaneous eigenfrequencies of Eq. (5.3) under the parabolic profile Eq. (5.4). Parameter Δ sets the maximum of $\omega_{\mathrm{m}}(t)$; λ controls the curvature. Color denotes energy distribution between the interacting resonators.

One such operation useful in quantum computing is the coherent exchange of information between the two photonic modes (SWAP operation). Figure 5.6 reports a representative simulation and highlights the magnon content that accompanies the swap.

It is also important to note, that the population of the magnon mode is zero after the passage, i.e., the magnonic serves only as a mediator of energy transfer between the photonic subsystems. Since the passage occurs during a relatively short time $\tau \ll 1/\Gamma_{\mathrm{m}}$, the magnon dissipation does not play a crucial role in this process, and the accuracy of the SWAP operation is close to 100%.

Another useful operation in quantum computing is the SPLIT operation, where one coherent information state is split into a coherent superposition of multiple information states. Such SPLIT operation can be performed using the same parabolic-shaped pulsed magnetic field profile Eq. (5.4) with different values of the curvature λ and maximum frequency Δ. Simulation of this operation in Fig. 5.7 used
$\lambda = 1.625\, g_{\mathrm{c}}^3 = 2\pi \cdot 0.513$ MHz/ns^2, $\Delta = -0.985\, g_{\mathrm{c}} = -2\pi \cdot 19.7$ MHz, and

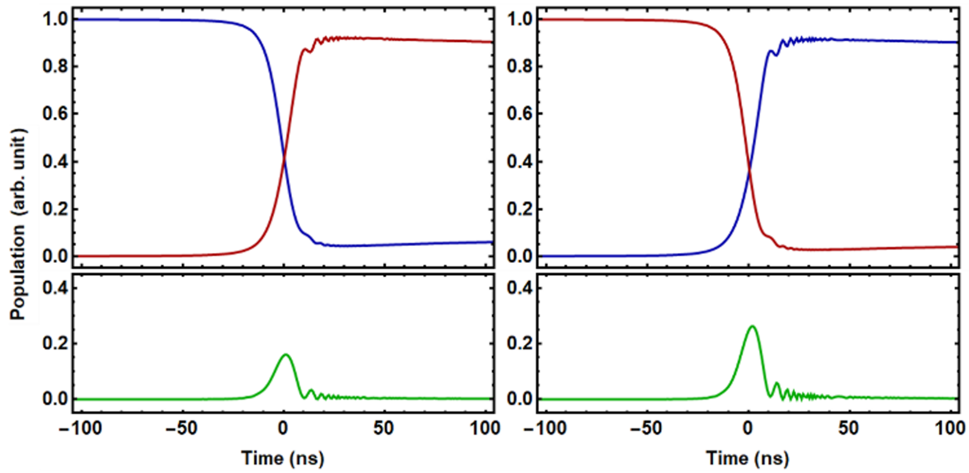

Figure 5.6: Parabolic-ramp SWAP operation with $\lambda = 2.0\, g_c^3 = 2\pi \cdot 0.63$ MHz/ns^2, $\Delta = -1.0\, g_c = -2\pi \cdot 20.0$ MHz, and $\Delta\omega_{2,1} = 2\pi \cdot 2.0$ MHz. Left: information initially in a_1 (blue) is coherently transduced to a_2 (red). Right: inverse process. Bottom panels: transient magnon population a_m, showing an asymmetry arising from the nonzero $\Delta\omega_{1,2}$.

$\Delta\omega_{1,2} = \omega_2 - \omega_1 = 2\pi \cdot 12.0$ MHz shows an asymmetry similar to that seen in the SWAP operation especially pronounced in the time dependence of the magnonic mode.

Interestingly, despite this observable asymmetry, the SPLIT operation may also be used to reverse the generation of entanglement by simply repeating the same operation on the coherent superposition of information states, shown in Fig. 5.8. This SPLIT operation and its reversal can also be performed on degenerate photonic modes.

Dynamic tuning of resonant magnon frequencies may also be useful for investigation of fundamental properties of single magnons. For example, one can consider a system of a single photonic resonator coupled to a magnonic resonator as described in the mathematical model Eqs. (5.1) with a parabolic profile $\omega_m(t)$ from Eq. (5.4). The dependence of the instantaneous eigen-frequencies of hybrid modes for this case is shown in Fig. 5.9. If the magnetic field profile is non-adiabatic, $\tau \sim |g_c|$, then only a partial (say, 50%) exchange of quantum state will occur at each of the two points of resonant

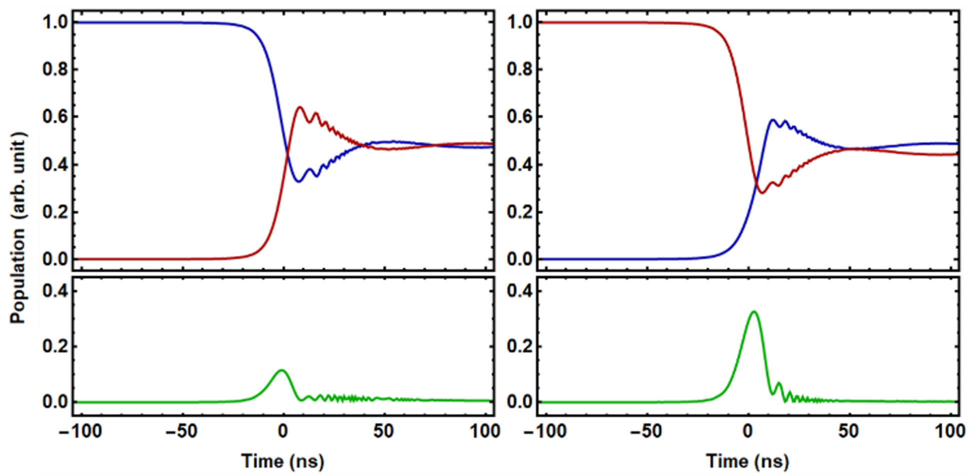

Figure 5.7: Parabolic-ramp SPLIT operation with $\lambda = 1.625\, g_c^3 = 2\pi \cdot 0.513$ MHz/ns^2, $\Delta = -0.985\, g_c = -2\pi \cdot 19.7$ MHz, and $\Delta\omega_{1,2} = 2\pi \cdot 12$ MHz. Left: information initially in a_1 (blue) is split into a coherent superposition across a_1 (red) and a_2. Right: the symmetric case with roles of a_1 and a_2 interchanged. Bottom: transient a_m population.

hybridization. Then, in the time interval between the hybridization points the system will exist in an entangled magnon/photon state. The two components of this state will interfere at the second hybridization point, and the final population of each mode will depend on details of single-magnon dynamics. Experiments of this type will be useful to investigate single-magnon non-dissipative decoherence processes, which are difficult to study using other means. This concept is explored fully in Chapter 7.

Finally, we note, that similar magnon-mediated coherent operations, described here for the case of photonic modes, are also possible with phonons and other solid-state excitations that efficiently couple to magnons. Thus, magnons represent a promising candidate for a universal mediator of coherent quantum information transduction in heterogeneous quantum systems.

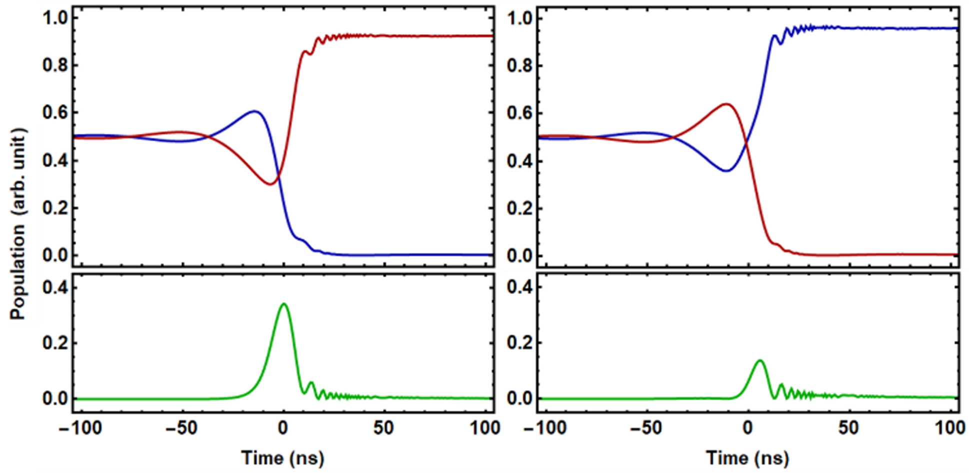

Figure 5.8: Reversibility of the SPLIT operation using the same pulse parameters as in Fig. 5.7. Initial states here match the final states from Fig. 5.7. In both left and right panels the initial state is entangled with different phase relations between partial a_1 and a_2 modes; repeating the SPLIT operation disentangles to a pure a_1 (left) or a_2 (right) state.

5.3 Rectangular Pulse

Having analyzed our system numerically using a parabolic pulsed magnetic field and explored linear ramps in the prior sections, we found that in the same physical structure, depending on the shape of the pulsed magnetic field, different unitary magnon-mediated quantum gates can be realized [40]. We now move to consider an analytically solvable interaction protocol based on a rectangular pulse. Namely, we consider a hybrid magnon–photon system that consists of two photonic resonators having degenerate frequencies ω_p and one magnonic resonator with a dynamically tuned resonance frequency $\omega_m(t)$.

The photonic resonators are not directly coupled with each other but are both coupled with the magnonic mode with the coupling rate g. In this hybrid system, we consider a simple analytically solvable interaction protocol that can be experimentally

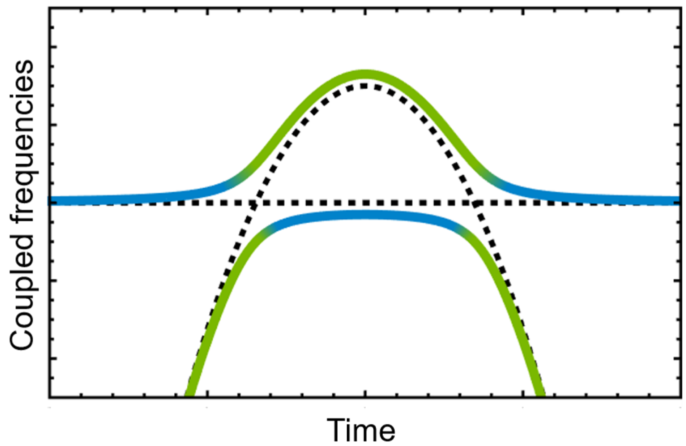

Figure 5.9: Instantaneous eigenfrequencies of Eq. (5.1) for the parabolic profile Eq. (5.4). Color indicates mode content: magnonic a_{m} (green) and photonic a_1 (blue).

realized with rectangular magnetic-field pulses of sufficiently large magnitude, shown schematically in Fig. 5.10.

Initially ($t < 0$) the frequency difference $|\omega_m - \omega_p| \gg g$ and interaction between the subsystems can be ignored. At $t = 0$ the magnonic mode frequency $\omega_m(t)$ is brought within the efficient interaction interval $\Delta = \omega_m - \omega_p \sim g$ and is held constant for the duration T. After $t = T$, the magnonic frequency is once again moved out of the photonic resonance region and any interaction between the subsystems stops. Similar to the parabolically shaped pulsed magnetic field, depending on the control pulse parameters Δ and T, different behaviors of the hybrid system can be realized.

Of particular interest is the situation in which the magnonic and photonic subsystems stay completely decoupled after the action of the control pulse. Such a case corresponds to a unitary operation on the photonic modes, realized through the indirect magnon-mediated coupling, and is of great importance for practical applications of magnonic resonators in quantum computing systems.

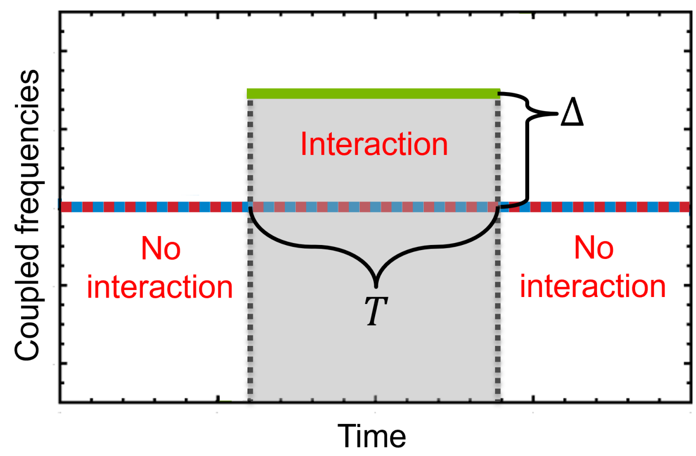

Figure 5.10: Rectangular control-pulse protocol. The magnon frequency $\omega_m(t)$ is abruptly tuned from far detuning $|\omega_m - \omega_p| \gg g$ to a fixed detuning $\Delta = \omega_m - \omega_p \sim g$, held for a duration T, and then returned far off resonance. This defines the constant-detuning interaction window that implements the analytically solvable gate.

Using our model, we derived a simple analytical condition is obtained for realizing unitary magnon-mediated operations. Namely, for each detuning Δ there exists an infinite series of pulse durations

$$T_n(\Delta) = \frac{2n\pi}{\sqrt{8g^2 + \Delta^2}}, \tag{5.5}$$

providing unitary conditions, where n is a positive integer. The resulting effect of the magnon interaction on the photonic subsystem, in this case, can be described by a 2×2 unitary matrix

$$U_n = e^{i\theta_n} \begin{pmatrix} \cos(\theta_n) & i\sin(\theta_n) \\ i\sin(\theta_n) & \cos(\theta_n) \end{pmatrix}, \tag{5.6}$$

relating photonic states before and after the pulse magnon action. Here the inter-mode mixing angle is given by

$$\theta_n = n\pi/2 - T_n(\Delta)\Delta/4 \tag{5.7}$$

and is shown in Fig. 5.11 for the case of $n = 3$.

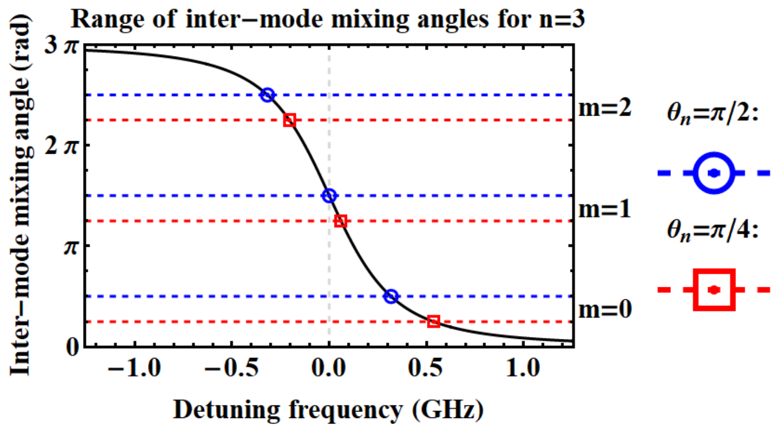

Figure 5.11: Inter-mode mixing angle Eq. (5.7) that parametrizes the unitary 2×2 action. For each branch n there exists a family of (Δ, T_n) giving the same θ_n; special cases $\theta_n = \pi/2 + m\pi$ (full exchange) and $\theta_n = \pi/4 + m\pi$ (50% mixing) are shown and further identified in the text.

For example, for $\theta_n = \pi/2 + m\pi$ (m is an integer number from 0 to $n-1$ that counts the number of solutions for every n-th unitary branch) a complete exchange of two photonic states is achieved, while $\theta_n = \pi/4 + m\pi$ describes 50% mixing behavior that allows one to entangle the two photonic modes.

The obtained results allow one to select pulse parameters realizing the desired unitary operation and also to analyze the limitations on the performance of the proposed magnon-mediated gates. Thus, it is clear that the simple rectangular pulse cannot realize all possible unitary gates since the matrix U_n depends only on one continuous parameter (θ_n), while the general 2×2 unitary matrix has four independent parameters. On the other hand, this pulse profile is sufficient to achieve an arbitrary exchange angle θ_n. The shortest pulse duration for which a complete exchange ($\theta_n = \pi/2$) is possible is $T_{\min} = \pi/(g\sqrt{2})$ and is realized at exact resonance $\Delta = 0$. In any n-th unitary branch, the pulse duration time $T_n(\Delta_{n,m})$ is minimized at $m = 0, n-1$, as shown in Fig. 5.12.

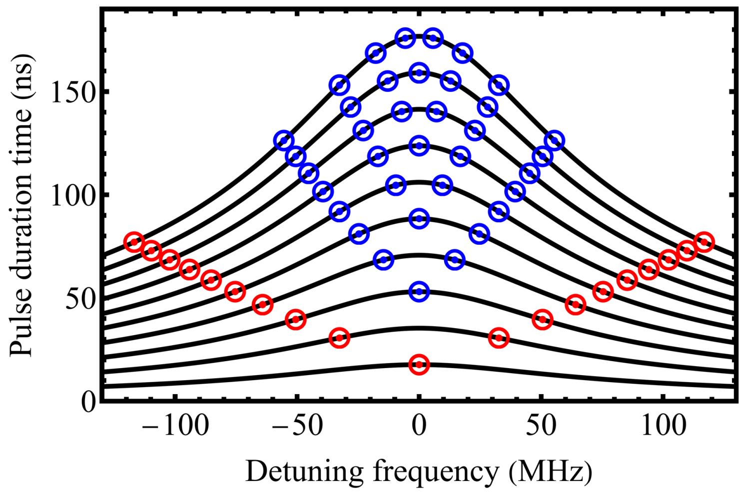

Figure 5.12: Pulse durations $T_n(\Delta)$ for unitary operation branches. Each branch n admits multiple detunings $\Delta_{n,m}$ achieving a given exchange angle; the shortest duration $T_{\min} = \pi/(g\sqrt{2})$ occurs at exact resonance $\Delta = 0$.

Our results also show a possibility to realize magnon-mediated unitary gates working in off-resonance conditions $|\Delta| \geq g$. For example, a $\theta_n = \pi/2$ gate can be realized with $\Delta = 18(2/19)^{1/2}g$ and $T_{10} = (19/2)^{1/2}\pi/g$. While such off-resonance operations require longer interaction times, their advantage in comparison to resonance-type operations is that the magnonic and photonic subsystems remain only weakly coupled throughout the whole process. This may lead to weaker decoherence of the quantum photonic subsystem caused by spin–lattice relaxation processes in the magnonic resonator. In general, the nth unitary branch $T_n(\Delta)$ has n different detuning values Δ, for which a given exchange angle θ_n (up to multiples of π) is achieved, which leaves a lot of space for optimization of practical magnon-mediated unitary gates.

While the preceding analysis was performed for a dissipation-free system, the main results remain qualitatively unchanged once dissipation via the magnon damping rate Γ_{m} is introduced into the system. In this case, however, the effect of interaction on the photonic subsystem is described by a matrix U_n' that is only approximately unitary. This means that the impact of the dissipation can be described by an error factor

$$\epsilon = \|U_n - U_n'\|^2. \tag{5.8}$$

This error factor ϵ quantifies the deviation from perfect unitarity.

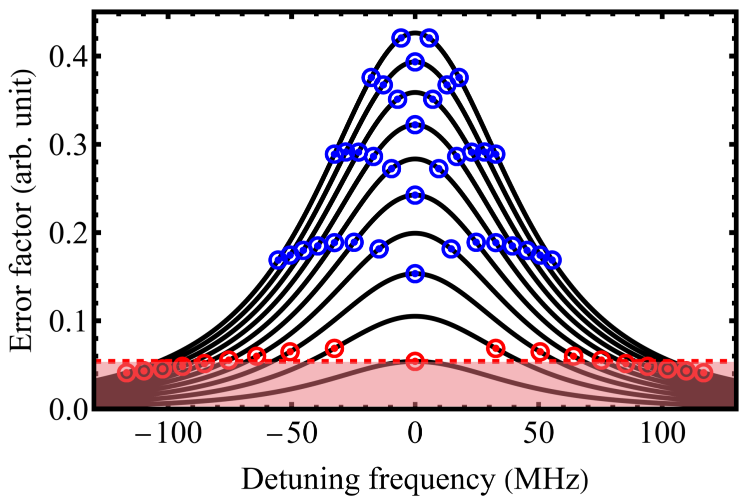

Figure 5.13: Unitary error factor $\epsilon = \|U_n - U_n'\|^2$ as a function of detuning. Dissipation maximizes the error at exact resonance ($\Delta = 0$) and suppresses it for far-off-resonant operation ($|\Delta| \gg g$), where coupling is weak but coherence losses are reduced.

Interestingly, though the shortest pulse duration for a complete photonic exchange ($\theta_n = \pi/2$) remains $T_{\min} = \pi/g\sqrt{2}$ and is realized at exact resonance $\Delta = 0$, due to the presence of dissipation, the error factor is largest here. In contrast, in the weak coupling regime ($g \ll |\Delta|$) the error factor trends to zero for far-off-resonant operation, even as n approaches ∞. This unexpected result is summarized in Fig. 5.13. The error is maximized at exact resonance ($\Delta = 0$) where the coupling is strongest, while it is suppressed for far-off-resonant operation ($|\Delta| \gg g$) where the coupling is weak but coherence losses are reduced.

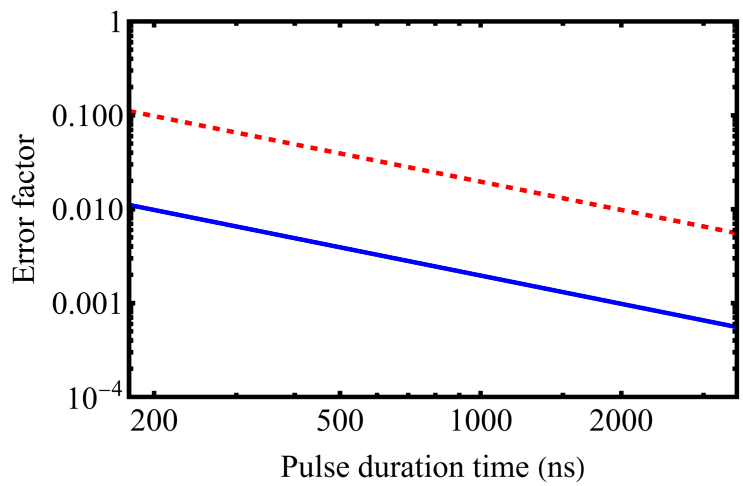

Figure 5.14: Long-time limit of the error factor Eq. (5.9)for off-resonant coupling: "ideal" film with $\Gamma_m = 6.28\ \mu s^{-1}$ (solid blue) versus "poor" film with $\Gamma_m = 62.8\ \mu s^{-1}$ (dotted red), for $g/2\pi = 20$ MHz. Increasing detuning $|\Delta|$ and pulse duration T suppresses error even with larger damping.

In the case when $T_n(\Delta)$ is minimized for every nth set of pulse durations, the impact of dissipation can be described in the long-time, off-resonant limit by an error factor

$$\epsilon \approx \frac{2\Gamma_m \Theta^2}{T g^2}. \tag{5.9}$$

The error factor is minimized as $T \to \infty$ and $|\Delta| \gg g$, where off-resonance coupling occurs. Conversely, the error factor is maximized as $T \to \infty$ and $\Delta = 0$, where on-resonance coupling occurs. Moreover, we can make a comparison of damping rates shown in Fig. 5.14, where the dotted line shows a magnon damping rate which is ten times larger than that of the solid line. The trend in Fig. 5.14 shows that even when magnon damping rate is increased by an order of magnitude, operation at larger Δ and longer T suppresses the error. In conclusion, these results imply that high-fidelity (i.e., low-error) operation can be achieved by increasing the pulse duration T and detuning Δ even in the case of a poor film where the dissipative effects of the magnon damping rate are much larger than normal.

5.4 Conclusion

This chapter has introduced three fundamental protocols for dynamic magnon tuning: linear ramps for state transfer, parabolic ramps for SWAP and SPLIT operations, and rectangular pulses for analytically solvable gates. We have analyzed these protocols within the classical framework, which, as shown in Section 3.4, provides a direct and intuitive analogy to the single-excitation ($N = 1$) quantum regime.

The key insight from all three protocols is that the temporal profile of the control pulse is a powerful resource for engineering coherent operations. The analysis of the rectangular pulse also revealed a crucial strategy for mitigating errors: off-resonant operation, while slower, can achieve higher fidelity by minimizing the system's exposure to the dominant magnon damping channel.

These concepts—controlling interactions in the time domain and leveraging off-resonant tuning—are the foundational principles for the fully quantum protocols developed in the remainder of this dissertation. We will now move beyond the $N = 1$ classical analogue and apply these principles to the multi-excitation quantum regime in Chapters 6, 7, and 8.

CHAPTER SIX

TIME-DOMAIN TWO-MAGNON INTERFERENCE

This chapter presents a model system for controllable two-magnon interference in the time domain. This two-magnon interference, i.e., a magnonic analog to the photonic Hong–Ou–Mandel (HOM) effect, is supported by a tunable magnonic beam splitter operation formed in a hybrid magnonic system comprising a pair of mutually-coupled magnon modes. By applying a tailored time-dependent magnetic field, magnons can be excited independently in each mode and subsequently brought into interaction, shifting from independent to collective oscillations, to realize a controllable magnonic beam splitter. When the beam splitter operation is applied to an initially unentangled two-magnon state, a maximally entangled magnonic N00N state with tunable phase sensitivity is produced. Importantly, this simple scheme enables the detection, generation, and manipulation of such entangled magnon states. These findings suggest that two-magnon interference in hybrid magnonic systems may enable novel quantum metrological devices to study fundamental magnon dynamics and contribute to developing hybrid magnonic quantum computing architectures.

6.1 Two-Particle Interference

Two-particle interference forms the basis of the HOM effect [144] and supports the functionality of many quantum technologies [145]. A standard example of two-particle interference is the photonic HOM effect, where two indistinguishable photons entering a balanced 50:50 beam splitter undergo quantum interference to form path-entangled output states, resulting in a distinctive dip in the coincidence rate [144], [145], [146]. Since its first demonstration in quantum optics [144], HOM interference has become central to quantum information science [145], enabling critical applications in entanglement generation, quantum computing, and quantum metrology [147], [148], [149], [150], among others [145]. Beyond optics, two-particle interference has also been observed in systems of bosonic and even fermionic quantum objects, such as, e.g., electrons, atoms, and phonons, reflecting a broader push toward hybrid quantum platforms [145]. Despite this progress, the implementation of HOM interference in magnonic systems remains largely underdeveloped, having only recently received attention [151], [152], [153], [154]. This gap is particularly surprising given the potential of magnons to serve as mediators of quantum information in hybrid systems[24], [39], [40].

In this chapter, we introduce a general and minimal model system for realizing two-magnon interference entirely in the time domain. Our protocol is agnostic to specific device geometries and relies exclusively on tunable dynamically-induced magnon-magnon interactions. By modulating a time-dependent magnetic field, we control the resonance conditions of two magnon modes to enact a tunable magnonic temporal beam splitter operation capable of generating and detecting maximally entangled magnonic N00N states from initially separable states. This approach establishes a purely magnonic analog of the HOM effect that is both experimentally accessible and conceptually transparent. This simplicity allows our model to be adapted to a broad range of candidate geometries and viable experimental platforms, including, e.g., synthetic antiferromagnets and remotely-coupled magnon resonators (see Fig. 6.1(a), (b)).

The significance of our approach is underscored by ongoing advancements in designs of single-magnon sources [70] and enhanced fabrication methods that facilitate stronger on-chip magnon-photon coupling within hybrid quantum magnonic architectures [70], [155]. These improved fabrication methods, such as those used in YIG-based systems and planar magnetic heterostructures, have made precise temporal control of magnon interactions increasingly feasible [41], [72], [73]. These developments suggest that time-domain control protocols, like the one we propose, could be implemented with existing or near-future technology [71], [72], [73].

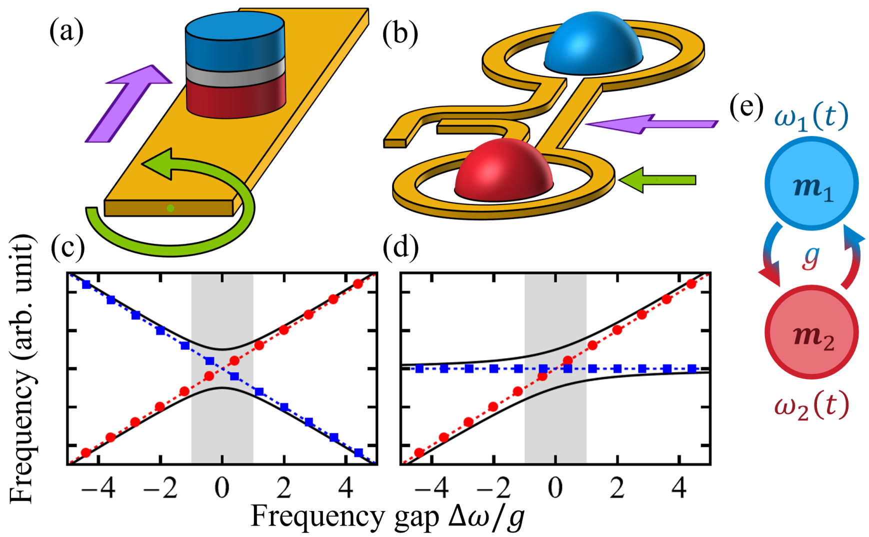

Figure 6.1: Candidate geometries and shared dynamics of (a, c) directly-coupled and (b, d) indirectly-coupled model hybrid magnonic systems for implementing time-domain two-magnon interference. (a) Directly-coupled magnon modes in a synthetic antiferromagnet (FM/nonmagnetic (NM)/FM trilayer) atop a CPW, enabling single-mode frequency control via mutual tuning. (b) Indirectly-coupled magnon modes in a pair of YIG spheres remotely coupled by a SC resonator, allowing independent multi-mode frequency control. (c) Coupled and uncoupled dynamics for the directly-coupled system in (a) under pulsed resonance protocols. (d) Coupled and uncoupled dynamics for the indirectly-coupled system in (b), exhibiting qualitatively similar behavior as in (c). (e) Generalized schematic of the hybrid magnonic system, abstracted from geometry to emphasize its implementation-independent character and critical parameters.

Our simple, versatile model system thus provides a practical route toward integrating magnon-enabled quantum elements into quantum computing and metrology platforms. This aligns with current trends that emphasize scalable and integrative quantum solutions. Ultimately, our work lays a crucial foundation for exploring quantum interference effects within magnonic systems and demonstrates the feasibility and flexibility of time-domain magnonic interference as a fundamental resource in quantum magnonics. We demonstrate how to form, analyze, and manipulate entangled magnonic states, characterize the dynamics of the temporal beam splitter operation, and propose a phase-shifting protocol as an example application of the entangled states. Together, these results position time-domain two-magnon interference as a viable technique for quantum state control in hybrid magnonic systems and advance magnonic HOM interferometry as a viable tool in hybrid quantum systems.

6.2 Two-Magnon Interference

We consider a model hybrid magnonic system designed to realize our proposed time-domain two-magnon interference protocol consisting of two magnon modes characterized by tunable resonance frequencies $\omega_1(t)$ and $\omega_2(t)$ that are coherently coupled with a coupling rate g. The interaction between these two magnon modes can be dynamically controlled through their frequency gap, $\Delta\omega(t) = \omega_1(t) - \omega_2(t)$, using, e.g., a time-dependent external magnetic field $B(t)$. When the modes are near resonance ($|\Delta\omega| \lesssim g$), the system is in the strong coupling regime, and coherent magnon-magnon interactions enable quantum information exchange and quantum interference, supporting the formation of quantum entanglement. Conversely, when the modes are substantially detuned ($|\Delta\omega| \gg g$), the system is in the weak coupling regime, and the two modes evolve nearly independently, allowing them to be addressed individually. This means that by applying precisely timed external magnetic field pulses $B(t)$, one can controllably bring the system into and out of resonance to enable dynamic magnon-magnon interactions, the essential mechanism for achieving time-domain two-magnon interference.

Here, we offer two candidate geometries for consideration that exemplify our general approach, which are illustrated in Fig. 6.1, representing limiting cases of directly-coupled and indirectly-coupled magnonic systems. The first geometry in Fig. 6.1(a) involves a synthetic antiferromagnet comprising a FM/NM/FM trilayer, exploiting direct coupling between magnon modes and providing a single control over magnon resonance frequencies (see Fig. 6.1(a), (c)). The second geometry employs indirectly-coupled magnon modes within YIG spheres that are remotely connected via a

SC resonator, allowing independent frequency control (see Fig. 6.1(b), (d)). Despite these distinct configurations, both systems exhibit analogous coupled and uncoupled dynamical behaviors (see Fig. 6.1(c), (d)) essential for our interference protocol, and can be generalized to a system of mutually-coupled magnon modes (see Fig. 6.1(e)) which is geometry-agnostic.

Operationally, the magnon modes are initially excited independently when substantially detuned, creating separable input states. A precisely timed magnetic pulse then dynamically brings the modes into resonance, forming a tunable temporal magnonic beam splitter operation. This operation converts initially separable magnon states into maximally entangled magnonic N00N states, enabling both the generation and subsequent detection of entanglement via two-magnon interference. Importantly, our protocol's temporal flexibility allows direct manipulation of the resulting quantum states by adjusting pulse timing and shape, providing enhanced control over entanglement characteristics.

In the simplest case, we consider rectangular magnetic field pulses with negligible rise and fall times, defined entirely by two parameters: the interaction time τ and the frequency gap $\Delta\omega$ (see Fig. 6.2(a), (b)). These parameters control the strength and timing of the magnon-magnon interaction by dynamically tuning the resonance condition. By reducing the frequency gap $\Delta\omega$ to bring the system into resonance ($|\Delta\omega| \ll g$) for a controlled interaction time τ, we induce coherent exchange between magnon modes. This process enables temporal magnonic analogs of beam splitting operations traditionally performed in spatial optical interferometry.

To characterize the pulse parameters, we define the magnonic TBS as a pulse tuned such that the transition probability of a single magnon between modes is exactly 50 % during the operation. That is, we initialize the system in a separable, unentangled single-magnon input state $|1\rangle \otimes |0\rangle$, where one magnon mode is in the excited state $|1\rangle$ and the other magnon mode is in the ground state $|0\rangle$. Then, we apply the TBS pulse and

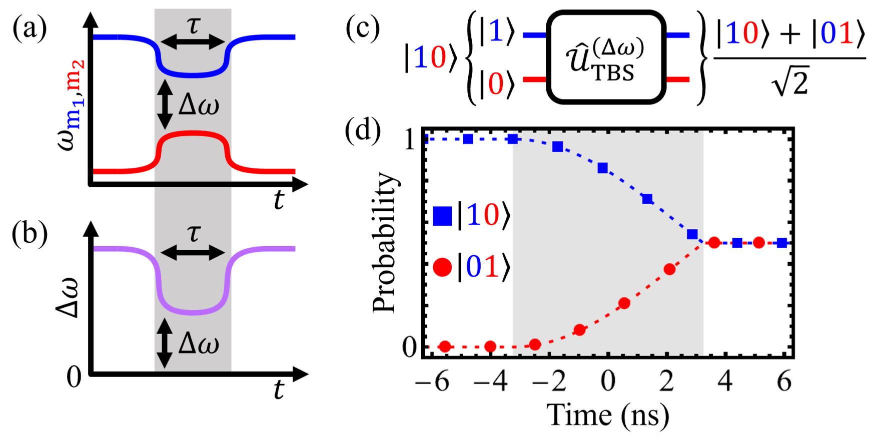

Figure 6.2: Magnon-magnon temporal beam splitter (TBS) pulse protocol characterization with single-magnon interference. (a) Resonance frequencies $\omega_1(t)$ and $\omega_2(t)$ of the two magnon modes approach one another during application of a rectangular magnetic field pulse. (b) Resulting time evolution of the frequency gap $\Delta\omega(t)$, which is held constant for a duration τ to allow coherent interaction. (c) Quantum circuit diagram of the TBS operation, represented by the unitary operator $\hat{\mathcal{U}}_{\text{TBS}}^{(\Delta\omega)}$, which depends on the frequency gap $\Delta\omega$, with the interaction time τ set by the condition for a balanced 50:50 beam splitter.s (d) Simulated time evolution of an initial $|10\rangle$ state under the TBS pulse, demonstrating coherent magnon population transfer and the formation of an equal superposition $(|10\rangle + |01\rangle)/\sqrt{2}$.

evolve the system into the entangled single-magnon state $\alpha|1\rangle \otimes |0\rangle + \beta|0\rangle \otimes |1\rangle$, where choosing τ and $\Delta\omega$ such that $|\alpha| = |\beta| = 1/\sqrt{2}$ defines a balanced magnonic TBS. The resulting interference behavior forms the basis for generating, detecting, and manipulating entangled magnonic states in our protocol when the input state is a separable unentangled two-magnon state $|1\rangle \otimes |1\rangle$.

6.3 Hamiltonian and Subspace Model

To simulate the coherent evolution of our model, we use the specific case of the general Hamiltonian from Eq. (3.8) for $Q = 0$ qubits and $M = 2$ magnon modes:

$$\hat{\mathcal{H}}(t)/\hbar = \omega_1(t)\, \hat{m}_1^\dagger \hat{m}_1 + \omega_2(t)\, \hat{m}_2^\dagger \hat{m}_2 + \tilde{g}_{12}\, \hat{m}_1^\dagger \hat{m}_2 + \tilde{g}_{12}^*\, \hat{m}_2^\dagger \hat{m}_1, \tag{6.1}$$

where $\tilde{g}_{12}$ is the inter-magnon coupling rate. As this is the only coupling in this chapter, for notational simplicity, we refer to it as $g \equiv \tilde{g}_{12}$. As established in Section 3.2, this Hamiltonian conserves the total number of quanta $N = m_1 + m_2$. We restrict our analysis to $N \leq 2$, corresponding to the physical scenario of initializing the system with at most one magnon in each mode.

This number conservation block-decomposes the system into the independent subspaces $\mathcal{H}_0$, $\mathcal{H}_1$, and $\mathcal{H}_2$. The specific Hamiltonian matrices for the non-trivial $N = 1$ and $N = 2$ subspaces are explicitly defined in **Case 2** of Section 3.3 and are summarized in Table 3.1.

The dynamics of this system are solved by calculating the unitary propagator $\hat{\mathcal{U}}(t, t_0)$ for each subspace, as defined in Eq. (3.25). Since the protocol in this chapter uses rectangular pulses, the evolution for a given pulse of duration τ at a constant detuning $\Delta\omega$ is a simple matrix exponential:

$$\hat{\mathcal{U}}_{\mathrm{TBS}}^{(\Delta\omega)} = \hat{\mathcal{U}}_0(\Delta\omega, \tau) = \exp\left((-i/\hbar)\,\hat{\mathcal{H}}(\Delta\omega)\,\tau\right). \tag{6.2}$$

In accordance with the noise analysis in Section 2.3.5, we focus on the idealized, unitary dynamics to isolate the coherent features of time-domain interference. We do not include noise channels, as their effect is secondary to the coherent protocol itself (a method for measuring their rates is presented in Chapter 7).

6.4 Magnon-Magnon Temporal Beam Splitter Pulse

We begin by examining the dynamics of a hybrid magnonic system subject to a rectangular magnetic pulse designed to implement a TBS operation. The system is initialized in a single-magnon state, such as $|10\rangle$, with the two magnon modes initially far detuned from one another, preventing interaction. A pulsed field is applied to dynamically reduce the frequency gap $\Delta\omega = \omega_1(t) - \omega_2(t)$, bringing the modes into near-resonance for a controlled duration τ, as shown in Fig. 6.2(a)–(b). This interaction window enables coherent magnon exchange governed by direct mode coupling. The time-domain control of $\Delta\omega(t)$ and the pulse duration τ forms the basis of the magnon-magnon TBS protocol.

The effective operation implemented by this pulsed interaction is denoted as $\hat{\mathcal{U}}_{\text{TBS}}^{(\Delta\omega)}$, which acts non-trivially during the resonance interval, as shown in the circuit diagram in Fig. 6.2(c). To realize a balanced 50:50 beam splitter, the interaction time τ is selected such that the single-magnon tunneling probability between modes is $1/2$. This corresponds to the condition $\tau = \pi/(2g)$, where g is the effective coupling strength during resonance. The unitary operator $\hat{\mathcal{U}}_{\text{TBS}}$ depends parametrically on $\Delta\omega$, while τ is tuned to ensure symmetric output amplitudes. The resulting operation mirrors the action of a symmetric photonic beam splitter, enabling coherent population redistribution without relying on spatial coupling geometries.

Figure 6.2(d) shows the simulated time evolution of a system initialized in the state $|10\rangle$ under the application of a balanced TBS pulse. The final state evolves into a superposition $(|10\rangle + |01\rangle)/\sqrt{2}$, confirming coherent delocalization of the magnon and validating the TBS protocol as a temporal analog of an optical beam splitter. These results demonstrate that a simple, geometry-independent detuning pulse enables deterministic and reversible magnonic beam splitting in the time domain, forming the foundation for controlled interference and entanglement in subsequent protocols.

6.5 Generation of Entangled Magnon States

We begin by simulating the application of a temporal magnonic TBS pulse to an initial state with one magnon in each mode, $|11\rangle$. This operation, illustrated in the quantum circuit in Fig. 6.3(a), is described by the unitary $\hat{\mathcal{U}}_{\text{TBS}}^{(\Delta\omega)}$. When the interaction time τ is set to produce a balanced beam splitter, the output state becomes the path-entangled N00N state $(|20\rangle + e^{i2\varphi}|02\rangle)/\sqrt{2}$, as shown in the simulation in Fig. 6.3(b). This transformation is a hallmark of two-particle quantum interference, akin to the HOM effect for photons.

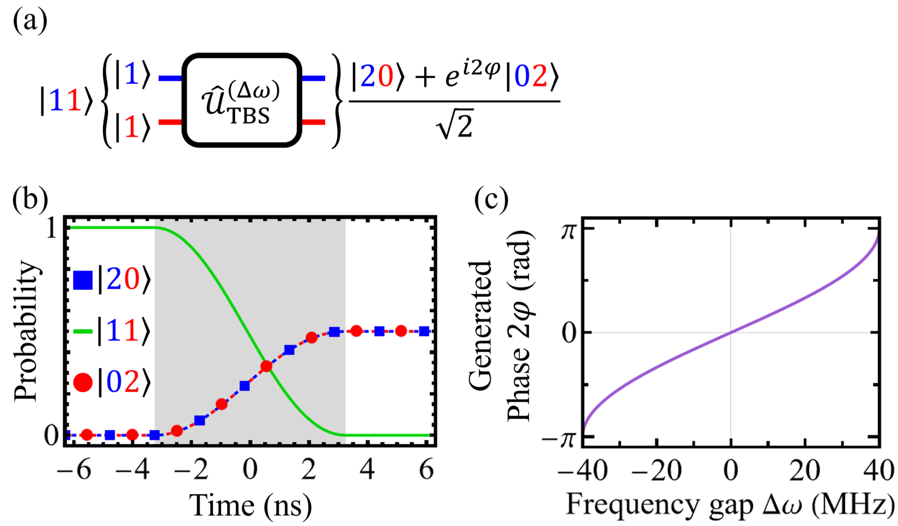

Figure 6.3: Generation of arbitrary entangled magnonic $N00N$ states using a TBS pulse. (a) Quantum circuit representation of the TBS pulse acting on the input state $|11\rangle$, resulting in N00N state generation. (b) Simulated time evolution showing coherent transformation from $|11\rangle$ to the entangled state $(|20\rangle + e^{i2\varphi}|02\rangle)/\sqrt{2}$. (c) Generated phase φ of the N00N state as a function of the frequency gap $\Delta\omega$.

Figure 6.3(c) quantifies the phase φ of the generated N00N state as a function of the frequency gap $\Delta\omega$. Because the total operation is unitary, the phase φ is coherently imprinted onto the output state, and its value can be precisely controlled by the detuning during the beam splitter interaction. This level of tunability demonstrates that our protocol enables not only the generation but also the continuous manipulation of entangled states using temporal control. Such control is critical for applications in quantum sensing and interferometric measurement where phase information encodes physical parameters.

6.6 Detection of Entangled Magnon States

To detect the generated N00N states, we apply the same beam splitter pulse in reverse, as depicted in the circuit diagram in Fig. 6.4(a). In this configuration, an entangled input state of the form $(|20\rangle + e^{i2\varphi'}|02\rangle)/\sqrt{2}$ evolves back into the separable state $|11\rangle$. The reverse evolution is shown in Fig. 6.4(b), where the magnon population redistributes from the entangled configuration to the coincidence basis. This time-reversed operation serves as a detection mechanism for N00N states, enabling phase-sensitive discrimination through direct population measurements.

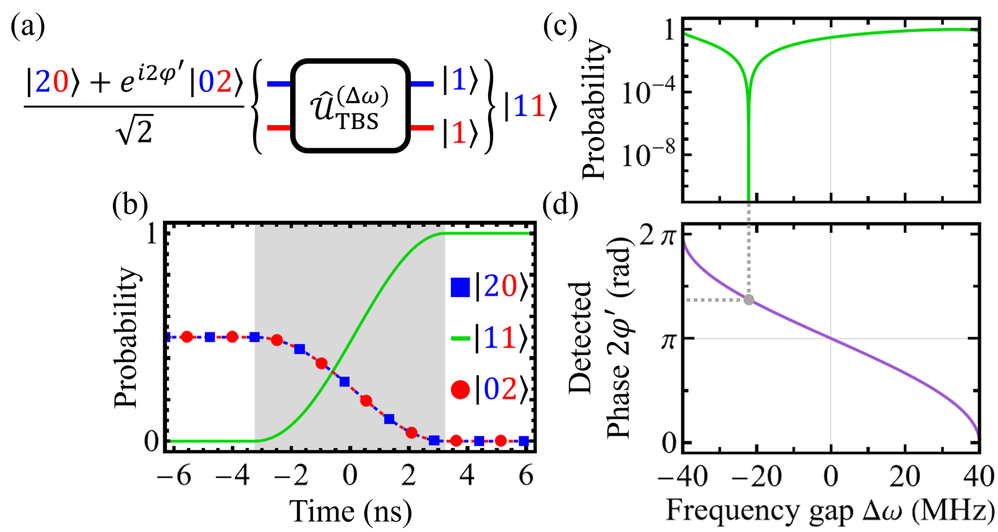

Figure 6.4: Detection of arbitrary entangled magnonic $N00N$ states using a TBS pulse. (a) Quantum circuit for applying the TBS pulse to an entangled input state $(|20\rangle + e^{i2\varphi'}|02\rangle)/\sqrt{2}$ to reverse the operation. (b) Time evolution showing reconstruction of the separable $|11\rangle$ state from an entangled input. (c) Anti-coincidence probability signal of detecting the $|11\rangle$ output state versus frequency gap, revealing interference-induced suppression of the $|11\rangle$ population at a specific frequency gap that correspond to the particular phase of the input $N00N$ state being detected. (d) Map of detected phase φ' of the input N00N state as a function of the frequency gap $\Delta\omega$ used to detect it.

Figures 6.4(c) and 6.4(d) provide the phase-sensitive readout mechanism. The anti-coincidence probability (the suppression of the $|11\rangle$ state) is plotted in Fig. 6.4(c). This signal shows a clear interference dip, and the frequency gap $\Delta\omega$ at which this minimum occurs corresponds to the detected phase φ' of the input N00N state. This relationship is summarized in the map in Fig. 6.4(d), which shows the detected phase as a function of the detuning. The visibility of this interference confirms the presence of coherent two-magnon interference and validates the operation of the TBS pulse as a high-fidelity entanglement detector. These results demonstrate that the same temporal protocol can serve as both an entanglement generator and phase-resolved measurement tool, using only direct magnon-magnon interactions.

6.7 Entangled Magnon State Manipulation

We demonstrate coherent manipulation of entangled magnonic N00N states using a simple pulse-based protocol that applies a controllable phase shift between the $|20\rangle$ and $|02\rangle$ components. To demonstrate coherent control over magnonic entangled states, we investigate the manipulation of a N00N state using a TBS pulse sequence. The protocol begins with a preexisting entangled state of the form $(|20\rangle + |02\rangle)/\sqrt{2}$, which is subjected to two consecutive TBS pulses separated by a detuned evolution interval. This sequence, shown in Fig. 6.5(a), implements a phase gate that transforms the input into $(|20\rangle + e^{i2\Delta\varphi}|02\rangle)/\sqrt{2}$, where $\Delta\varphi$ is a relative phase imprinted by the detuning. This operation is realized by the unitary operator $\hat{\mathcal{U}}_{\mathrm{TBS}}^{(\Delta\omega)}\hat{\mathcal{U}}_{\mathrm{TBS}}^{(-\Delta\omega)}$, which preserves the entangled nature of the state while enabling phase control.

The induced phase shift $\Delta\varphi$ depends exclusively on the frequency gap $\Delta\omega$ during the detuned interval, as confirmed by simulations shown in Fig. 6.5(b). The results demonstrate continuous and deterministic tuning of the output phase, with no degradation of the quantum coherence. Because this protocol does not rely on ancillary systems or additional degrees of freedom, it provides a direct and efficient mechanism for manipulating the internal structure of magnonic entangled states.

This form of temporal phase manipulation enables critical quantum control functionality analogous to optical phase shifters in photonic quantum circuits. It supports

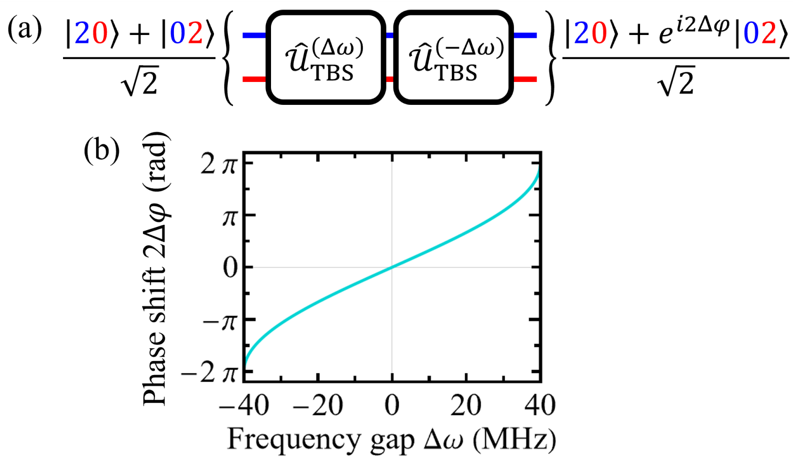

Figure 6.5: Manipulation of magnonic N00N states using a TBS phase gate. (a) Quantum circuit representation of the phase shift protocol, consisting of two TBS pulses with conjugate frequency gaps. This operation acts on the initial N00N state $(|20\rangle + |02\rangle)/\sqrt{2}$ and produces an output state $(|20\rangle + e^{i2\Delta\varphi}|02\rangle)/\sqrt{2}$, where $\Delta\varphi$ is the induced phase shift. (b) Dependence of the accumulated phase shift $\Delta\varphi$ on the frequency gap $\Delta\omega$, illustrating deterministic and continuous phase tunability.

robust, reversible operations that preserve entanglement, making it well-suited for quantum information encoding, interferometric sensing, and quantum logic. The demonstrated tunability and coherence retention establish the TBS-based phase gate as a foundational tool for scalable magnonic quantum technologies. These results underscore the potential of time-domain magnonic protocols as building blocks for scalable quantum logic, metrology, and sensing platforms based on spin-wave excitations.

6.8 Conclusion

We have introduced a generalized, geometry-independent protocol for time-domain two-magnon interference using direct magnon-magnon interactions and dynamically controlled detuning. By implementing a tunable temporal magnonic beam splitter, our model system enables the generation, detection, and manipulation of maximally entangled magnonic N00N states–realizing a magnonic analog of the HOM effect. This work demonstrates that time-domain control alone suffices to implement magnonic interferometry, eliminating the need for ancillary quantum systems or complex spatial routing.

The simplicity and flexibility of our protocol make it broadly compatible with both directly and indirectly coupled magnonic systems, including synthetic antiferromagnet FM/NM/FM trilayers and remotely coupled YIG spheres. Numerical simulations confirm high-fidelity interference and entanglement generation across these platforms. As advances in single-magnon sources, strong coupling, and device fabrication continue, the protocol provides a promising foundation for scalable quantum-enhanced sensing, magnonic logic, and hybrid quantum information processing architectures.

CHAPTER SEVEN

TEMPORAL MAGNON-QUBIT MACH-ZEHNDER INTERFEROMETER

In this chapter, a temporal magnon-qubit MZI is proposed. The interferometer is based on controllable entanglement of a microwave qubit and a magnonic state, achieved by application of a pulsed magnetic field playing the role of a magnon–qubit TBS. Analogous to a typical MZI, the generated interference pattern of the final qubit population carries information about the magnon dynamics. One important application of the proposed scheme is the study of single magnon decoherence. Interestingly, this scheme allows one to independently determine rates of two possible decoherence channels. This may help enable single magnon state applications and answer fundamental questions of quasiparticle decoherence at single quantum levels.

7.1 Mach–Zehnder Interferometer

MZIs have been a fundamental tool in physics for more than a century, originally designed to explore the interference patterns of light in the classical regime [156], [157] and since evolving into versatile tools for exploring quantum phenomena [147], [148], [158], [159], [160]. In its simplest form, an MZI uses a pair of beam splitters to generate interference patterns by splitting a beam of light into two physical paths and later recombining them before measurement [156], [157], [161], [162]. Continued development has shown that various excitations can be used to realize MZIs and MZI-like devices, such as, e.g., coherent light [162], lasers [161], single photons [147], [148], [159], [163], [164], electrons [165], phonons [166], qubits [160], and magnons [167], [168], [169], [170], [171], [172], [173], [174]. These recent extensions of MZIs illustrate the shift from classical to quantum regime explorations and highlight the adaptability of the underlying MZI framework to more complex quantum tasks.

One exciting extension of MZIs into the quantum regime is their application to hybrid quantum systems, where, among the various excitations used to realize MZIs, magnons–quanta of spin waves–hold the potential for unique functionality as they can easily couple with both bosonic and fermionic excitations [30], [31], [32], [33], [34], [35], [39], [40], [41], [70]. Additionally, the resonant frequency of magnons can be tuned via external magnetic fields [30], [31], [32], [33], [34], [35], [39], [40], which means that a time-varying magnetic field may lead to novel functionality [40], [41], [70]. This means that existing hybrid magnonic MZIs and MZI-like devices [167], [168], [169], [171], [172], [173], [174], [175] could be developed further to study multiple different physical systems simultaneously. This versatility makes magnons a compelling candidate for developing practical hybrid quantum systems and for investigating fundamental aspects of quantum dynamics at single-quanta level.

In this chapter, we propose to realize a temporal-domain MZI that operates in the quantum regime by entangling the states of a magnon and a qubit. Specifically, this temporal magnon-qubit MZI leverages dynamic interaction between these two subsystems, where a pulsed magnetic field plays the role of a "beam splitter" for dynamically coupling and uncoupling the magnon and qubit modes, thereby controllably entangling and unentangling them. The key difference between our approach and existing magnon-based MZI-like devices lies in the temporal nature of the interactions: instead of using spatially separated paths, we use time-dependent operations between the magnon and qubit subsystems to entangle and unentangle them. This allows us to observe quantum interference effects in the qubit's final state, which directly encodes information about the magnon's dynamics during the evolution period. This measurement scheme is especially well-suited for probing the decoherence processes of magnons, which are typically short-lived compared to qubits [36].

The need for this temporal magnon-qubit MZI is motivated by recent advances in quantum magnonics, including the development of single magnon sources [70] and strong coupling between magnons and other quantum systems [30], [31], [32], [33], [34], [35], [39], [40], [41], [70]. These advances create a unique opportunity to study single magnon decoherence (SMD) mechanisms–critical for advancing quantum technologies that operate with finite magnon number states. Our proposed interferometer provides a straightforward method for exploring these processes, particularly by enabling the independent measurement of different magnon decoherence channels, such as damping and dephasing.

The temporal magnon-qubit MZI we introduce here represents a step forward in the study of hybrid quantum systems, specifically for magnonic systems. Its ability to probe various aspects of single magnon dynamics could enable new applications in quantum sensing and quantum information processing.

7.2 Scheme of Temporal MZI

We propose to realize a temporal magnon-qubit MZI using a simple hybrid quantum system shown schematically in Fig. 7.1(a). In this work we make no assumptions about the underlying geometry of such a system, and instead investigate what dynamics might be possible, agnostic to any implementation. This system consists of a single magnon mode $|m\rangle$ with resonance frequency ω_m and a single qubit $|q\rangle$ with resonance frequency ω_q that are coupled to one another with a rate g. Interaction between these two modes can be controlled by varying the magnon-qubit frequency gap $\Delta\omega = \omega_m - \omega_q$. When $|\Delta\omega| \lesssim g$, a coherent exchange of quantum information between two subsystems is possible. In the opposite limit $|\Delta\omega| \gg g$ the magnon and qubit modes evolve almost independently.

The magnon-qubit gap $\Delta\omega$ can be controlled dynamically by, e.g., a time-dependent magnetic field $B(t)$ that changes the magnon frequency $\omega_m(t)$ (see Fig. 7.1(b)). This means that by delivering short magnetic pulses one can controllably

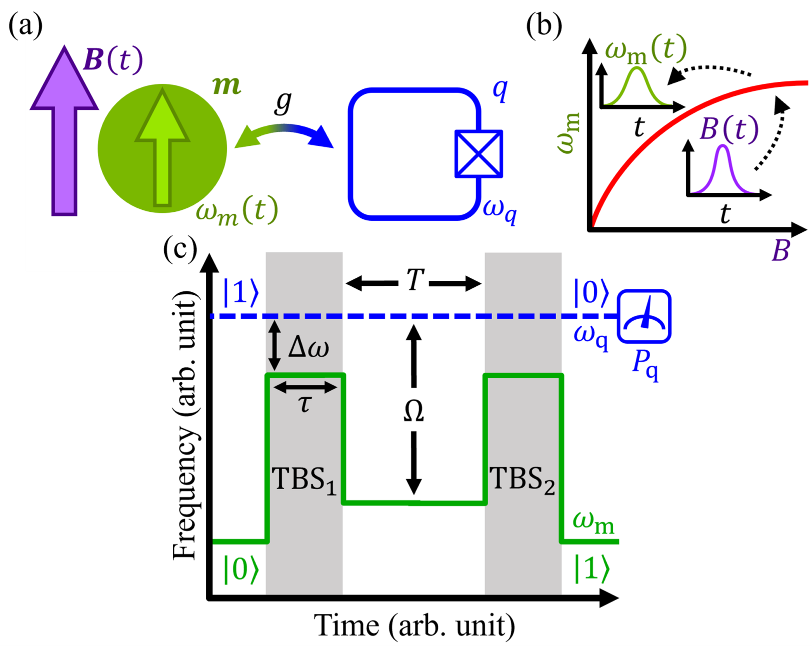

Figure 7.1: (a) Schematic diagram of a hybrid quantum system consisting of coupled magnon mode (m) and qubit (q). (b) Dynamic control of the magnon frequency $\omega_m(t)$ by pulsed magnetic field $B(t)$. (c) Temporal MZI: two magnetic pulses $\rm TBS_1$ and $\rm TBS_2$ (shaded areas) serve as temporal "beam splitters" that couple magnon and qubit modes. In between the pulses, the two subsystems evolve independently. The interference result is measured as the final qubit state.

bring the two subsystems into resonance and the strong coupling regime ($|\Delta\omega| \ll g$), leading to entanglement between the magnon and qubit, or out of resonance, detuned from one another and into the weak coupling regime ($|\Delta\omega| \gg g$), causing the two modes to evolve independently. These so-called dynamic magnon-qubit interactions are the essential mechanism enabling the temporal interferometric scheme.

In the simplest case, we can consider a rectangular pulse of $\omega_m(t)$ with negligible rise and fall times (see TBS_1 or TBS_2 pulses in Fig. 7.1(c)). Then, the result of the dynamic magnon-qubit interaction can be described by using only two parameters of the pulsed magnetic field profile–the interaction time τ and the frequency gap $\Delta\omega$.

This pulse-driven control allows us to sequence multiple dynamic magnon-qubit interactions to perform operations analogous to beam splitting and recombination in traditional MZIs. In this temporal version, the "splitting" and "recombination" are achieved by applying two pulses separated by a free evolution time T, during which the magnon and qubit evolve independently due to a large frequency gap Ω.

The measurement scheme underlying the temporal magnon-qubit MZI follows a simple protocol, shown schematically in Fig. 7.1(c). Initially, the system is prepared in the unentangled state $|1\rangle \otimes |0\rangle$, with the qubit in the excited state $|1\rangle$ and the magnon mode in the ground state $|0\rangle$. A magnetic field pulse TBS_1 then acts as a magnon-qubit beam splitter, reducing their detuning, temporarily coupling the two subsystems and allowing them to interact, thereby entangling their states. Right after the end of the TBS_1 the qubit-magnon system is in the entangled state $\alpha\,|1\rangle \otimes |0\rangle + \beta\,|0\rangle \otimes |1\rangle$, where the coefficients α and β depend on the parameters of the "beam splitter" pulse τ and $\Delta\omega$. In particular, it is possible to choose $|\alpha| = |\beta| = 1/\sqrt{2}$, which corresponds to a usual 50:50 beam splitter.

After a free evolution period T, during which the system remains entangled, but evolves freely due to a large frequency gap Ω, a second magnetic pulse TBS_2 is applied, effectively "unentangling" the magnon and qubit. Then, the magnon and qubit subsystems return to a large detuning. Finally, one measures the final qubit state, namely, probability P_q that the qubit is in the excited state. These measurements allow one to recover the interference pattern formed by the qubit and magnon mode and reveal insights into the quantum processes happening during free magnon evolution (e.g., magnon decoherence mechanisms).

7.3 Hamiltonian and Simulation Model

To simulate the evolution of this system, we use the specific $Q = 1$, $M = 1$ case of the general Hamiltonian from Eq. (3.8):

$$\hat{\mathcal{H}}(t)/\hbar = \omega_m(t)\,\hat{m}^\dagger\hat{m} + \omega_q\,\hat{q}^\dagger\hat{q} + g\,\hat{q}^\dagger\hat{m} + g^*\,\hat{m}^\dagger\hat{q}, \tag{7.1}$$

where $\hat{m}$ and $\hat{q}$ are the magnon and qubit operators, respectively, and g is their coupling rate.

As the protocol starts with a single excitation (in the qubit), the Hamiltonian conserves the total number of quanta $N = q + m = 1$. The dynamics are therefore confined to the $N = 1$ subspace, which is a simple two-level system. This corresponds to **Case 1** in Table 3.1, with the basis states $\{|1;0\rangle, |0;1\rangle\}$ (representing $|q = 1, m = 0\rangle$ and $|q = 0, m = 1\rangle$). The trivial $N = 0$ ground state $|0;0\rangle$ is uncoupled from this manifold.

The protocol consists of a sequence of rectangular pulses where the Hamiltonian is piecewise-constant. As described in Section 3.7, the propagator for each step is a simple matrix exponential $\hat{\mathcal{U}}_0(\Delta\omega, \tau)$ (from Eq. (3.26)). The propagator for the full MZI sequence is the product of the three steps:

$$\hat{\mathcal{U}}_{\text{MZI}} = \hat{\mathcal{U}}_0(\Delta\omega, \tau)\,\hat{\mathcal{U}}_0(\Omega, T)\,\hat{\mathcal{U}}_0(\Delta\omega, \tau). \tag{7.2}$$

The final qubit population P_{q} is the probability of being in the $|1;0\rangle$ state after this evolution.

To simulate noise, we use the GKSL master equation framework (Eq. (3.27)). As established by the noise hierarchy in Section 2.3.5, we include only the dominant magnon decoherence channels, $\Gamma_{\text{amplitude}}$ and Γ_{phase}. The simulation is then performed by vectorizing the density matrix and solving Eq. (3.30) using the numerical methods described in Section 3.7.

7.4 Magnon-Qubit Temporal Beam Splitter Pulse

The TBS between the magnon and qubit states is formed by resonantly coupling the two subsystems for some time τ and frequency gap $\Delta\omega$, thereby allowing them to interact and coherently exchange quantum information (see Fig. 7.2(a, d, g)). The scattering probability P_{TBS} between the states (the probability of an excitation scattering from the qubit to the magnon state) is described by

$$P_{\text{TBS}}(\Delta\omega, \tau) = \frac{(2g)^2}{\Delta\omega^2 + (2g)^2} \sin^2\left(\frac{\tau}{2}\sqrt{\Delta\omega^2 + (2g)^2}\right). \tag{7.3}$$

The functionality of the TBS pulse can also be described in terms of a splitting angle θ_{BS} such that $P_{\text{TBS}} = \sin^2(\theta_{\text{BS}})$. When $P_{\text{TBS}}(\Delta\omega, \tau) = 1/2$, which corresponds to a splitting angle $\theta_{\text{BS}} = \pi/4$, a balanced "50:50" magnon-qubit TBS pulse is achieved, as depicted. Fig. 7.2(b, e, h) and (c, f, i) show that when the balanced TBS pulse is applied, it can maximally entangle the two subsystems or "unentangle" a previously entangled state, similarly to a standard optical beam splitter. This serves as the primary interference mechanism enabling the functionality of the temporal magnon-qubit MZI.

Interestingly, a balanced 50:50 TBS can be achieved for different detunings $\Delta\omega$ by properly adjusting the pulse duration τ. TBS pulses with different $\Delta\omega$ allow one to create entangled magnon-qubit states of the form $\left(|0,1\rangle + e^{i\phi}|1,0\rangle\right)/\sqrt{2}$ with different phase shift ϕ. For $|\Delta\omega| > 2g$, the maximum splitting angle θ_{BS} falls below $\pi/2$ and a balanced TBS is no longer possible.

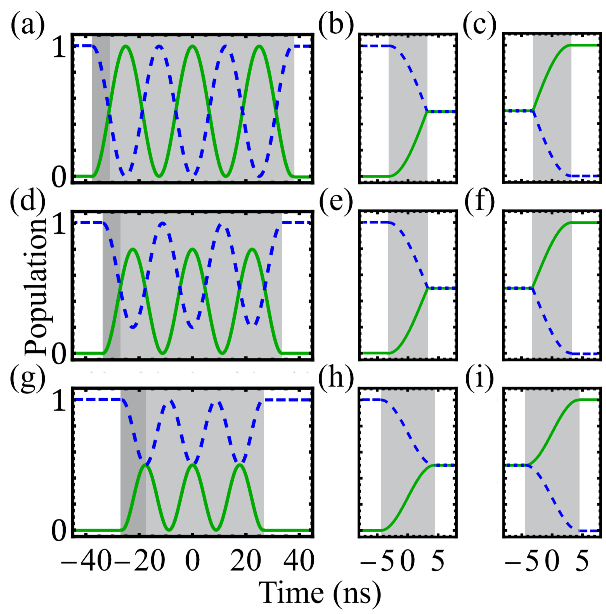

Figure 7.2: Operation of magnon-qubit TBS. Left column: coherent magnon-qubit dynamics during coupling pulse with different detunings: (a) $\Delta\omega = 0$, (d) $\Delta\omega = g$, (g) $\Delta\omega = 2g$. Central and right columns show "entangling" and "unentangling" operations for balanced TBS pulses: (b, c) $\tau = 6.25$ ns, (e, f) $\tau = 6.49$ ns, (h, i) $\tau = 8.84$ ns. Magnon-qubit coupling rate $g = 2\pi \times 20$ MHz.

In the following, we utilize a balanced TBS pulse where the two subsystems are in exact resonance $\Delta\omega = 0$, which achieves the TBS operation in the least amount of time ($\tau \approx 6.25$ ns).

7.5 Influence of Off-Resonant Coupling on Free Evolution

A key component of the proposed temporal magnon-qubit MZI measurement scheme is the period of free evolution, the region of time T during which magnon and qubit subsystems evolve independently. The interference pattern generated by the final qubit population P_{q} thus relies on the parameters that govern this period of free evolution, the frequency gap Ω and the interaction time T. Of these two parameters, the frequency gap Ω is the most critical, as it dictates the level to which the evolution is "free" or not, i.e., how much influence the residual off-resonance magnon-qubit coupling has on the dynamics of the system. An example of such influence is shown in Fig. 7.3(b), where one can see small-amplitude high-frequency oscillations during the period of "free" magnon and qubit evolution.

The main effects of the off-resonant coupling are the change of the period of the interference pattern and reduction of its visibility. In the fixed-frequency-gap operation mode, when the gap Ω is kept constant and the free evolution period T is varied, the period ΔT of the interference pattern is $\Delta T = 2\pi/\sqrt{\Omega^2 + 4g^2} \approx 2\pi/|\Omega| - (4\pi g^2)/|\Omega|^3$, and its deviation from the ideal case $\Delta T = 2\pi/|\Omega|$ is negligible for $|\Omega| > 5g$ (see Fig. 7.3(e)).

The visibility ν of the interference pattern is defined by the extrema of the qubit population,

$$\nu = (P_{\mathrm{max}} - P_{\mathrm{min}})/(P_{\mathrm{max}} + P_{\mathrm{min}}). \tag{7.4}$$

Residual off-resonant coupling does not reduce visibility ν for resonant TBS $\Delta\omega = 0$ and unitary "free" magnon evolution. However, for $\Delta\omega \neq 0$ or in the presence of non-unitary jump processes, the interference pattern visibility degrades at small frequency gaps Ω (see

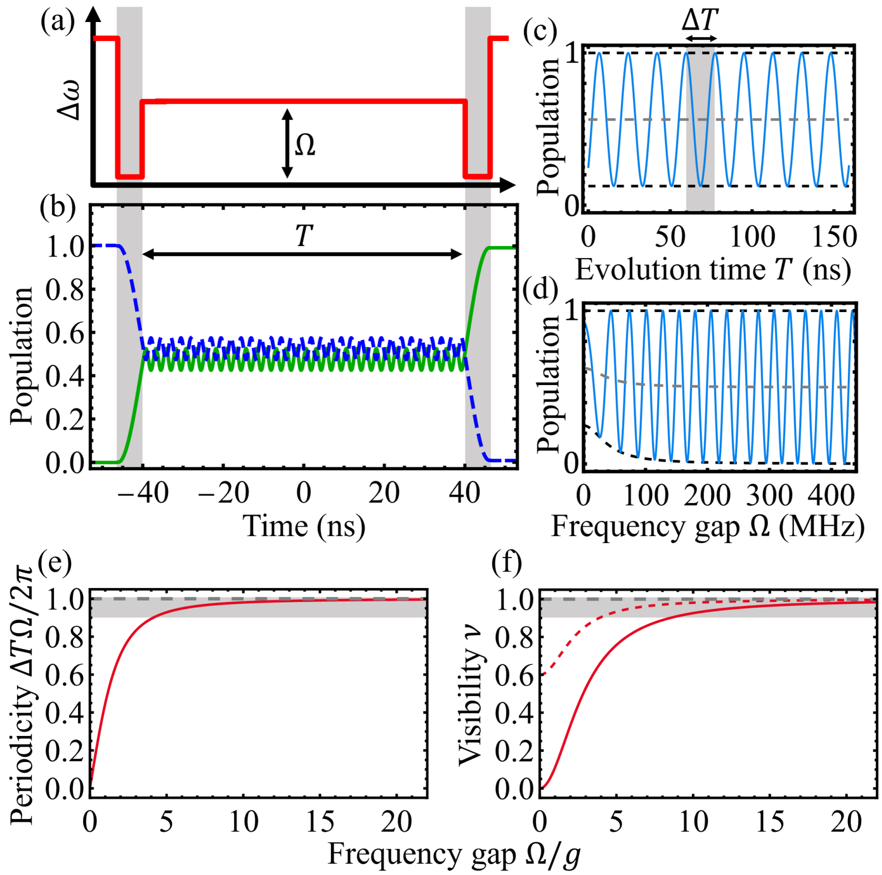

Figure 7.3: Influence of the residual off-resonance coupling on temporal magnon-qubit MZI measurement scheme. (a) Cartoon diagram of magnon-qubit frequency gap $\Delta\omega(t)$ during MZI operation. (b) Numerical simulation of the magnon (green) and qubit (blue) populations during MZI operation. Fast small-amplitude oscillations during "free" evolution are due to the residual coupling. (c) Interference pattern for fixed-frequency-gap mode (fixed Ω and varying T). (d) Interference pattern for fixed-evolution-time mode. (e) Dependence of the periodicity of the interference pattern on the frequency gap Ω; gray highlight indicates periodicity $\geq 90\%$. (f) Dependence of the visibility on the frequency gap Ω; gray highlight indicates visibility $\geq 90\%$, dashed and solid red lines denote TBS pulse detunings of g and $2g$, respectively. Simulation parameters: $g = 2\pi \times 20$ MHz, $\Delta\omega = 2\pi\times 20$ MHz, $\tau \approx 6.49$ ns, (b) $\Omega = 2\pi\times 400$ MHz, $T \approx 79.3$ ns, (c) $\Omega = 2\pi\times 40$ MHz, (d) $T \approx 39.8$ ns.

Fig. 7.3(f)). Similarly to the deviations in period ΔT, these spurious effects are negligible for $|\Omega| > 5g$. Thus, this inequality determines the condition under which magnon-qubit dynamics can be considered as uncoupled in the MZI scheme.

7.6 Measurement of Single Magnon Decoherence

One interesting application of the proposed temporal magnon-qubit MZI is the measurement of SMD mechanisms. Here, we consider two potential noise channels that correspond to the more commonly encountered interactions that influence decoherence, namely, amplitude $L_{\text{amplitude}}$ and phase L_{phase} noise. Amplitude noise can be thought of as the process of a magnon encountering an inhomogeneity and scattering into a phonon. In this case, the noise process is not number-conserving and can be described by the operator $L_{\text{amplitude}} = \hat{m}$, with an accompanying amplitude noise rate $\Gamma_{\text{amplitude}}$. Phase noise can be thought of as the process of a magnon-phonon scattering, which results in a random change of the magnon phase. In this case, the noise process is number-conserving and described by $L_{\text{phase}} = \hat{m}^{\dagger}\hat{m}$, with an accompanying phase noise rate Γ_{phase}.

The impact of these two SMD mechanisms can clearly be seen in Fig. 7.4. When only $L_{\text{amplitude}}$ is present as shown in Fig. 7.4(a), the average qubit population P_{avg} gradually decreases as the interaction time is increased, while ν remains relatively high. In contrast, when only L_{phase} is present as shown in Fig. 7.4(b), P_{avg} remains unchanged at the 50% value, but ν degrades with T. In a system with a mixture of two noise channels, such as that shown in Fig. 7.4(c), the resulting interference pattern demonstrates both these effects. It is interesting that both $\Gamma_{\text{amplitude}}$ and Γ_{phase} rates can be found from the measurements of the MZI interference pattern. Namely,

$$\Gamma_{\text{amplitude}} = \frac{1}{T} \ln\left(\frac{1}{2(P_{\max} + P_{\min}) - 1}\right), \tag{7.5}$$

and

$$\Gamma_{\text{phase}} = \frac{1}{T} \ln\left(\frac{2(P_{\max} + P_{\min}) - 1}{(P_{\max} - P_{\min})^2}\right), \tag{7.6}$$

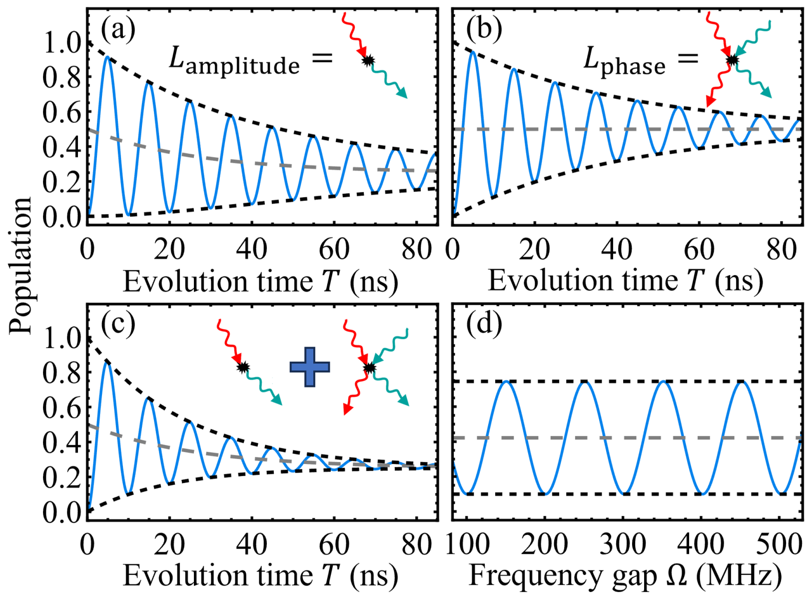

Figure 7.4: Interference patterns for measurement of single magnon decoherence. (a–c) Fixed-frequency-gap interference pattern, (d) fixed-evolution-time interference pattern. (a) Amplitude noise, (b) phase noise, (c, d) mixture of amplitude and phase noise. Dashed black and gray lines in (a–d) indicate the envelope (i.e., the maxima P_{max} and minima P_{min}) and average P_{avg} of the final qubit population (solid blue lines), respectively. Simulation parameters: (a–d) $g = 2\pi \times 20$ MHz, $\Delta\omega = 0$, $\tau \approx 6.25$ ns, (a–c) $\Omega = 2\pi \times 100$ MHz, (d) $T \approx 9.95$ ns, (a, c, d) $\Gamma_{\text{amplitude}} \approx 37.7\ \mu\text{s}^{-1}$, (b–d) $\Gamma_{\text{phase}} \approx 50.3\ \mu\text{s}^{-1}$.

where $P_{\max}$ and $P_{\min}$ are, respectively, the maximum and minimum final qubit populations. In practical implementation of this SMD measurement scheme, it is better to work in the fixed-interaction-time (T) mode with varying frequency gap Ω. This mode simplifies measurements of $P_{\max}$ and $P_{\min}$, which are independent of the gap Ω (see Fig. 7.4(d)).

7.7 Conclusion

In this chapter, we have proposed a novel type of MZI based on a "beam splitting" operation realized in the time domain. Applied to a hybrid system of SC qubit and microwave magnon, this scheme provides new means to study magnon dynamics at the quantum level. In particular, the proposed interferometer can be used to study different channels of SMD and allows one to separately determine two common noise rates $\Gamma_{\text{amplitude}}$ and Γ_{phase} by simply measuring the extrema of the qubit population forming the temporal interference pattern.

CHAPTER EIGHT

UNIVERSAL SET OF MAGNON-MEDIATED QUANTUM GATES

In this chapter, we explore the full potential of dynamic magnon-mediated interactions for quantum information processing. We demonstrate that arbitrary quantum operations can be realized on a hybrid quantum system of mutually non-interacting qubits coupled to a single ancilla magnonic mode, with control applied *only* to the magnon. This demonstration represents the critical achievement of this dissertation.

As established in Section 2.1.5, the short lifetime of magnons compared to SC qubits makes them unsuitable as quantum memories. However, their strong coupling to other excitations makes them ideal mediators for coherently manipulating and transducing information between otherwise disparate qubits. Our control scheme exploits this, acting exclusively on this magnonic mediator. Interaction is selectively enabled by dynamically tuning the magnon resonance frequency $\omega_m(t)$ into (or out of) resonance with a target qubit, such that the frequency gap $\Delta\omega_{1,2} = \omega_m(t) - \omega_{q_{1,2}}$ becomes comparable to the coupling rate $g_{1,2}$. Within this framework, we present protocols for arbitrary single-qubit rotations and a tunable two-qubit CPhase gate, which together form a universal set on the qubit subsystem.

Moreover, we show that this tunable CPhase gate is a one-parameter specialization of a more general, four-parameter family of two-qubit magnon-mediated quantum gates. This class of gates is related to the fSim gates used in demonstrations of quantum primacy [4], [5]. These results demonstrate the principal possibility of constructing a reconfigurable quantum computer where all operations are implemented by manipulating only the ancillary magnon, requiring no direct qubit-qubit interaction.

8.1 General Unitarity Condition for Magnon-Mediated Gates

Before we design specific gate protocols, we first need to establish the general condition for *any* magnon-mediated operation to be a valid, unitary gate on the qubit subspace.

The fundamental requirement is simple. The ancillary magnon mode must be fully disentangled from the qubit subsystem at both the start and the end of the operation. The protocol must therefore be a “catch and release” mechanism. The system starts in a separable state, for example $|\psi\rangle_q \otimes |0\rangle_m$. The magnon is then dynamically coupled to the qubits, forming a complex, entangled state across the full system. To complete the gate, the protocol must precisely reverse this process, returning the magnon to its initial $|0\rangle_m$ state. The final separable state is $|\psi'\rangle_q \otimes |0\rangle_m$, where the qubit subsystem has been left in a new, transformed state, $|\psi'\rangle_q = \hat{\mathcal{U}} |\psi\rangle_q$.

This ”catch and release” mechanism can be understood as the magnon acting as a temporary tool. The ”catch” phase of the protocol involves the magnon ”catching” quantum information from the qubits, which creates the temporary, complex, entangled state between the qubits and the magnon. This is the ”messy” part where the computation happens. The ”release” phase must then perfectly reverse this, ”releasing” the information entirely back to the qubits. The magnon must ”let go” completely and return to its original, empty vacuum state $|0\rangle_m$. This final “release” step is then the unitarity condition.

When this ”catch and release” is successful, the operator $\hat{\mathcal{U}}$ describes the net operation as a pure, unitary quantum gate that has acted *only* on the qubit subspace. Because the ancillary magnon has been returned to its original state, its involvement in the protocol, no matter how complex, becomes invisible in the final input-output relation. The equation $|\psi'\rangle_q = \hat{\mathcal{U}} |\psi\rangle_q$ is the mathematical statement of this successful gate; the final state of the qubits is *only* the initial state of the qubits transformed by $\hat{\mathcal{U}}$, with no other system left entangled or involved. The operation is therefore a valid, coherent manipulation of the qubit states.

As we demonstrated with the rectangular pulse in Chapter 5, this is achieved by precisely controlling the pulse detuning frequency gap $\Delta\omega$ and duration time τ. If the magnon is not returned to a separable state, the operation results in a complex entangled state of the full qubit-magnon system. This represents a loss of information and coherence from the qubit subspace and is therefore not a valid, unitary gate on the qubits alone. This general condition—that the system must begin and end unentangled—is foundational and applies to all the single-qubit and two-qubit gates developed below.

8.2 System Hamiltonian and Subspace Model

The specific system for this chapter consists of $Q = 2$ qubits and $M = 1$ magnon. Its Hamiltonian is a specific case of the general model from Eq. (3.8):

$$\hat{\mathcal{H}}(t)/\hbar = \omega_m(t)\hat{m}^\dagger\hat{m} + \omega_{q1}\hat{q}_1^\dagger\hat{q}_1 + \omega_{q2}\hat{q}_2^\dagger\hat{q}_2 + g_1\hat{q}_1^\dagger\hat{m} + g_1^*\hat{m}^\dagger\hat{q}_1 + g_2\hat{q}_2^\dagger\hat{m} + g_2^*\hat{m}^\dagger\hat{q}_2, \quad (8.1)$$

where $\hat{m}^\dagger$ ($\hat{m}$) and $\hat{q}_{1,2}^\dagger$ ($\hat{q}_{1,2}$) are the creation (annihilation) operators for the magnon and qubit modes, respectively. This Hamiltonian is the specific $Q = 2, M = 1$ system defined in **Case 3** of Section 3.3. As defined in Section 3.2, this Hamiltonian conserves the total number of quanta $N = q_1 + q_2 + m$. The dynamics can therefore be solved independently in each N- quanta subspace (QSS). These subspaces are listed in Table 3.1.

The Qubit Frequency Mismatch

A key feature of this model is the assumption of a large qubit frequency mismatch, $|\omega_{q_1} - \omega_{q_2}| \gg |g_{1,2}|$. This mismatch is a crucial resource, and a desirable feature in modern quantum hardware, as it is a primary method of construction to reduce crosstalk. Here, it ensures that the magnon mode, when tuned to a frequency near ω_{q_1} or ω_{q_2}, can only interact with *one* qubit at any given moment of time, either q_1 *or* q_2. This simplifies the N-QSS. For example, the 1-QSS, $\{|1, 0; 0\rangle, |0, 1; 0\rangle, |0, 0; 1\rangle\}$, effectively decouples

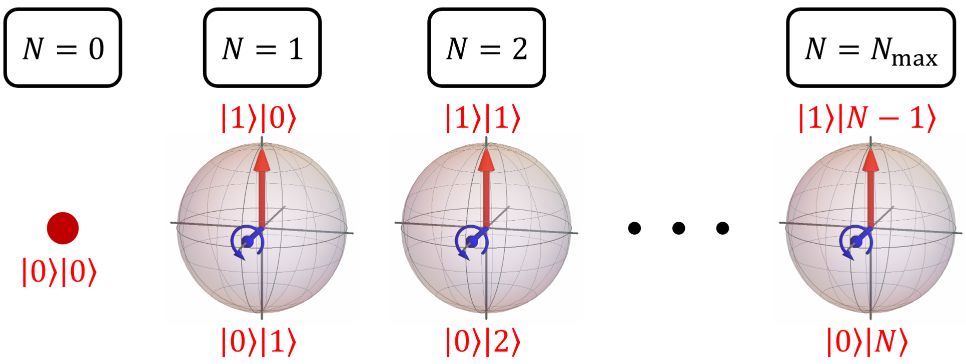

Figure 8.1: Schematic depiction of the N-QSS reduction to effective two-dimensional Bloch spheres ($N > 0$), enabled by the large qubit frequency mismatch. These N-QSS spheres evolve simultaneously under the same pulse but at different rates set by $g_{\text{eff}}^{(N)}$ (Eq. (8.4)). State labels map to the general $|q_t, m\rangle$ basis. The North Pole corresponds to the qubit-excited state $|1, N-1\rangle$ and the South Pole to the magnon-excited state $|0, N\rangle$.

into two independent two-level systems: $\{|1,0;0\rangle, |0,0;1\rangle\}$ (for $q_1 \leftrightarrow m$ exchange) and $\{|0,1;0\rangle, |0,0;1\rangle\}$ (for $q_2 \leftrightarrow m$ exchange).

This reduction allows each N-QSS (when one qubit is interacting) to be mapped onto an effective two-level system (and thus a standard Bloch sphere), as shown in Fig. 8.1. For $N \geq 1$, this subspace is spanned by the states $|1, N-1\rangle$ (one qubit excited) and $|0, N\rangle$ (zero qubits excited, N magnons). The state of each N-QSS $|\psi_N\rangle$ is described by

$$|\psi_N\rangle = c_{0,N}\; |0, N\rangle + c_{1,N-1}\; |1, N-1\rangle\,, \tag{8.2}$$

and evolves according to $i\hbar \dfrac{\partial\, |\psi_N\rangle}{\partial t} = \hat{\mathcal{H}}_N(t)\; |\psi_N\rangle$, where $\hat{\mathcal{H}}_N(t)$ is the N-QSS Hamiltonian:

$$i \begin{pmatrix} \dot{c}_{0,N} \\ \dot{c}_{1,N-1} \end{pmatrix} = \begin{pmatrix} N\,\omega_m(t) & g_{\text{eff}}^{(N)*} \\ g_{\text{eff}}^{(N)} & (N-1)\,\omega_m(t) + \omega_q \end{pmatrix} \begin{pmatrix} c_{0,N} \\ c_{1,N-1} \end{pmatrix}. \tag{8.3}$$

Crucially, the effective coupling rate for these N-QSS dynamics, $g_{\text{eff}}^{(N)}$, scales with the excitation number N as:

$$g_{\text{eff}}^{(N)} = \sqrt{N}\, g_{1,2}. \tag{8.4}$$

This N-dependence is the central mechanism of this chapter. It allows a single control pulse on the magnon to perform *different* operations on different N-QSS *simultaneously* (e.g., an R_Z gate on the 2-QSS while performing an identity gate on the 1-QSS). The time evolution $\hat{\mathcal{U}}_N$ for each subspace is then a simple rotation on its respective Bloch sphere, calculated using the numerical methods from Section 3.7:

$$\hat{\mathcal{U}}_N(\Delta\omega, \tau) = \exp\Big(-i\,\hat{\mathcal{H}}_N[\Delta\omega]\,\tau\Big). \tag{8.5}$$

8.3 Single Qubit Gates

As established in Section 8.2, the large qubit frequency mismatch ensures the magnon can only interact with one qubit at a time. For analyzing single-qubit gates, we can therefore first analyze a simpler $Q = 1, M = 1$ system. The relevant Hamiltonian and 1-QSS, $\{|1;0\rangle, |0;1\rangle\}$, are defined in **Case 1** of Section 3.3. A universal gate set requires the ability to perform arbitrary single-qubit rotations. We demonstrate two distinct magnon-mediated methods to achieve this.

Rotation with Coherent States: R_X and R_Y

In the "usual way" of driving a qubit, a magnon mode prepared in an initial coherent state with a large average number of magnons ($\bar{N} \gg 1$) can be used to invoke a fast, Rabi-like rotation of the qubit state. In this regime, the magnon mode acts as a classical drive. The angle of rotation is controlled by the duration of the resonant interaction pulse. The axis of rotation (X vs. Y) is set by the phase of the initial magnon coherent state; for example, an in-phase coherent state ($\phi = 0$) produces a drive along the

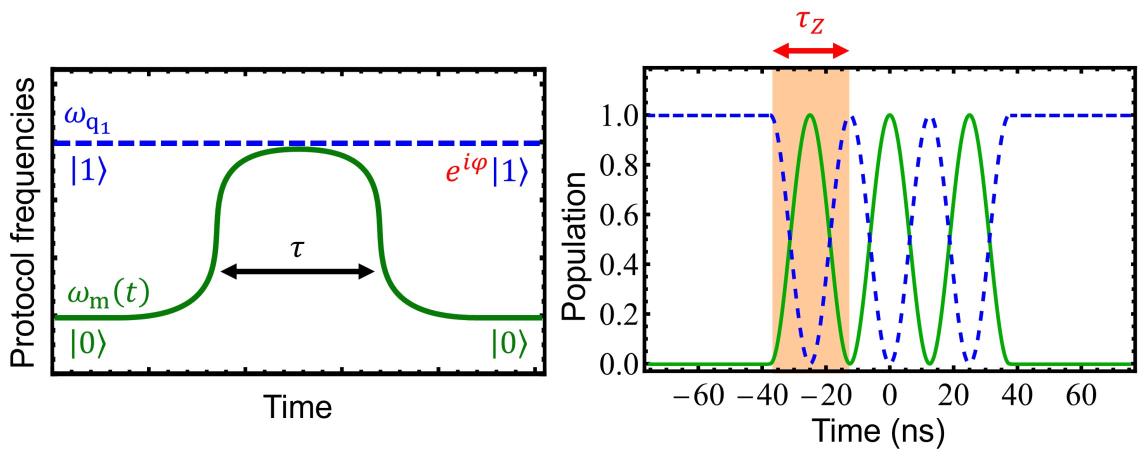

Figure 8.2: The R_Z gate protocol at exact resonance ($\Delta\omega = 0$): (left) schematic of the pulsed frequency profile with interaction time τ; (right) simulated time evolution of the qubit (initially $|1\rangle$) and the magnon (initially vacuum) populations over three oscillation periods, with a single R_Z period highlighted. Returning the population to the qubit while accruing a phase realizes R_Z.

X-axis (R_X rotation), while a quadrature-phase state ($\phi = \pi/2$) produces a drive along the Y-axis (R_Y rotation).

Rotation with Vacuum State: R_Z

While an R_Z rotation can, in principle, be constructed from a sequence of R_X and R_Y gates, our protocol can realize this rotation directly and more efficiently. This is achieved by using an interaction with the magnon mode while it is in its initial vacuum state, $|0\rangle_m$.

This protocol is not a simple Rabi drive; it is a complete, controlled excursion within the 1-QSS. As shown in Figures 8.2 and 8.3, the pulsed frequency profile $\omega_m(t)$ is precisely shaped to allow for an integer number of full oscillations of the state population between the qubit and the magnon. The population (dashed blue line) starts at the qubit, transfers entirely to the magnon (solid green line), and then returns perfectly to the qubit.

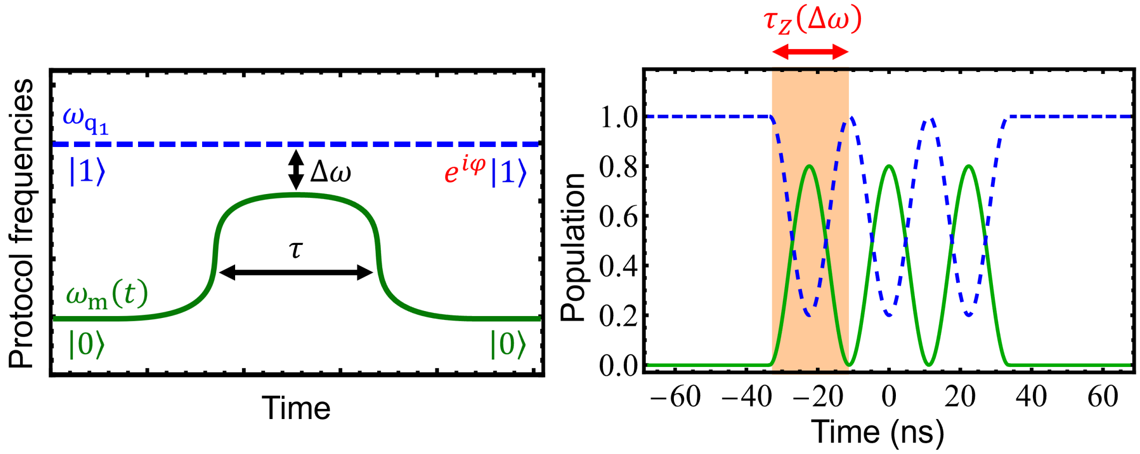

Figure 8.3: The detuned R_Z gate protocol ($\Delta\omega \neq 0$): (left) schematic of the pulsed frequency profile with interaction time τ; (right) simulated dynamics over three periods with the R_Z-realizing interval highlighted. Detuning modifies the exchange rate and the accrued phase, enabling continuous phase tuning at fixed τ.

This "catch and release" sequence ensures that the qubit and magnon subsystems are fully unentangled at the end of the operation ($c_m(\tau) = 0$), satisfying the general unitarity condition. However, the state acquires a controllable phase φ during this excursion. By changing the parameters of the frequency pulse $\omega_m(t)$, specifically the detuning $\Delta\omega$, R_Z rotations with different angles (phases) can be invoked. This continuous tunability is summarized in Fig. 8.4.

Mathematical Comparison of Coherent and Vacuum Protocols

The difference between these two protocols is clear from their respective equations of motion. In the 1-QSS, the **vacuum–R_Z protocol** couples the qubit amplitude $c_q(t)$ (representing $|1;0\rangle$) and the magnon amplitude $c_m(t)$ (representing $|0;1\rangle$) via the 1-QSS Hamiltonian:

$$\begin{aligned} i\,\dot{c}_q &= \tfrac{\Delta\omega}{2}\,c_q + g\,c_m, \\ i\,\dot{c}_m &= g\,c_q - \tfrac{\Delta\omega}{2}\,c_m, \end{aligned} \tag{8.6}$$

with the initial condition $c_m(0) = 0$. Selecting parameters $(\Delta\omega, \tau)$ such that $c_m(\tau) = 0$ returns the population to the qubit while imprinting a controllable phase on $c_q(\tau)$.

For the **coherent-state $R_{X,Y}$ protocol**, we replace the magnon operator $\hat{m}$ with a large classical amplitude $\alpha = \sqrt{\bar{N}}\, e^{i\phi_{\text{drive}}}$. This yields an effective drive on the qubit basis states c_1 (representing $|1\rangle$) and c_0 (representing $|0\rangle$):

$$\begin{aligned} i\,\dot{c}_1 &= \tfrac{\Delta\omega}{2}\, c_1 + (g\,\alpha)\, c_0, \\ i\,\dot{c}_0 &= (g\,\alpha^*)\, c_1 - \tfrac{\Delta\omega}{2}\, c_0. \end{aligned} \tag{8.7}$$

This is algebraically identical to Eq. (8.6), with the coupling g simply replaced by an effective, complex coupling $g_{\text{eff}} = g\alpha$. This makes it clear that choosing the phase of the coherent state α (i.e., ϕ_{drive}) determines the rotation axis. This comparison motivates our use of the vacuum-R_Z gate as a natural, resource-efficient primitive for our universal gate set.

R_Z Realization and Tunability with a Pulsed Frequency Profile

The R_Z gate is implemented by the simple pulsed frequency profile $\omega_m(t)$ shown in the following figures. To emphasize the mechanism and its tunability, we present the protocol and corresponding simulation for two cases.

Figure 8.2 shows the exact-resonance case ($\Delta\omega = 0$). The left panel shows the pulse profile, and the right panel shows the resulting sinusoidal population exchange. One full R_Z period τ_Z is highlighted, showing the population returning fully to the qubit (dashed blue line) after one full excursion into the magnon (solid green line).

Figure 8.3 shows the detuned case ($\Delta\omega \neq 0$). The detuning modifies the effective coupling, which changes two things: (1) the population never fully transfers to the magnon, and (2) the oscillation period $\tau_Z(\Delta\omega)$ is shorter. However, the principle is the same: after one full period, the population returns to the qubit, having acquired a different phase than in the resonant case.

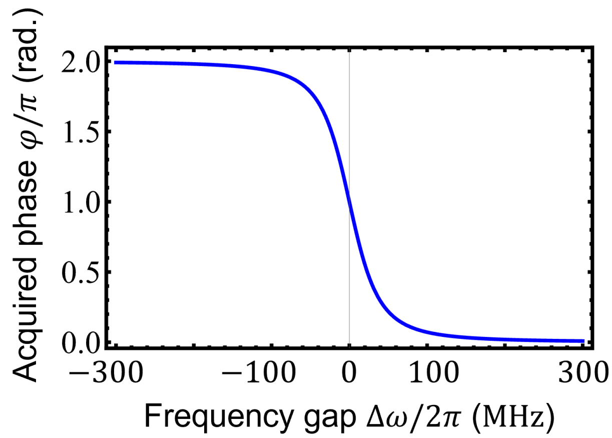

Figure 8.4: Acquired phase φ of the magnon-mediated R_Z gate versus the frequency gap $\Delta\omega$ used during the operation. This tunability curve summarizes how detuning continuously controls the gate angle.

Figure 8.4 summarizes the result. It plots the final acquired phase φ of the R_Z gate as a function of the detuning $\Delta\omega$ used during the pulse. This demonstrates the continuous control over the gate angle, which is a requirement for an arbitrary single-qubit rotation.

8.4 Two-Qubit Gates

Having established how to perform arbitrary rotations on a single qubit, we now return to the full $Q = 2, M = 1$ system (Eq. (8.1)) to construct the final, crucial piece of our universal gate set: a two-qubit entangling gate.

The core challenge remains the same as before. Our qubits, q_1 and q_2, are non-interacting by design. The only way to make them "talk" is through the ancillary magnon mode. To achieve this, we must leverage the central mechanism introduced in Section 8.2: the N-dependent effective coupling rate, $g_{\text{eff}}^{(N)}$ (Eq. (8.4)).

The strategy is to design a pulse sequence that performs a *different* operation on the 2-QSS (which corresponds to the $|1, 1\rangle$ state) than it does on the 1-QSS (corresponding to

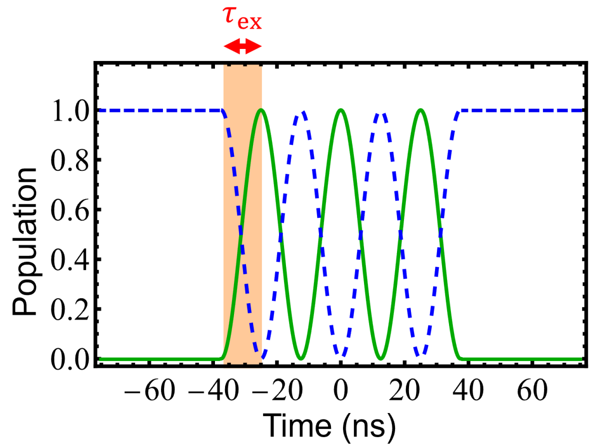

Figure 8.5: Half-period exchange between a qubit and the magnon mode. The plot shows the population dynamics for a single highlighted half-beating period (τ_{ex}) that exchanges the qubit and magnon states when the magnon is initially in vacuum $|0\rangle$. This $Z/2$ exchange (half of the R_Z cycle) is the lightweight boundary operation that removes and later restores information to the control qubit.

$|0,1\rangle$ and $|1,0\rangle$). This "differential rotation" *is* the entangling gate. The general method we use to achieve this is an elegant **three-stage protocol** which we will now detail.

The Three-Stage Exchange-Interact-Exchange Protocol

The key building block for this protocol is the **magnon-qubit exchange** operation (a π-pulse). This is simply the vacuum-R_Z protocol from the previous section, but stopped after exactly one-half period of oscillation ($\tau_{ex} \approx \pi/2g_{\text{eff}}^{(N)}$), as shown in Fig. 8.5.

This exchange is the necessary first and last step of any two-qubit gate. The overall protocol is a three-stage sequence:

1. **Exchange (Stage 1):** The state of the *control qubit* $|q_c\rangle$ is exchanged with the magnon mode $|m\rangle$, which starts in its vacuum state $|0\rangle_m$. (Exchange: $q_c \leftrightarrow m$).

2. **Interact (Stage 2):** A desired interaction, or unitary rotation protocol is performed on magnon mode $|m\rangle$ with the *target qubit* $|q_t\rangle$ in the q_t-m subsystem, which now contains the quantum information of the control qubit $|q_c\rangle$. (Interact: $q_t \leftrightarrow m$).
3. **Exchange (Stage 3):** The state of the magnon mode $|m\rangle$ is exchanged back into the *control qubit* $|q_c\rangle$, returning the magnon to the vacuum state. (Exchange: $q_c \leftrightarrow m$).

This "Exchange-Interact-Exchange" sequence ensures that the magnon, which acts as a temporary "bus" for the quantum information, is unentangled from the qubit subsystem at the end of the full operation, satisfying the general unitarity condition. The total unitary operation on the two-qubit state $|q_c, q_t\rangle$ is thus given by

$$\hat{\mathcal{U}}_{\text{gate}} = \hat{\mathcal{U}}_{\text{ex}} \cdot \hat{\mathcal{U}}_{\text{interact}} \cdot \hat{\mathcal{U}}_{\text{ex}}. \tag{8.8}$$

Unitarity Condition for the Two-Qubit Protocol

To be a valid gate on the qubit subspace, this three-stage protocol must satisfy the general unitarity condition. As we have established, the "Exchange" operation is only unitary when paired, and the key is that the system state just before the final exchange (Stage 3) must be in a form that allows the magnon to be returned to vacuum.

Let's trace the logic. During Stage 2 (the "Interact" stage), the control qubit q_c is in its ground state, so the system evolves in the $|0, q_t; m\rangle$ basis. The N-QSS Bloch spheres (Fig. 8.1) describe this q_t-m subsystem, which we now explicitly label as the 1-QSS and 2-QSS. The "North Pole" $|1, N-1\rangle$ corresponds to the state $|0, 1; N-1\rangle$ and the "South Pole" $|0, N\rangle$ corresponds to the state $|0, 0; N\rangle$.

The initial "Exchange" (Stage 1) maps the computational basis states onto the *poles* of these spheres:

- An initial $|1, 0; 0\rangle$ state becomes $|0, 0; 1\rangle$. This is the **South Pole** of the 1-QSS.
- An initial $|1, 1; 0\rangle$ state becomes $|0, 1; 1\rangle$. This is the **North Pole** of the 2-QSS.

This mapping is the key. To ensure the final "Exchange" (Stage 3) returns the magnon to vacuum, the "Interact" stage (Stage 2) must *return any populated sphere to its starting pole*. This is the geometric condition for unitarity. We must ensure that the state $|0, N\rangle$ (the South Pole) is unpopulated at the end of the "Interact" stage, as this state would be "stuck" in the magnon and break the unitarity.

Arbitrary Two-Qubit Gates (*ABC* Protocol)

The "Interact" stage (Stage 2) of the general protocol is itself a composite *three-step* pulse sequence. It is critical to distinguish this "three-step" $q_t \leftrightarrow m$ protocol from the "three-stage" $q_c \leftrightarrow m$ protocol it lives inside. We implement this interaction, which we call a unitary qubit-magnon rotation $\hat{\mathcal{U}}_{qm}$, by composing three controlled rotations (A, B, and C) of the N-QSS Bloch spheres:

$$\hat{\mathcal{U}}_{qm} = \hat{\mathcal{U}}_N(\Delta\omega_C, \tau_C)\, \hat{\mathcal{U}}_N(\Delta\omega_B, \tau_B)\, \hat{\mathcal{U}}_N(\Delta\omega_A, \tau_A). \tag{8.9}$$

This constitutes a **general four-parameter family of two-qubit gates**. In this protocol, the first two rotations (A and B) can be freely chosen. The final pulse (C) is then calculated to satisfy the unitarity condition described above: it must return the 2-QSS to its North Pole (its starting point).

Figure 8.6 provides a visual depiction of this general "ABC" protocol. The top row shows the 1-QSS, and the bottom row shows the 2-QSS. An arbitrary first pulse (A) and second pulse (B) are applied, taking the state vectors on complex paths from their starting poles. The final pulse (C) is then specifically calculated to return the $N = 2$ state vector (bottom row) to its initial "North Pole," satisfying the unitarity condition for the $|1, 1\rangle$ state.

As the figure illustrates, this *same* pulse (C) does *not* necessarily return the 1-QSS (top row) to its starting "South Pole". This differential evolution is the key: the 2-QSS returns to its starting pole (acquiring a phase γ) while the 1-QSS is left in a new, arbitrary superposition. This differential rotation *is* the non-trivial two-qubit gate, generating the 2×2 block in the final gate matrix Eq. (8.10)

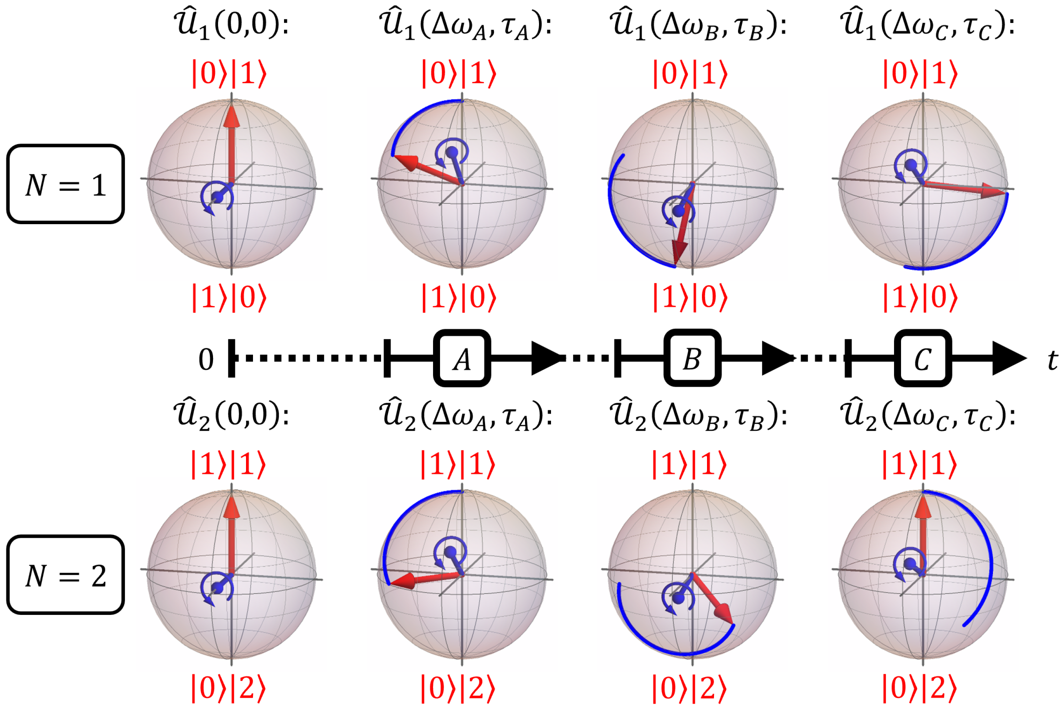

Figure 8.6: *ABC* composition on the *N*-*QSS* Bloch spheres (representing the q_t-m subsystem). Two arbitrary rotations A and B are followed by a computed C that returns the 2-*QSS* sphere (bottom row) to its initial "North Pole" (the $|1;1\rangle$ state) up to a phase. This same pulse C does not necessarily return the 1-*QSS* sphere (top row) to its starting "South Pole", resulting in a non-trivial operation on the 1-*QSS*.

This three-stage protocol can realize a general, block-diagonal two-qubit gate of the form:

$$\hat{\mathcal{U}}_{\text{gate}} = \begin{pmatrix} 1 & 0 & 0 & 0 \\ 0 & u_{11} & u_{12} & 0 \\ 0 & u_{21} & u_{22} & 0 \\ 0 & 0 & 0 & e^{i\gamma} \end{pmatrix} \tag{8.10}$$

where the 0-QSS ($|0,0\rangle$) is unchanged (identity), the 2-QSS ($|1,1\rangle$) acquires a phase γ, and the 1-QSS ($\{|0,1\rangle, |1,0\rangle\}$) undergoes a 2×2 unitary transformation $\hat{\mathcal{U}}_1$. This is a form of the fSim gate. While this protocol cannot realize a CNOT gate, it provides a powerful family of entangling operations.

The $CPhase$ Gate as a One-Parameter Specialization (ABA Protocol)

A universal set of gates does not require the full four-parameter arbitrary gate. We can realize the CPhase gate by imposing an *additional constraint* on our "ABC" three-step protocol.

The CPhase gate is defined by an operation that induces a tunable phase γ *only* on the $|1,1\rangle$ state, while acting as the identity on all other states ($|0,0\rangle$, $|0,1\rangle$, and $|1,0\rangle$). In practice, any physical protocol will impart *some* global phase to *all* subspaces. The phases acquired by the 1-QSS states (which map to $|0,1\rangle$ and $|1,0\rangle$) are trivial single-qubit phases. As we demonstrated in Section 8.3, the vacuum-R_Z protocol provides the exact tool to correct for these phases. Because that protocol allows us to apply any controllable $R_Z(\varphi)$ rotation, these single-qubit phases can be easily tracked and canceled out by applying corrective single-qubit R_Z rotations after the main protocol is complete.

The *entangling* part of the gate arises because the 2-QSS (mapping to $|1,1\rangle$), due to the N-dependent coupling (Eq. (8.4)), evolves *differently* and acquires a unique phase, $\phi_{N=2}$. The final, non-trivial entangling phase γ of the CPhase gate is the *leftover* relative phase on the $|1,1\rangle$ state *after* these single-qubit phases have been corrected for.

This logic can be expressed by showing the full unitary action on the qubit subspace. The raw three-stage protocol, $\hat{\mathcal{U}}_{\text{gate}}$, is diagonal and imparts a different phase on each computational basis state (we set the global phase $\phi_{00} = 0$):

$$\hat{\mathcal{U}}_{\text{gate}} = \begin{pmatrix} 1 & 0 & 0 & 0 \\ 0 & e^{i\phi_{01}} & 0 & 0 \\ 0 & 0 & e^{i\phi_{10}} & 0 \\ 0 & 0 & 0 & e^{i\phi_{11}} \end{pmatrix} \tag{8.11}$$

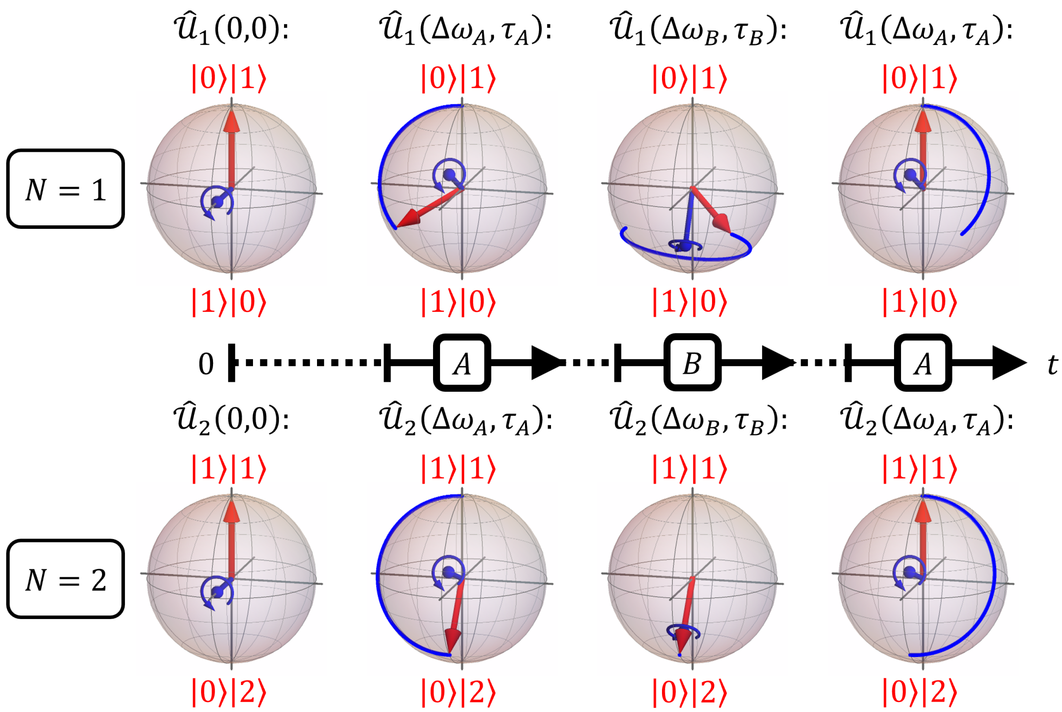

Figure 8.7: N-QSS Bloch-sphere depiction of the $CPhase$ gate protocol. This is a one-parameter limiting case of the more general four-parameter gate N-QSS Bloch-sphere depiction of the $CPhase$ gate protocol. This is a one-parameter limiting case of the more general four-parameter $\hat{\mathcal{U}}_{qm}$ such that $\hat{\mathcal{U}}_{CPhase}(\Delta\omega_A) = \hat{\mathcal{U}}_{qm}(\Delta\omega_A, \tau_A(\Delta\omega_A), \Delta\omega_B(\Delta\omega_A), \tau_B(\Delta\omega_A))$, where $\Delta\omega_A$ is the sole control parameter for the protocol, and the pulse sequence is constrained to return *both* the 1-QSS (top) and 2-QSS (bottom) to their starting poles, imposing an identity operation on the 1-QSS.

The phases ϕ_{01} and ϕ_{10} are the trivial, correctable single-qubit phases. We cancel them by applying a correction gate, $\hat{\mathcal{U}}_{\text{correct}}$, composed of the single-qubit R_Z operations we developed in Section 8.3. This correction is $\hat{\mathcal{U}}_{\text{correct}} = R_{Z,q_c}(-\phi_{10}) \otimes R_{Z,q_t}(-\phi_{01})$:

$$\hat{\mathcal{U}}_{\text{correct}} = \begin{pmatrix} 1 & 0 & 0 & 0 \\ 0 & e^{-i\phi_{01}} & 0 & 0 \\ 0 & 0 & e^{-i\phi_{10}} & 0 \\ 0 & 0 & 0 & e^{-i(\phi_{10}+\phi_{01})} \end{pmatrix} \tag{8.12}$$

The final, true CPhase gate is the product of the raw gate and this correction. The single-qubit phases cancel, leaving only the uncompensatable, relative phase on the $|1, 1\rangle$ state:

$$\hat{\mathcal{U}}_{\text{CPhase}} = \hat{\mathcal{U}}_{\text{correct}} \cdot \hat{\mathcal{U}}_{\text{gate}} = \begin{pmatrix} 1 & 0 & 0 & 0 \\ 0 & 1 & 0 & 0 \\ 0 & 0 & 1 & 0 \\ 0 & 0 & 0 & e^{i(\phi_{11}-\phi_{10}-\phi_{01})} \end{pmatrix} \tag{8.13}$$

This gives the entangling phase $\gamma = \phi_{11} - \phi_{10} - \phi_{01}$. To achieve this specialized gate, the "Interact" stage must satisfy *two* conditions simultaneously:

- An $R_Z(\gamma_{\text{net}})$ rotation on 2-QSS (returns to North Pole with a net phase, $\gamma_{\text{net}} \approx \phi_{11}$).
- An identity operation on 1-QSS (returns to South Pole with no net phase, $\phi_{10} \approx 0$).

This is possible precisely because of the N-QSS dependent coupling (Eq. (8.4)). The same pulse sequence rotates the 1-QSS and 2-QSS at different rates. We can therefore find a special set of pulses (e.g., a symmetric "ABA" sequence) that satisfies both conditions at once.

This reduces the general four-parameter $\hat{\mathcal{U}}_{qm}$ (Eq. (8.9)) to a one-parameter family of the more general four-parameter gate N-QSS Bloch-sphere depiction of the $CPhase$ gate protocol. This is a one-parameter limiting case of the more general four-parameter $\hat{\mathcal{U}}_{qm}$ such that

$$\hat{\mathcal{U}}_{CPhase}(\Delta\omega_A) = \hat{\mathcal{U}}_{qm}(\Delta\omega_A, \tau_A(\Delta\omega_A), \Delta\omega_B(\Delta\omega_A), \tau_B(\Delta\omega_A)), \tag{8.14}$$

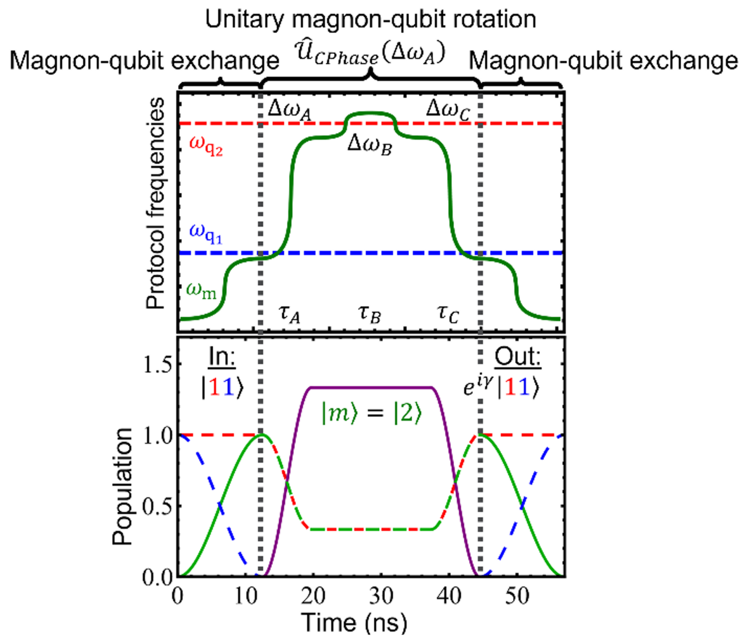

Figure 8.8: Schematic of the *CPhase* protocol applied to the $|1, 1\rangle$ state. Top: time-dependent detuning sequence across the three steps. Bottom: population evolution in qubit (dashed) and magnon (solid) modes; dotted lines indicate step boundaries. The protocol exchanges, interacts, and re-exchanges to end in a disentangled configuration.

where $\Delta\omega_A$ is the sole control parameter for the protocol. This results from the symmetric ABA protocol, where the durations τ_A and τ_C (of the *three-step* protocol) are fixed to perform the π-rotations, and the parameters for the *central* pulse (Step B) become dependent on the single control parameter, $\Delta\omega_A$.

This is shown schematically on the Bloch spheres in Fig. 8.7. This specialized "ABA" protocol is chosen such that the 1-QSS (top row) undergoes a complex path but returns to its starting South Pole (Identity), while the 2-QSS (bottom row) also returns to its starting North Pole, but acquires a net phase γ.

Figure 8.8 shows a simulation of this full $CPhase$ protocol applied to the $|1, 1\rangle$ state. The three-step "ABA" pulse profile is shown in the top panel. The bottom panel shows the populations. The final state is $e^{i\gamma}|1, 1\rangle$. Since this "ABA" sequence acts as the

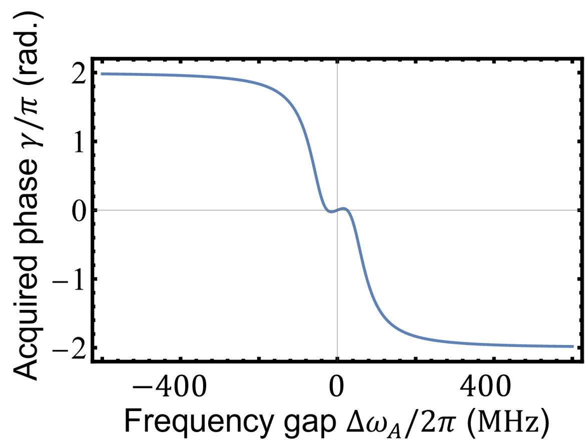

Figure 8.9: Phase acquired by the $CPhase$ gate versus the initial step detuning $\Delta\omega_A$ in the symmetric ABA realization. The single control parameter $\Delta\omega_A$ tunes the entangling phase continuously, while the subsequent step parameters are fixed by the unitarity/disentanglement condition.

identity on the $N = 1$ and $N = 0$ subspaces (up to correctable single-qubit phases), it is a true $CPhase$ gate. This gate is a **one-parameter family**: the desired entangling phase γ is continuously tunable simply by choosing the initial detuning $\Delta\omega_A$, as shown in Fig. 8.9.

8.5 Conclusion

We showed that magnons can be used as universal mediators in quantum information processing. Namely, we demonstrated the possibility of realizing a universal set of magnon-mediated quantum gates, including arbitrary single-qubit rotations and a two-qubit CPhase gate. We further showed this is a specialization of an arbitrary, four-parameter two-qubit gate, demonstrating a path toward quantum primacy-capable systems mediated by magnons. These gates are formed without any direct qubit-qubit interaction, using only dynamic control of the ancillary magnon mode. These results illuminate plausible paths for integrating magnonics into existing quantum technologies and may lead to the ability to build a reconfigurable magnonic-based quantum computer.

CHAPTER NINE

CONCLUSIONS

In this dissertation, we advance the theoretical framework of dynamic magnon-mediated interactions, moving from static concepts to concrete, simulated protocols. We first established a geometry-agnostic modeling framework (Chapter 3) for simulating time-dependent quantum systems. We then grounded our theory by applying it to a modular superconducting-circuit platform (Chapter 4) and exploring transmission line-mediated coupling between ferromagnetic resonators. This analysis in Chapter 4 was performed in direct collaboration with our experimental colleagues at Argonne National Laboratory, whose foundational work provided the experimental data used to validate our model.

With this robust theoretical foundation, we demonstrated how dynamically-tuned control of magnon resonance enables a suite of deterministic operations (Chapter 5), including linear-ramp transfer, parabolic SWAP/SPLIT operations, and an analytically solvable rectangular-pulse protocol that strategically suppresses dissipation. We extended this to the multi-excitation quantum regime by designing two temporal interferometers. Both the time-domain two-magnon interferometer (Chapter 6) and the temporal magnon-qubit Mach-Zehnder (Chapter 7) utilize pulsed control as a temporal beam splitter to generate correlated states and to enable a novel qubit-based probe of single-magnon decoherence.

Our central achievement is the construction of a universal set of magnon-mediated quantum gates (Chapter 8). We designed pulse sequences, simulated numerically, that realize arbitrary single-qubit rotations and two-qubit controlled-phase gates between noninteracting qubits. These results show that dynamically-tuned resonance control turns strong magnon coupling into a programmable resource, providing both a framework for universal control and a method for single-quanta diagnostics.

The immediate path forward is the experimental realization of the interferometers and foundational operations we have proposed. Our theoretical work provides a concrete route to programmable, heterogeneous quantum systems by using magnons as the active, dynamically-tuned interface that links otherwise static subsystems, translating strong, tunable coupling into scalable control.

REFERENCES

[1] S. Ganjam et al., "Surpassing millisecond coherence in on chip superconducting quantum memories by optimizing materials and circuit design," en, *Nature Communications*, vol. 15, no. 1, p. 3687, May 2024, Publisher: Nature Publishing Group, ISSN: 2041-1723. DOI: 10.1038/s41467-024-47857-6.

[2] M. Tuokkola et al., "Methods to achieve near-millisecond energy relaxation and dephasing times for a superconducting transmon qubit," en, *Nature Communications*, vol. 16, no. 1, p. 5421, Jul. 2025, Publisher: Nature Publishing Group, ISSN: 2041-1723. DOI: 10.1038/s41467-025-61126-0.

[3] Y. Wang et al., "Single-qubit quantum memory exceeding ten-minute coherence time," en, *Nature Photonics*, vol. 11, no. 10, pp. 646–650, Oct. 2017, Publisher: Nature Publishing Group, ISSN: 1749-4893. DOI: 10.1038/s41566-017-0007-1.

[4] F. Arute et al., "Quantum supremacy using a programmable superconducting processor," en, *Nature*, vol. 574, no. 7779, pp. 505–510, Oct. 2019, Publisher: Nature Publishing Group, ISSN: 1476-4687. DOI: 10.1038/s41586-019-1666-5.

[5] Google AI Quantum et al., "Demonstrating a Continuous Set of Two-Qubit Gates for Near-Term Quantum Algorithms," *Physical Review Letters*, vol. 125, no. 12, p. 120 504, Sep. 2020, Publisher: American Physical Society. DOI: 10.1103/PhysRevLett.125.120504.

[6] K. N. Smith, G. S. Ravi, J. M. Baker, and F. T. Chong, "Scaling Superconducting Quantum Computers with Chiplet Architectures," in *2022 55th IEEE/ACM International Symposium on Microarchitecture (MICRO)*, Oct. 2022, pp. 1092–1109. DOI: 10.1109/MICRO56248.2022.00078.

[7] M. Kjaergaard et al., "Superconducting Qubits: Current State of Play," en, *Annual Review of Condensed Matter Physics*, vol. 11, no. 1, pp. 369–395, Mar. 2020, ISSN: 1947-5454, 1947-5462. DOI: 10.1146/annurev-conmatphys-031119-050605.

[8] S. Bravyi, A. W. Cross, J. M. Gambetta, D. Maslov, P. Rall, and T. J. Yoder, "High-threshold and low-overhead fault-tolerant quantum memory," en, *Nature*, vol. 627, no. 8005, pp. 778–782, Mar. 2024, Publisher: Nature Publishing Group, ISSN: 1476-4687. DOI: 10.1038/s41586-024-07107-7.

[9] D. Castelvecchi, "IBM releases first-ever 1,000-qubit quantum chip," en, *Nature*, vol. 624, no. 7991, pp. 238–238, Dec. 2023, Bandiera_abtest: a Cg_type: News Publisher: Nature Publishing Group Subject_term: Mathematics and computing, Quantum physics. DOI: 10.1038/d41586-023-03854-1.

[10] J. Kim et al., "A Fault-Tolerant Million Qubit-Scale Distributed Quantum Computer," en, in *Proceedings of the 29th ACM International Conference on Architectural Support for Programming Languages and Operating Systems, Volume 2*, La Jolla CA USA: ACM, Apr. 2024, pp. 1–19, ISBN: 979-8-4007-0385-0. DOI: 10.1145/3620665.3640388.

[11] M. Mohseni et al., *How to Build a Quantum Supercomputer: Scaling from Hundreds to Millions of Qubits*, arXiv:2411.10406 [quant-ph], Jan. 2025. DOI: 10.48550/arXiv.2411.10406.

[12] H. D. Zeh, "On the interpretation of measurement in quantum theory," en, *Foundations of Physics*, vol. 1, no. 1, pp. 69–76, Mar. 1970, ISSN: 1572-9516. DOI: 10.1007/BF00708656.

[13] H. D. Zeh, "Toward a quantum theory of observation," en, *Foundations of Physics*, vol. 3, no. 1, pp. 109–116, Mar. 1973, ISSN: 1572-9516. DOI: 10.1007/BF00708603.

[14] Z.-L. Xiang, S. Ashhab, J. Q. You, and F. Nori, "Hybrid quantum circuits: Superconducting circuits interacting with other quantum systems," *Reviews of Modern Physics*, vol. 85, no. 2, pp. 623–653, Apr. 2013, Publisher: American Physical Society. DOI: 10.1103/RevModPhys.85.623.

[15] A. A. Clerk, K. W. Lehnert, P. Bertet, J. R. Petta, and Y. Nakamura, "Hybrid quantum systems with circuit quantum electrodynamics," en, *Nature Physics*, vol. 16, no. 3, pp. 257–267, Mar. 2020, Publisher: Nature Publishing Group, ISSN: 1745-2481. DOI: 10.1038/s41567-020-0797-9.

[16] G. Kurizki et al., "Quantum technologies with hybrid systems," *Proceedings of the National Academy of Sciences*, vol. 112, no. 13, pp. 3866–3873, Mar. 2015, Publisher: Proceedings of the National Academy of Sciences. DOI: 10.1073/pnas.1419326112.

[17] A. Blais, R.-S. Huang, A. Wallraff, S. M. Girvin, and R. J. Schoelkopf, "Cavity quantum electrodynamics for superconducting electrical circuits: An architecture for quantum computation," *Physical Review A*, vol. 69, no. 6, p. 062 320, Jun. 2004, Publisher: American Physical Society. DOI: 10.1103/PhysRevA.69.062320.

[18] A. Wallraff et al., "Strong coupling of a single photon to a superconducting qubit using circuit quantum electrodynamics," en, *Nature*, vol. 431, no. 7005, pp. 162–167, Sep. 2004, Publisher: Nature Publishing Group, ISSN: 1476-4687. DOI: 10.1038/nature02851.

[19] J. E. Moore et al., "Basic Energy Sciences Roundtable: Opportunities for Quantum Computing in Chemical and Materials Sciences," English, USDOE Office of Science (SC) (United States), Tech. Rep., Nov. 2017. DOI: 10.2172/1616253.

[20] L. Fan et al., "Superconducting cavity electro-optics: A platform for coherent photon conversion between superconducting and photonic circuits," *Science Advances*, vol. 4, no. 8, eaar4994, Aug. 2018, Publisher: American Association for the Advancement of Science. DOI: 10.1126/sciadv.aar4994.

[21] A. Imamoğlu, "Cavity QED Based on Collective Magnetic Dipole Coupling: Spin Ensembles as Hybrid Two-Level Systems," *Physical Review Letters*, vol. 102, no. 8, p. 083 602, Feb. 2009, Publisher: American Physical Society. DOI: 10.1103/PhysRevLett.102.083602.

[22] J. H. Wesenberg et al., "Quantum Computing with an Electron Spin Ensemble," *Physical Review Letters*, vol. 103, no. 7, p. 070 502, Aug. 2009, Publisher: American Physical Society. DOI: 10.1103/PhysRevLett.103.070502.
[23] D. I. Schuster et al., "High-Cooperativity Coupling of Electron-Spin Ensembles to Superconducting Cavities," *Physical Review Letters*, vol. 105, no. 14, p. 140 501, Sep. 2010, Publisher: American Physical Society. DOI: 10.1103/PhysRevLett.105.140501.
[24] D. Lachance-Quirion, Y. Tabuchi, A. Gloppe, K. Usami, and Y. Nakamura, "Hybrid quantum systems based on magnonics," en, *Applied Physics Express*, vol. 12, no. 7, p. 070 101, Jun. 2019, Publisher: IOP Publishing, ISSN: 1882-0786. DOI: 10.7567/1882-0786/ab248d.
[25] D. Zhu et al., "A scalable multi-photon coincidence detector based on superconducting nanowires," en, *Nature Nanotechnology*, vol. 13, no. 7, pp. 596–601, Jul. 2018, Publisher: Nature Publishing Group, ISSN: 1748-3395. DOI: 10.1038/s41565-018-0160-9.
[26] Y. Chu et al., "Quantum acoustics with superconducting qubits," *Science*, vol. 358, no. 6360, pp. 199–202, Oct. 2017, Publisher: American Association for the Advancement of Science. DOI: 10.1126/science.aao1511.
[27] K. J. Satzinger et al., "Quantum control of surface acoustic-wave phonons," en, *Nature*, vol. 563, no. 7733, pp. 661–665, Nov. 2018, Publisher: Nature Publishing Group, ISSN: 1476-4687. DOI: 10.1038/s41586-018-0719-5.
[28] S. J. Whiteley et al., "Spin–phonon interactions in silicon carbide addressed by Gaussian acoustics," en, *Nature Physics*, vol. 15, no. 5, pp. 490–495, May 2019, Publisher: Nature Publishing Group, ISSN: 1745-2481. DOI: 10.1038/s41567-019-0420-0.
[29] Y. Kubo et al., "Strong Coupling of a Spin Ensemble to a Superconducting Resonator," *Physical Review Letters*, vol. 105, no. 14, p. 140 502, Sep. 2010, Publisher: American Physical Society. DOI: 10.1103/PhysRevLett.105.140502.
[30] H. Huebl et al., "High Cooperativity in Coupled Microwave Resonator Ferrimagnetic Insulator Hybrids," *Physical Review Letters*, vol. 111, no. 12, p. 127 003, Sep. 2013, Publisher: American Physical Society. DOI: 10.1103/PhysRevLett.111.127003.
[31] Y. Tabuchi, S. Ishino, T. Ishikawa, R. Yamazaki, K. Usami, and Y. Nakamura, "Hybridizing Ferromagnetic Magnons and Microwave Photons in the Quantum Limit," *Physical Review Letters*, vol. 113, no. 8, p. 083 603, Aug. 2014, Publisher: American Physical Society. DOI: 10.1103/PhysRevLett.113.083603.
[32] X. Zhang, C.-L. Zou, L. Jiang, and H. X. Tang, "Strongly Coupled Magnons and Cavity Microwave Photons," *Physical Review Letters*, vol. 113, no. 15, p. 156 401, Oct. 2014, Publisher: American Physical Society. DOI: 10.1103/PhysRevLett.113.156401.

[33] Y. Tabuchi et al., “Coherent coupling between a ferromagnetic magnon and a superconducting qubit,” *Science*, vol. 349, no. 6246, pp. 405–408, Jul. 2015, Publisher: American Association for the Advancement of Science. DOI: 10.1126/science.aaa3693.

[34] Y. Li et al., “Strong Coupling between Magnons and Microwave Photons in On-Chip Ferromagnet-Superconductor Thin-Film Devices,” *Physical Review Letters*, vol. 123, no. 10, p. 107 701, Sep. 2019, Publisher: American Physical Society. DOI: 10.1103/PhysRevLett.123.107701.

[35] J. T. Hou and L. Liu, “Strong Coupling between Microwave Photons and Nanomagnet Magnons,” *Physical Review Letters*, vol. 123, no. 10, p. 107 702, Sep. 2019, Publisher: American Physical Society. DOI: 10.1103/PhysRevLett.123.107702.

[36] A. G. Gurevich and G. A. Melkov, *Magnetization Oscillations and Waves*, en. London: CRC Press, Sep. 1996, ISBN: 978-0-8493-9460-7. DOI: 10.1201/9780138748487.

[37] B. A. Kalinikos and A. N. Slavin, “Theory of dipole-exchange spin wave spectrum for ferromagnetic films with mixed exchange boundary conditions,” *Journal of Physics C: Solid State Physics*, vol. 19, no. 35, pp. 7013–7033, Dec. 1986, ISSN: 0022-3719. DOI: 10.1088/0022-3719/19/35/014.

[38] A. V. Chumak, V. I. Vasyuchka, A. A. Serga, and B. Hillebrands, “Magnon spintronics,” en, *Nature Physics*, vol. 11, no. 6, pp. 453–461, Jun. 2015, ISSN: 1745-2473, 1745-2481. DOI: 10.1038/nphys3347.

[39] Y. Li, W. Zhang, V. Tyberkevych, W.-K. Kwok, A. Hoffmann, and V. Novosad, “Hybrid magnonics: Physics, circuits, and applications for coherent information processing,” *Journal of Applied Physics*, vol. 128, no. 13, p. 130 902, Oct. 2020, ISSN: 0021-8979. DOI: 10.1063/5.0020277.

[40] D. D. Awschalom et al., “Quantum Engineering With Hybrid Magnonic Systems and Materials (Invited Paper),” *IEEE Transactions on Quantum Engineering*, vol. 2, pp. 1–36, 2021, Conference Name: IEEE Transactions on Quantum Engineering, ISSN: 2689-1808. DOI: 10.1109/TQE.2021.3057799.

[41] J. Xu, C. Zhong, X. Han, D. Jin, L. Jiang, and X. Zhang, “Coherent Gate Operations in Hybrid Magnonics,” *Physical Review Letters*, vol. 126, no. 20, p. 207 202, May 2021, Publisher: American Physical Society. DOI: 10.1103/PhysRevLett.126.207202.

[42] D. Lachance-Quirion et al., “Resolving quanta of collective spin excitations in a millimeter-sized ferromagnet,” *Science Advances*, vol. 3, no. 7, e1603150, Jul. 2017, Publisher: American Association for the Advancement of Science. DOI: 10.1126/sciadv.1603150.

[43] D. Lachance-Quirion, S. P. Wolski, Y. Tabuchi, S. Kono, K. Usami, and Y. Nakamura, “Entanglement-based single-shot detection of a single magnon with a superconducting qubit,” *Science*, vol. 367, no. 6476, pp. 425–428, Jan. 2020,

Publisher: American Association for the Advancement of Science. DOI: 10.1126/science.aaz9236.
[44] C. Trevillian and V. Tyberkevych, “Magnon mediated coherent information transfer between superconducting resonators,” in *Digests of the IEEE International Magnetics Conference 2020 (INTERMAG 2020)*, FE-09, Montreal, Quebec, Canada: IEEE Magnetics Society, 2020.
[45] C. Trevillian and V. Tyberkevych, “Magnon mediated coherent information manipulation and processing,” in *Abstracts of the 65th Annual Conference on Magnetism and Magnetic Materials (MMM 2020)*, Q2-07, Virtual: IEEE Magnetics Society, 2020.
[46] C. Trevillian and V. Tyberkevych, “Magnon mediated coherent quantum information operations,” in *2020 IEEE Around-the-Clock Around-the-Globe Magnetics Conference (AtC-AtG 2020)*, Virtual, Earth: IEEE Magnetics Society, 2020.
[47] C. Trevillian and V. Tyberkevych, “Unitary magnon-mediated operations for quantum computing,” in *2020 IEEE 10th International Conference on “Nanomaterials: Applications & Properties” (NAP-2020)*, Sumy, Ukraine: IEEE, 2020.
[48] C. Trevillian and V. Tyberkevych, “Unitary quantum information operations mediated by magnons,” in *2nd Joint Annual Meeting of the IEEE Magnetics Society and Nanotechnology Council Chicago Chapters*, Virtual: IEEE, 2020.
[49] C. Trevillian and V. Tyberkevych, “Analytical model for unitary magnon-mediated quantum gates in hybrid magnon-photon systems,” in *Digests of the IEEE International Magnetics Conference 2021 (INTERMAG 2021)*, EC-09, Lyon, France: IEEE Magnetics Society, 2021.
[50] C. Trevillian and V. Tyberkevych, “Unitary magnon-mediated operations for quantum computing,” in *APS March Meeting Abstracts 2021*, R38.00002, Virtual: APS, 2021.
[51] C. Trevillian and V. Tyberkevych, “Time domain two-magnon interference,” in *2021 IEEE Around-the-Clock Around-the-Globe Magnetics Conference (AtC-AtG 2021)*, Virtual, Earth: IEEE Magnetics Society, 2021.
[52] C. Trevillian and V. Tyberkevych, “Magnon-mediated quantum information processing in weakly-coupled hybrid magnon-photon systems,” in *Abstracts of the Sixth International Conference for Young Quantum Information Scientists (YQIS 6)*, Virtual, 2021.
[53] C. Trevillian and V. Tyberkevych, “Increasing fidelity of magnon-mediated quantum gates by off-resonance coupling,” in *2021 IEEE 11th International Conference on “Nanomaterials: Applications & Properties” (NAP-2021)*, Odesa, Ukraine: IEEE, 2021.
[54] C. Trevillian and V. Tyberkevych, “Generation of entanglement by two-magnon interference,” in *Abstracts of the 15th IEEE Joint Magnetism and Magnetic*

Materials - International Magnetics Conference (Joint MMM-INTERMAG 2022), HOJ-02, New Orleans, LA, USA: IEEE Magnetics Society, 2022.

[55] C. Trevillian and V. Tyberkevych, “Entanglement manipulation with a tunable magnonic beamsplitter,” in *APS March Meeting Abstracts 2022*, S52.00014, Chicago, IL, USA: APS, 2022.

[56] C. Trevillian and V. Tyberkevych, “Controllably entangled magnon states via two-magnon interference,” in *7th International Conference on Magnonics (Magnonics 2022)*, B2-2, Oxnard, CA, USA, 2022.

[57] C. Trevillian and V. Tyberkevych, “Interferometry of single magnon decoherence mechanisms,” in *2022 IEEE Around-the-Clock Around-the-Globe Magnetics Conference (AtC-AtG 2022)*, Virtual, Earth: IEEE Magnetics Society, 2022.

[58] C. Trevillian and V. Tyberkevych, “Measurement scheme for single magnon decoherence,” in *Abstracts of the 67th Annual Conference on Magnetism and Magnetic Materials (MMM 2022)*, CE-06 (GOC-10), Minneapolis, MN, USA: IEEE Magnetics Society, 2022.

[59] C. Trevillian and V. Tyberkevych, “Temporal-domain magnonic mach-zehnder interferometer,” in *APS March Meeting Abstracts 2023*, Q57.00008, Las Vegas, NV, USA: APS, 2023.

[60] C. Trevillian and V. Tyberkevych, “Temporal magnon-qubit mach-zehnder interferometry,” in *APS Eastern Great Lakes Section Spring Meeting Abstracts 2023*, Rochester, MI, USA: APS, 2023.

[61] C. Trevillian and V. Tyberkevych, “Universal set of magnon-mediated quantum gates,” in *3rd IEEE Magnetic Frontiers: Quantum Technologies Conference (Magnetic Frontiers 2023)*, Orlando, FL, USA: IEEE Magnetics Society, 2023.

[62] C. Trevillian and V. Tyberkevych, “Universal set of magnon-mediated quantum gates,” in *Digests of the IEEE International Magnetic Conference 2023 (INTERMAG 2023)*, GH-07 (SOD-09), Sendai, Japan: IEEE Magnetics Society, 2023.

[63] C. Trevillian and V. Tyberkevych, “Temporal magnon-qubit mach-zehnder interferometry,” in *2023 IEEE Magnetics Society Summer School*, Bari, Italy: IEEE Magnetics Society, 2023.

[64] C. Trevillian and V. Tyberkevych, “Universal set of magnon-mediated quantum gates,” in *8th International Conference on Magnonics (Magnonics 2023)*, P2-PB50, Le Touquet-Paris-Plage, France, 2023.

[65] C. Trevillian and V. Tyberkevych, “Two-qubit magnon-mediated quantum gates,” in *Abstracts of the 68th Annual Conference on Magnetism and Magnetic Materials (MMM 2023)*, ED-10, 2023.

[66] C. Trevillian and V. Tyberkevych, “Arbitrary two-qubit magnon-mediated quantum gates,” in *Digests of the IEEE International Magnetic Conference 2024 (INTERMAG 2024)*, DB-09, Rio de Janeiro, Brazil, 2024.

[67] C. Trevillian and V. Tyberkevych, "Magnon-mediated quantum interferometry," in *Abstracts of the 8th International Conference on Microwave Magnetics (ICMM 2024)*, Rochester, MI, USA, 2024.
[68] C. Trevillian and V. Tyberkevych, "Magnon-mediated quantum computing," in *Abstracts of the 8th International Conference on Microwave Magnetics (ICMM 2024)*, Rochester, MI, USA, 2024.
[69] C. Trevillian and V. Tyberkevych, "Magnon-mediated quantum computing," in *6th Joint Annual Meeting of the IEEE Magnetics Society and Nanotechnology Council, Chicago and Southeastern Michigan Chapters*, Chicago, IL, USA: IEEE, 2024.
[70] A. V. Chumak et al., "Advances in Magnetics Roadmap on Spin-Wave Computing," *IEEE Transactions on Magnetics*, vol. 58, no. 6, pp. 1–72, Jun. 2022, Conference Name: IEEE Transactions on Magnetics, ISSN: 1941-0069. DOI: 10.1109/TMAG.2022.3149664.
[71] Y. Li et al., "Coherent Coupling of Two Remote Magnonic Resonators Mediated by Superconducting Circuits," en, *Physical Review Letters*, vol. 128, no. 4, p. 047 701, Jan. 2022, ISSN: 0031-9007, 1079-7114. DOI: 10.1103/PhysRevLett.128.047701.
[72] M. Song et al., *Programmable Real-Time Magnon Interference in Two Remotely Coupled Magnonic Resonators*, arXiv:2309.04289 [cond-mat], Sep. 2023. DOI: 10.48550/arXiv.2309.04289.
[73] M. Song et al., "Single-shot magnon interference in a magnon-superconducting-resonator hybrid circuit," *Nature Communications*, vol. 16, no. 1, p. 3649, Apr. 17, 2025, ISSN: 2041-1723. DOI: 10.1038/s41467-025-58482-2.
[74] F. Bloch, "Zur Theorie des Ferromagnetismus," de, *Zeitschrift für Physik*, vol. 61, no. 3, pp. 206–219, Mar. 1930, ISSN: 0044-3328. DOI: 10.1007/BF01339661.
[75] T. Holstein, "Field Dependence of the Intrinsic Domain Magnetization of a Ferromagnet," *Physical Review*, vol. 58, no. 12, pp. 1098–1113, 1940. DOI: 10.1103/PhysRev.58.1098.
[76] F. J. Dyson, "General Theory of Spin-Wave Interactions," en, *Physical Review*, vol. 102, no. 5, pp. 1217–1230, Jun. 1956, ISSN: 0031-899X. DOI: 10.1103/PhysRev.102.1217.
[77] C. Herring and C. Kittel, "On the Theory of Spin Waves in Ferromagnetic Media," en, *Physical Review*, vol. 81, no. 5, pp. 869–880, Mar. 1951, ISSN: 0031-899X. DOI: 10.1103/PhysRev.81.869.
[78] C. Kittel, "On the Theory of Ferromagnetic Resonance Absorption," *Physical Review*, vol. 73, no. 2, pp. 155–161, Jan. 1948, Publisher: American Physical Society. DOI: 10.1103/PhysRev.73.155.
[79] C. Kittel, "Excitation of Spin Waves in a Ferromagnet by a Uniform rf Field," *Physical Review*, vol. 110, no. 6, pp. 1295–1297, Jun. 1958, Publisher: American Physical Society. DOI: 10.1103/PhysRev.110.1295.

[80] L. R. Walker, “Magnetostatic Modes in Ferromagnetic Resonance,” *Physical Review*, vol. 105, no. 2, pp. 390–399, 1957. DOI: 10.1103/PhysRev.105.390.

[81] R. W. Damon and J. R. Eshbach, “Magnetostatic modes of a ferromagnet slab,” *Journal of Physics and Chemistry of Solids*, vol. 19, no. 3, pp. 308–320, May 1961, ISSN: 0022-3697. DOI: 10.1016/0022-3697(61)90041-5.

[82] S. O. Demokritov, B. Hillebrands, and A. N. Slavin, “Brillouin light scattering studies of confined spin waves: Linear and nonlinear confinement,” *Physics Reports*, vol. 348, no. 6, pp. 441–489, Jul. 2001, ISSN: 0370-1573. DOI: 10.1016/S0370-1573(00)00116-2.

[83] A. A. Serga, T. Neumann, A. V. Chumak, and B. Hillebrands, “Generation of spin-wave pulse trains by current-controlled magnetic mirrors,” *Applied Physics Letters*, vol. 94, no. 11, p. 112 501, Mar. 2009, ISSN: 0003-6951. DOI: 10.1063/1.3098407.

[84] L. J. Cornelissen, J. Liu, R. A. Duine, J. B. Youssef, and B. J. van Wees, “Long distance transport of magnon spin information in a magnetic insulator at room temperature,” *Nature Physics*, vol. 11, no. 12, pp. 1022–1026, Dec. 2015, arXiv:1505.06325 [cond-mat], ISSN: 1745-2473, 1745-2481. DOI: 10.1038/nphys3465.

[85] V. Cherepanov, I. Kolokolov, and V. L’vov, “The saga of YIG: Spectra, thermodynamics, interaction and relaxation of magnons in a complex magnet,” *Physics Reports*, vol. 229, no. 3, pp. 81–144, Jul. 1993, ISSN: 0370-1573. DOI: 10.1016/0370-1573(93)90107-O.

[86] A. A. Serga, A. V. Chumak, and B. Hillebrands, “YIG magnonics,” *Journal of Physics D: Applied Physics*, vol. 43, no. 26, p. 264 002, Jul. 2010, ISSN: 0022-3727, 1361-6463. DOI: 10.1088/0022-3727/43/26/264002.

[87] P. Pirro, V. I. Vasyuchka, A. A. Serga, and B. Hillebrands, “Advances in coherent magnonics,” en, *Nature Reviews Materials*, vol. 6, no. 12, pp. 1114–1135, Dec. 2021, Publisher: Nature Publishing Group, ISSN: 2058-8437. DOI: 10.1038/s41578-021-00332-w.

[88] A. V. Chumak and H. Schultheiss, “Magnonics: Spin waves connecting charges, spins and photons,” *Journal of Physics D: Applied Physics*, vol. 50, no. 30, p. 300 201, Aug. 2017, ISSN: 0022-3727, 1361-6463. DOI: 10.1088/1361-6463/aa7715.

[89] B. Schumacher, “Quantum coding,” en, *Physical Review A*, vol. 51, no. 4, pp. 2738–2747, Apr. 1995, ISSN: 1050-2947, 1094-1622. DOI: 10.1103/PhysRevA.51.2738.

[90] R. P. Feynman, “Simulating physics with computers,” en, *International Journal of Theoretical Physics*, vol. 21, no. 6, pp. 467–488, Jun. 1982, ISSN: 1572-9575. DOI: 10.1007/BF02650179.

[91] D. Deutsch, “Quantum theory, the Church–Turing principle and the universal quantum computer,” en, *Proceedings of the Royal Society of London. A.*

Mathematical and Physical Sciences, vol. 400, no. 1818, pp. 97–117, Jul. 1985, ISSN: 0080-4630. DOI: 10.1098/rspa.1985.0070.
[92] M. A. Nielsen and I. L. Chuang, *Quantum Computation and Quantum Information: 10th Anniversary Edition*, en. Cambridge University Press, Dec. 2010, ISBN: 978-1-139-49548-6.
[93] R. P. Feynman, "Quantum mechanical computers," en, *Foundations of Physics*, vol. 16, no. 6, pp. 507–531, Jun. 1986, ISSN: 1572-9516. DOI: 10.1007/BF01886518.
[94] P. Jurcevic et al., "Demonstration of quantum volume 64 on a superconducting quantum computing system," en, *Quantum Science and Technology*, vol. 6, no. 2, p. 025 020, Mar. 2021, Publisher: IOP Publishing, ISSN: 2058-9565. DOI: 10.1088/2058-9565/abe519.
[95] Y. Kim et al., "Evidence for the utility of quantum computing before fault tolerance," en, *Nature*, vol. 618, no. 7965, pp. 500–505, Jun. 2023, Publisher: Nature Publishing Group, ISSN: 1476-4687. DOI: 10.1038/s41586-023-06096-3.
[96] J. I. Cirac, "Quantum Computations with Cold Trapped Ions," *Physical Review Letters*, vol. 74, no. 20, pp. 4091–4094, 1995. DOI: 10.1103/PhysRevLett.74.4091.
[97] C. Monroe and J. Kim, "Scaling the Ion Trap Quantum Processor," *Science*, vol. 339, no. 6124, pp. 1164–1169, Mar. 2013, Publisher: American Association for the Advancement of Science. DOI: 10.1126/science.1231298.
[98] D. Loss, "Quantum computation with quantum dots," *Physical Review A*, vol. 57, no. 1, pp. 120–126, 1998. DOI: 10.1103/PhysRevA.57.120.
[99] D. M. Zajac et al., "Resonantly driven CNOT gate for electron spins," *Science*, vol. 359, no. 6374, pp. 439–442, Jan. 2018, Publisher: American Association for the Advancement of Science. DOI: 10.1126/science.aao5965.
[100] I. Bloch, J. Dalibard, and S. Nascimbène, "Quantum simulations with ultracold quantum gases," en, *Nature Physics*, vol. 8, no. 4, pp. 267–276, Apr. 2012, Publisher: Nature Publishing Group, ISSN: 1745-2481. DOI: 10.1038/nphys2259.
[101] M. Saffman, "Quantum computing with atomic qubits and Rydberg interactions: Progress and challenges," en, *Journal of Physics B: Atomic, Molecular and Optical Physics*, vol. 49, no. 20, p. 202 001, Oct. 2016, Publisher: IOP Publishing, ISSN: 0953-4075. DOI: 10.1088/0953-4075/49/20/202001.
[102] E. Knill, R. Laflamme, and G. J. Milburn, "A scheme for efficient quantum computation with linear optics," en, *Nature*, vol. 409, no. 6816, pp. 46–52, Jan. 2001, Publisher: Nature Publishing Group, ISSN: 1476-4687. DOI: 10.1038/35051009.
[103] Y. Wang et al., "Efficient quantum memory for single-photon polarization qubits," en, *Nature Photonics*, vol. 13, no. 5, pp. 346–351, May 2019, Publisher: Nature Publishing Group, ISSN: 1749-4893. DOI: 10.1038/s41566-019-0368-8.

[104] P. W. Shor, “Scheme for reducing decoherence in quantum computer memory,” *Physical Review A*, vol. 52, no. 4, R2493–R2496, 1995. DOI: 10.1103/PhysRevA.52.R2493.
[105] A. M. Steane, “Error Correcting Codes in Quantum Theory,” *Physical Review Letters*, vol. 77, no. 5, pp. 793–797, 1996. DOI: 10.1103/PhysRevLett.77.793.
[106] A. M. Steane, “Simple quantum error-correcting codes,” *Physical Review A*, vol. 54, no. 6, pp. 4741–4751, 1996. DOI: 10.1103/PhysRevA.54.4741.
[107] B. M. Terhal, “Quantum error correction for quantum memories,” *Reviews of Modern Physics*, vol. 87, no. 2, pp. 307–346, 2015. DOI: 10.1103/RevModPhys.87.307.
[108] J. M. Martinis, “Decoherence in Josephson Qubits from Dielectric Loss,” *Physical Review Letters*, vol. 95, no. 21, 2005. DOI: 10.1103/PhysRevLett.95.210503.
[109] F. Bloch, “Nuclear Induction,” *Physical Review*, vol. 70, no. 7-8, pp. 460–474, 1946. DOI: 10.1103/PhysRev.70.460.
[110] R. P. Feynman, F. L. Vernon Jr., and R. W. Hellwarth, “Geometrical Representation of the Schrödinger Equation for Solving Maser Problems,” *Journal of Applied Physics*, vol. 28, no. 1, pp. 49–52, Jan. 1957, ISSN: 0021-8979. DOI: 10.1063/1.1722572.
[111] Y. Nakamura, Y. A. Pashkin, and J. S. Tsai, “Coherent control of macroscopic quantum states in a single-Cooper-pair box,” en, *Nature*, vol. 398, no. 6730, pp. 786–788, Apr. 1999, Publisher: Nature Publishing Group, ISSN: 1476-4687. DOI: 10.1038/19718.
[112] J. Koch et al., “Charge-insensitive qubit design derived from the Cooper pair box,” *Physical Review A*, vol. 76, no. 4, p. 042 319, Oct. 2007, Publisher: American Physical Society. DOI: 10.1103/PhysRevA.76.042319.
[113] H. Häffner, C. F. Roos, and R. Blatt, “Quantum computing with trapped ions,” *Physics Reports*, vol. 469, no. 4, pp. 155–203, Dec. 2008, ISSN: 0370-1573. DOI: 10.1016/j.physrep.2008.09.003.
[114] R. Blatt and D. Wineland, “Entangled states of trapped atomic ions,” en, *Nature*, vol. 453, no. 7198, pp. 1008–1015, Jun. 2008, Publisher: Nature Publishing Group, ISSN: 1476-4687. DOI: 10.1038/nature07125.
[115] F. A. Zwanenburg, “Silicon quantum electronics,” *Reviews of Modern Physics*, vol. 85, no. 3, pp. 961–1019, 2013. DOI: 10.1103/RevModPhys.85.961.
[116] J. L. O’Brien, “Optical Quantum Computing,” *Science*, vol. 318, no. 5856, pp. 1567–1570, Dec. 2007, Publisher: American Association for the Advancement of Science. DOI: 10.1126/science.1142892.
[117] C. Gonzalez, “Cloud based QC with Amazon Braket,” en, *Digitale Welt*, vol. 5, no. 2, pp. 14–17, Apr. 2021, ISSN: 2569-1996. DOI: 10.1007/s42354-021-0330-z.
[118] J. E. Bourassa et al., “Blueprint for a Scalable Photonic Fault-Tolerant Quantum Computer,” en-GB, *Quantum*, vol. 5, p. 392, Feb. 2021, Publisher: Verein zur

Förderung des Open Access Publizierens in den Quantenwissenschaften. DOI: 10.22331/q-2021-02-04-392.
[119] T. Rudolph, “Why I am optimistic about the silicon-photonic route to quantum computing,” *APL Photonics*, vol. 2, no. 3, p. 030 901, Mar. 2017, ISSN: 2378-0967. DOI: 10.1063/1.4976737.
[120] L. Bai, M. Harder, Y. P. Chen, X. Fan, J. Q. Xiao, and C.-M. Hu, “Spin Pumping in Electrodynamically Coupled Magnon-Photon Systems,” *Physical Review Letters*, vol. 114, no. 22, p. 227 201, Jun. 2015, Publisher: American Physical Society. DOI: 10.1103/PhysRevLett.114.227201.
[121] Y. Tabuchi et al., “Quantum magnonics: The magnon meets the superconducting qubit,” fr, *Comptes Rendus. Physique*, vol. 17, no. 7, pp. 729–739, 2016, ISSN: 1878-1535. DOI: 10.1016/j.crhy.2016.07.009.
[122] J. Majer et al., “Coupling superconducting qubits via a cavity bus,” en, *Nature*, vol. 449, no. 7161, pp. 443–447, Sep. 2007, ISSN: 0028-0836, 1476-4687. DOI: 10.1038/nature06184.
[123] M. Boissonneault, “Dispersive regime of circuit QED: Photon-dependent qubit dephasing and relaxation rates,” *Physical Review A*, vol. 79, no. 1, 2009. DOI: 10.1103/PhysRevA.79.013819.
[124] A. A. Clerk, M. H. Devoret, S. M. Girvin, F. Marquardt, and R. J. Schoelkopf, “Introduction to Quantum Noise, Measurement and Amplification,” *Reviews of Modern Physics*, vol. 82, no. 2, pp. 1155–1208, Apr. 2010, arXiv:0810.4729 [cond-mat], ISSN: 0034-6861, 1539-0756. DOI: 10.1103/RevModPhys.82.1155.
[125] M. Kounalakis, C. Dickel, A. Bruno, N. K. Langford, and G. A. Steele, “Tuneable hopping and nonlinear cross-Kerr interactions in a high-coherence superconducting circuit,” en, *npj Quantum Information*, vol. 4, no. 1, p. 38, Aug. 2018, Publisher: Nature Publishing Group, ISSN: 2056-6387. DOI: 10.1038/s41534-018-0088-9.
[126] M. Harder et al., “Level Attraction Due to Dissipative Magnon-Photon Coupling,” *Physical Review Letters*, vol. 121, no. 13, p. 137 203, Sep. 2018, Publisher: American Physical Society. DOI: 10.1103/PhysRevLett.121.137203.
[127] V. L. Grigoryan, “Cavity-mediated dissipative spin-spin coupling,” *Physical Review B*, vol. 100, no. 1, 2019. DOI: 10.1103/PhysRevB.100.014415.
[128] X. Xu, “Cavity quantum electrodynamics with single quantum dots and photonic crystal cavities,” en, in *International Photonics and OptoElectronics Meeting 2019 (OFDA, OEDI, ISST, PE, LST, TSA)*, Wuhan: OSA, 2019, OW3D.1, ISBN: 978-1-943580-72-9. DOI: 10.1364/OEDI.2019.OW3D.1.
[129] Y.-P. Wang and C.-M. Hu, “Dissipative couplings in cavity magnonics,” *Journal of Applied Physics*, vol. 127, no. 13, p. 130 901, Apr. 2020, ISSN: 0021-8979. DOI: 10.1063/1.5144202.
[130] I. Boventer, “Control of the coupling strength and linewidth of a cavity magnon-polariton,” *Physical Review Research*, vol. 2, no. 1, 2020. DOI: 10.1103/PhysRevResearch.2.013154.

[131] B. Bhoi, “Abnormal anticrossing effect in photon-magnon coupling,” *Physical Review B*, vol. 99, no. 13, 2019. DOI: 10.1103/PhysRevB.99.134426.
[132] Y. Tserkovnyak, “Exceptional points in dissipatively coupled spin dynamics,” *Physical Review Research*, vol. 2, no. 1, 2020. DOI: 10.1103/PhysRevResearch.2.013031.
[133] B. Yao et al., “The microscopic origin of magnon-photon level attraction by traveling waves: Theory and experiment,” en, *Physical Review B*, vol. 100, no. 21, p. 214 426, Dec. 2019, ISSN: 2469-9950, 2469-9969. DOI: 10.1103/PhysRevB.100.214426.
[134] J. W. Rao, “Interactions between a magnon mode and a cavity photon mode mediated by traveling photons,” *Physical Review B*, vol. 101, no. 6, 2020. DOI: 10.1103/PhysRevB.101.064404.
[135] X. Zhang, C.-L. Zou, N. Zhu, F. Marquardt, L. Jiang, and H. X. Tang, “Magnon dark modes and gradient memory,” en, *Nature Communications*, vol. 6, no. 1, p. 8914, Nov. 2015, ISSN: 2041-1723. DOI: 10.1038/ncomms9914.
[136] N. J. Lambert, J. A. Haigh, S. Langenfeld, A. C. Doherty, and A. J. Ferguson, “Cavity-mediated coherent coupling of magnetic moments,” *Physical Review A*, vol. 93, no. 2, p. 021 803, Feb. 2016, Publisher: American Physical Society. DOI: 10.1103/PhysRevA.93.021803.
[137] R. G. E. Morris, A. F. van Loo, S. Kosen, and A. D. Karenowska, “Strong coupling of magnons in a YIG sphere to photons in a planar superconducting resonator in the quantum limit,” en, *Scientific Reports*, vol. 7, no. 1, p. 11 511, Sep. 2017, Publisher: Nature Publishing Group, ISSN: 2045-2322. DOI: 10.1038/s41598-017-11835-4.
[138] M. Song et al., “Single-shot electrical detection of short-wavelength magnon pulse transmission in a magnonic thin-film waveguide,” en, *npj Spintronics*, vol. 3, no. 1, p. 12, Apr. 2025, Publisher: Nature Publishing Group, ISSN: 2948-2119. DOI: 10.1038/s44306-025-00072-5.
[139] P. Krantz, M. Kjaergaard, F. Yan, T. P. Orlando, S. Gustavsson, and W. D. Oliver, “A quantum engineer’s guide to superconducting qubits,” en, *Applied Physics Reviews*, vol. 6, no. 2, p. 021 318, Jun. 2019, ISSN: 1931-9401. DOI: 10.1063/1.5089550.
[140] G. Lindblad, “On the generators of quantum dynamical semigroups,” en, *Communications in Mathematical Physics*, vol. 48, no. 2, pp. 119–130, Jun. 1976, ISSN: 0010-3616, 1432-0916. DOI: 10.1007/BF01608499.
[141] H.-P. Breuer and F. Petruccione, *The theory of open quantum systems*. Oxford ; New York: Oxford University Press, 2002, ISBN: 978-0-19-852063-4.
[142] S. Blanes, F. Casas, J. Oteo, and J. Ros, “The Magnus expansion and some of its applications,” en, *Physics Reports*, vol. 470, no. 5-6, pp. 151–238, Jan. 2009, ISSN: 03701573. DOI: 10.1016/j.physrep.2008.11.001.
[143] W. Magnus, “On the exponential solution of differential equations for a linear operator,” en, *Communications on Pure and Applied Mathematics*, vol. 7, no. 4,

pp. 649–673, Nov. 1954, ISSN: 0010-3640, 1097-0312. DOI: 10.1002/cpa.3160070404.
[144] C. K. Hong, "Measurement of subpicosecond time intervals between two photons by interference," *Physical Review Letters*, vol. 59, no. 18, pp. 2044–2046, 1987. DOI: 10.1103/PhysRevLett.59.2044.
[145] F. Bouchard et al., "Two-photon interference: The Hong–Ou–Mandel effect," en, *Reports on Progress in Physics*, vol. 84, no. 1, p. 012 402, Dec. 2020, Publisher: IOP Publishing, ISSN: 0034-4885. DOI: 10.1088/1361-6633/abcd7a.
[146] C. Drago and A. M. Brańczyk, "Hong–Ou–Mandel interference: A spectral–temporal analysis," *Canadian Journal of Physics*, vol. 102, no. 8, pp. 411–421, Aug. 2024, Publisher: NRC Research Press, ISSN: 0008-4204. DOI: 10.1139/cjp-2023-0312.
[147] K. T. Kapale, L. D. DiDomenico, H. Lee, P. Kok, and J. P. Dowling, "Quantum interferometric sensors," in *Quantum Sensing and Nanophotonic Devices*, vol. 5359, SPIE, Jul. 2004, pp. 169–176. DOI: 10.1117/12.516220.
[148] K. T. Kapale, L. D. Didomenico, H. Lee, P. Kok, and J. P. Dowling, "Quantum interferometric sensors," en, L. Cohen, Ed., Florence, Italy, Jun. 2007, p. 660 316. DOI: 10.1117/12.724317.
[149] J. P. Dowling, "Quantum optical metrology – the lowdown on high-N00N states," en, *Contemporary Physics*, vol. 49, no. 2, pp. 125–143, Mar. 2008, ISSN: 0010-7514, 1366-5812. DOI: 10.1080/00107510802091298.
[150] J. P. Dowling and K. P. Seshadreesan, "Quantum Optical Technologies for Metrology, Sensing, and Imaging," *Journal of Lightwave Technology*, vol. 33, no. 12, pp. 2359–2370, Jun. 2015, ISSN: 0733-8724, 1558-2213. DOI: 10.1109/JLT.2014.2386795.
[151] M. Kostylev, "Magnonic Hong-Ou-Mandel effect," *Physical Review B*, vol. 108, no. 13, p. 134 416, Oct. 2023, Publisher: American Physical Society. DOI: 10.1103/PhysRevB.108.134416.
[152] Z. Li, J. Sun, and F. Ma, "Floquet engineering of selective magnon–magnon coupling in synthetic antiferromagnets," *Applied Physics Letters*, vol. 123, no. 23, p. 232 406, Dec. 2023, ISSN: 0003-6951. DOI: 10.1063/5.0177917.
[153] S.-f. Qi and J. Jing, "Floquet generation of a magnonic NOON state," *Physical Review A*, vol. 107, no. 1, 2023. DOI: 10.1103/PhysRevA.107.013702.
[154] X. Zhu, R. Xia, and L. Xu, "Floquet-engineering magnonic NOON states with performance improved by soft quantum control," en, *Quantum Information Processing*, vol. 22, no. 12, pp. 1–15, Dec. 2023, Company: Springer Distributor: Springer Institution: Springer Label: Springer Number: 12 Publisher: Springer US, ISSN: 1573-1332. DOI: 10.1007/s11128-023-04200-0.
[155] P. G. Baity et al., "Strong magnon–photon coupling with chip-integrated YIG in the zero-temperature limit," *Applied Physics Letters*, vol. 119, no. 3, p. 033 502, Jul. 2021, ISSN: 0003-6951. DOI: 10.1063/5.0054837.

[156] L. Mach, “Ueber einen interferenzrefraktor,” German, *Zeitschrift für Instrumentenkunde*, vol. 12, pp. 89–93, Mar. 1892.
[157] L. Zehnder, “Ein neuer interferenzrefraktor,” German, *Zeitschrift für Instrumentenkunde*, vol. 11, pp. 275–285, Aug. 1891.
[158] C. M. Caves, “Quantum-mechanical noise in an interferometer,” *Physical Review D*, vol. 23, no. 8, pp. 1693–1708, Apr. 1981, Publisher: American Physical Society. DOI: 10.1103/PhysRevD.23.1693.
[159] A. Ekert, “Quantum interferometers as quantum computers,” en, *Physica Scripta*, vol. 1998, no. T76, p. 218, Jan. 1998, Publisher: IOP Publishing, ISSN: 1402-4896. DOI: 10.1238/Physica.Topical.076a00218.
[160] W. D. Oliver, Y. Yu, J. C. Lee, K. K. Berggren, L. S. Levitov, and T. P. Orlando, “Mach-Zehnder Interferometry in a Strongly Driven Superconducting Qubit,” *Science*, vol. 310, no. 5754, pp. 1653–1657, Dec. 2005, Publisher: American Association for the Advancement of Science. DOI: 10.1126/science.1119678.
[161] U. Grigull and H. Rottenkolber, “Two-Beam Interferometer Using a Laser,” EN, *JOSA*, vol. 57, no. 2, pp. 149–155, Feb. 1967, Publisher: Optica Publishing Group. DOI: 10.1364/JOSA.57.000149.
[162] D. Wilkie and S. A. Fisher, “Measurement of Temperature by Mach-Zehnder Interferometry,” en, *Proceedings of the Institution of Mechanical Engineers*, vol. 178, no. 1, pp. 461–470, Jun. 1963, Publisher: IMECHE, ISSN: 0020-3483. DOI: 10.1177/002034836317800166.
[163] J. G. Rarity et al., “Two-photon interference in a Mach-Zehnder interferometer,” *Physical Review Letters*, vol. 65, no. 11, pp. 1348–1351, Sep. 1990, Publisher: American Physical Society. DOI: 10.1103/PhysRevLett.65.1348.
[164] G. B. Xavier and J. P. v. d. Weid, “Stable single-photon interference in a 1 km fiber-optic Mach–Zehnder interferometer with continuous phase adjustment,” EN, *Optics Letters*, vol. 36, no. 10, pp. 1764–1766, May 2011, Publisher: Optica Publishing Group, ISSN: 1539-4794. DOI: 10.1364/OL.36.001764.
[165] Y. Ji, Y. Chung, D. Sprinzak, M. Heiblum, D. Mahalu, and H. Shtrikman, “An electronic Mach–Zehnder interferometer,” en, *Nature*, vol. 422, no. 6930, pp. 415–418, Mar. 2003, Number: 6930 Publisher: Nature Publishing Group, ISSN: 1476-4687. DOI: 10.1038/nature01503.
[166] O. A. Kaya, A. Cicek, A. Salman, and B. Ulug, “Acoustic Mach–Zehnder interferometer utilizing self-collimated beams in a two-dimensional phononic crystal,” *Sensors and Actuators B: Chemical*, vol. 203, pp. 197–203, Nov. 2014, ISSN: 0925-4005. DOI: 10.1016/j.snb.2014.06.097.
[167] M. Balynsky et al., “Magnonic interferometric switch for multi-valued logic circuits,” *Journal of Applied Physics*, vol. 121, no. 2, p. 024 504, Jan. 2017, ISSN: 0021-8979. DOI: 10.1063/1.4973115.
[168] Y. Fetisov and C. Patton, “Microwave bistability in a magnetostatic wave interferometer with external feedback,” *IEEE Transactions on Magnetics*, vol. 35,

no. 2, pp. 1024–1036, Mar. 1999, Conference Name: IEEE Transactions on Magnetics, ISSN: 1941-0069. DOI: 10.1109/20.748850.

[169] A. Khitun, M. Bao, and K. L. Wang, "Magnonic logic circuits," en, *Journal of Physics D: Applied Physics*, vol. 43, no. 26, p. 264 005, Jun. 2010, ISSN: 0022-3727. DOI: 10.1088/0022-3727/43/26/264005.

[170] N. Kostylev, M. Goryachev, A. D. Bulanov, V. A. Gavva, and M. E. Tobar, "Determination of Low Loss in Isotopically Pure Single Crystal 28Si at Low Temperatures and Single Microwave Photon Energy," en, *Scientific Reports*, vol. 7, no. 1, p. 44 813, Mar. 2017, ISSN: 2045-2322. DOI: 10.1038/srep44813.

[171] K.-S. Lee and S.-K. Kim, "Conceptual design of spin wave logic gates based on a Mach–Zehnder-type spin wave interferometer for universal logic functions," *Journal of Applied Physics*, vol. 104, no. 5, p. 053 909, Sep. 2008, ISSN: 0021-8979. DOI: 10.1063/1.2975235.

[172] O. Rousseau et al., "Realization of a micrometre-scale spin-wave interferometer," en, *Scientific Reports*, vol. 5, no. 1, p. 9873, May 2015, Number: 1 Publisher: Nature Publishing Group, ISSN: 2045-2322. DOI: 10.1038/srep09873.

[173] T. Schneider, A. A. Serga, B. Leven, B. Hillebrands, R. L. Stamps, and M. P. Kostylev, "Realization of spin-wave logic gates," *Applied Physics Letters*, vol. 92, no. 2, p. 022 505, Jan. 2008, ISSN: 0003-6951. DOI: 10.1063/1.2834714.

[174] A. B. Ustinov and B. A. Kalinikos, "Nonlinear microwave spin wave interferometer," en, *Technical Physics Letters*, vol. 27, no. 5, pp. 403–405, May 2001, ISSN: 1090-6533. DOI: 10.1134/1.1376765.

[175] M. P. Kostylev, A. A. Serga, T. Schneider, B. Leven, and B. Hillebrands, "Spin-wave logical gates," *Applied Physics Letters*, vol. 87, no. 15, p. 153 501, Oct. 2005, ISSN: 0003-6951. DOI: 10.1063/1.2089147.